Nanoscale Magnetic Resonance Spectroscopy Using Individual Spin Qubits

A dissertation presented
by

Igor Lovchinsky

to
The Department of Physics
in partial fulfillment of the requirements
for the degree of
Doctor of Philosophy
in the subject of

Physics

Harvard University
Cambridge, Massachusetts
May 2017

Dissertation Advisor: Author

Professor Mikhail D. Lukin **Igor Lovchinsky**

Nanoscale Magnetic Resonance Spectroscopy

Using Individual Spin Qubits

Abstract

Nuclear magnetic resonance (NMR) and electron paramagnetic resonance (EPR) are essential tools for both the physical and life sciences, but have been limited to the detection of large ensembles of spins due to their low sensitivity and the macroscopic nature of the sensors. Over the past several decades, significant efforts have been directed toward pushing this sensitivity to its ultimate physical limit, the detection of individual electronic and nuclear spin signals localized in a small volume. Our approach to nanoscale sensing achieves this goal by utilizing spin qubit sensors associated with individual nitrogen vacancy (NV) color centers in diamond.

In this thesis we develop new techniques and applications of nanoscale magnetic resonance spectroscopy. We begin with a brief review of several relevant properties of the NV center. In particular we discuss its level structure, the manipulation of its spin state via application of control fields and the various interactions with the local environment that lead to decoherence and relaxation of its spin state. We discuss the use of NV centers as nanoscale magnetic sensors and present a demonstration of the first magnetic resonance detection and spectroscopy of individual proteins using an approach based on quantum logic. We then demonstrate the use of NV-based nuclear quadrupole resonance (NQR) spectroscopy to probe the structure and spin dynamics

of a two-dimensional material. This is followed by the first experimental realization of all-optical detection of a single electronic spin. Finally, we end this thesis with the first demonstration of the detection of a single nuclear spin at room temperature using a technique based on utilizing a network of electronic spin-1/2 qubit sensors on the diamond surface.

Contents

Citations to Previously Published Work

Parts of Chapter 1 has been published in:

> "All-Optical Sensing of a Single-Molecule Electron Spin", A. O. Sushkov, N. Chisholm, I. Lovchinsky, M. Kubo, P. K. Lo, S. D. Bennett, D. Hunger, A. Akimov, R. L. Walsworth, H. Park & M. D. Lukin Nano Letters **14**, 6443 (2014).

Chapter 2, in its entirety, has been published as:

> "Nuclear Magnetic Resonance Detection and Spectroscopy of Single Proteins Using Quantum Logic", I. Lovchinsky, A. O. Sushkov, E. Urbach, N. P. de Leon, S. Choi, K. De Greve, R. Evans, R. Gertner, E. Bersin, C. Müller, L. McGuinness, F. Jelezko, R. L. Walsworth, H. Park & M. D. Lukin Science **351**, 836-841 (2016).

Chapter 3, in its entirety, has been published as

> "Magnetic Resonance Spectroscopy of an Atomically Thin Material Using a Single Spin Qubit", I. Lovchinsky, J. D. Sanchez-Yamagishi, E. K. Urbach, S. Choi, S. Fang, T. I. Andersen, K. Watanabe, T. Taniguchi, A. Bylinskii, E. Kaxiras, P. Kim, H. Park & M. D. Lukin Science **355**, 503-507 (2017).

Chapter 4 appears, in its entirety, as

> "All-Optical Sensing of a Single-Molecule Electron Spin", A. O. Sushkov, N. Chisholm, I. Lovchinsky, M. Kubo, P. K. Lo, S. D. Bennett, D. Hunger, A. Akimov, R. L. Walsworth, H. Park & M. D. Lukin Nano Letters **14**, 6443 (2014).

Chapter 5 appears, in its entirety, as

> "Magnetic Resonance Detection of Individual Proton Spins Using Quantum Reporters", A. O. Sushkov, I. Lovchinsky, N. Chisholm, R. L. Walsworth, H. Park & M. D. Lukin Physical Review Letters **113**, 197601 (2014).

Acknowledgments

First and foremost, I would like to acknowledge and thank my advisor Misha Lukin. Misha really taught me what it means to be a good scientist and I feel extremely fortunate to have had such a brilliant mentor. He always encouraged me to pursue my own ideas and always gave me the freedom to work on a variety of very different problems. I also want to thank the other members of my thesis committee, Hongkun Park and Markus Greiner. They supported and encouraged me throughout my PhD and provided invaluable insight. I have also had the great privilege of collaborating and working with other faculty members at Harvard as well as in other universities, including Ron Walsworth, Paola Cappellaro, Fedor Jelezko, Efthimios Kaxiras and Philip Kim.

I could not have gotten through grad school without the help of some wonderful and brilliant colleagues. First, Nick Chisholm has been my closest colleague and friend. When I entered grad school, he taught me everything from aligning a double-pass to how to properly handle tiny diamonds without flinging them across the room. I could not have asked for a better colleague, friend, moving buddy, diamond cleaner, wedding-singer and hair-stylist.

I have been lucky to work with many other brilliant graduate students, postdocs and undergraduate students, including Elana Urbach, Alex Sushkov, Arthur Safira, Eric Bersin, Javier Sanchez-Yamagishi and many, many others. My time here would not have been the same without their advise and ideas. I also want to thank Jacob Barandes who, in addition to being a great mentor and friend, really inspired me to go into physics in the first place and was always an invaluable source of wisdom.

Finally, I want to thank my family. My wife Alice and my parents, Tamara and

Leonid, and my brother Dmitriy were all extremely supportive when, at the ripe age of 26, I decided to become a scientist and go to grad school. My daughter, Alina, while perhaps not appreciating the finer details of dynamical decoupling pulse sequences, nevertheless indulged me as I read Quantum Physics for Babies to put her to sleep.

To my parents, Tamara and Leonid

Chapter 1

Introduction

1.1 Background

Precision magnetic sensing is essential to a wide array of technologies, with important applications in both the physical and life sciences. In particular, in biology and medicine, nuclear magnetic resonance (NMR) has been a leading technology for investigating the structure and motional properties of proteins [1, 2, 3, 4, 5] and other biomolecules [6], while functional magnetic resonance imaging (fMRI) has emerged as a primary workhorse for obtaining key physiological and pathological information (such as blood and tissue oxygen level and redox status [7, 8, 9]) noninvasively. Developing nanoscale magnetic sensing applicable to individual molecules could enable revolutionary advances in the physical, biological, and medical sciences. Examples include determining the structure of single proteins and other biomolecules as well as in vivo measurements of small concentrations of reactive oxygen species that could lead to insights into cellular signaling, aging, mutations, and cancer [10, 11, 12]. The

practical realization of these ideas is extremely challenging, however, as it requires sensitive detection of weak magnetic fields associated with individual electronic or nuclear spins at nanometer scale resolution, often under ambient, room-temperature conditions.

Many state-of-the-art magnetic sensors, including superconducting quantum interference devices (SQUIDs) [13], semiconductor Hall effect sensors [14], and spin exchange relaxation-free atomic magnetometers [15], offer outstanding sensitivity, but their macroscopic nature precludes individual spin sensing. Sensing ensembles of paramagnetic molecules in biological and medical systems is currently performed using bulk electron paramagnetic resonance (EPR), which has a limit of approximately 10^7 electron-spins [16]. Bulk NMR is typically limited to macroscopic sample quantities and often requires high magnetic fields [17]. Microcoil NMR detectors have recently been used to detect micron-sized nuclear spin samples, although further improvements in spatial resolution of this technique are challenging [18, 19]. Magnetic resonance force microscopy (MRFM) has been used to detect a $(4\text{ nm})^3$ voxel of hydrogen nuclear spins as well as individual electronic spins, but at cryogenic, milliKelvin temperature under high vacuum [20, 21].

The nitrogen-vacancy (NV) color center in diamond has recently emerged as a promising precision magnetic field sensor with nanoscale resolution [22, 23]. Ensembles of NV centers in bulk diamond have been used to sense paramagnetic molecules in solution [24], with sensitivity of 10^3 statistically polarized electronic spins and spatial resolution of approximately 450 nm, and NV centers in nanodiamonds have been used to sense paramagnetic ions covering the nanodiamond surface [25] and in a lipid

bilayer formed around the nanodiamond surface [26]. Shallow NV centers have also been used to detect nanoscale ensembles of nuclear spins, covering the surface of a bulk diamond crystal [27, 28].

1.2 Overview of Thesis

In this dissertation we develop new techniques and applications for nanoscale magnetic sensing using individual NV centers, although many of the techniques presented can readily be applied to NV ensembles as well as to other types of atomic-sized sensors. In the remainder of Chapter 1, we provide a brief introduction to the structure of the NV center and discuss its many remarkable properties. The remaining chapters present experimental demonstrations of various nanoscale sensing applications. In Chapter 2 we demonstrate the magnetic resonance detection and spectroscopy of individual protein molecules using a readout scheme based on quantum logic. In Chapter 3 we use nuclear quadrupole resonance (NQR) spectroscopy to study the structure and nuclear spin dynamics in a two-dimensional (2D) material. In Chapter 4 we use a technique based on relaxometry to demonstrate the room-temperature detection of individual electronic spins and in Chapter 5 we use a network of electronic spin defects on the diamond surface to demonstrate sensing of an individual nuclear spin. A brief summary as well as an outlook on future applications in provided in Chapter 6.

1.3 The Nitrogen Vacancy Color Center

1.3.1 Introduction

The NV center is a point defect in the diamond lattice that consists of a substitutional nitrogen atom and an adjacent carbon vacancy [29, 30]. The structure of this defect defines a symmetry axis (henceforth referred to as the NV axis) that can be oriented along the four crystallographic directions in the diamond lattice (Fig. 1.1A). This color center is often found in natural diamond but can also be incorporated via implantation of nitrogen ions, followed by a vacuum anneal at high temperature or by introducing nitrogen impurities during the chemical vapor deposition (CVD) growth process. For all the work presented in this thesis, we use electronic-grade, CVD-grown diamond with NV centers implanted several nanometers below the surface (see, for example, Section A.3 for details).

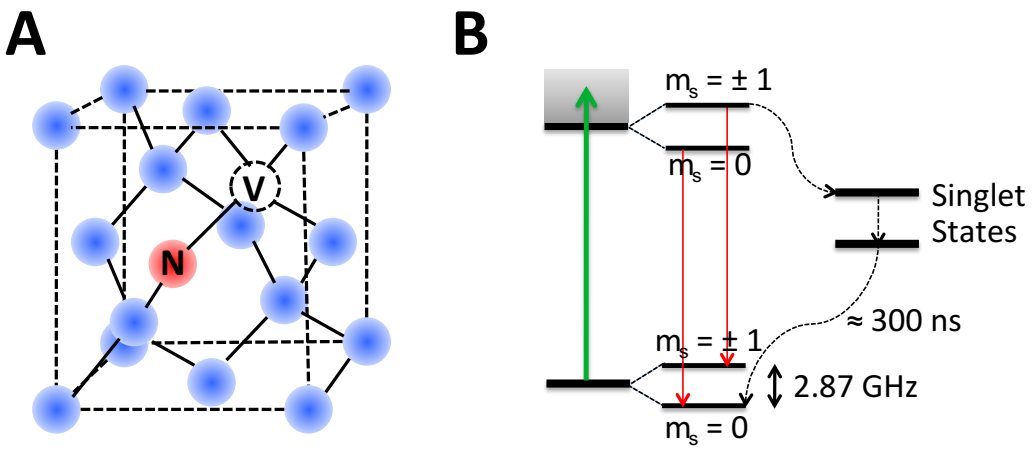

Figure 1.1: The nitrogen vacancy (NV) color center in diamond. **(A)** The NV defect in the diamond lattice. **(B)** Simplified level structure of the NV center.

The NV center can exist in several charge states [29]. In this work, we exclusively

consider the negatively charged defect, which we henceforth refer to simply as the NV center. The NV center incorporates six electrons; three are associated with dangling bonds from the proximal carbon atoms, two come from the nitrogen atom and one is captured from a nearby donor [29]. The ground state of the NV center is a spin triplet, characterized by the $m_s = 0$ and the $m_s = \pm 1$ magnetic sublevels. For simplicity, we refer to these states as $|0\rangle$ and $|\pm 1\rangle$. In the absence of an external applied magnetic field, the states $|\pm 1\rangle$ are degenerate, while $|0\rangle$ is separated by the zero-field splitting of approximately 2.87 GHz [29]. Applying an external magnetic field lifts the degeneracy of the $|\pm 1\rangle$ states and shifts the levels via the Zeeman effect. Applying a microwave field resonant with the $|0\rangle \rightarrow |\pm 1\rangle$ transition induces coherent population transfer between the magnetic sublevels.

As shown in Fig. 1.1B, the ground and excited states of the NV center are separated by approximately 637 nm (add this to figure). When the NV is optically pumped using above-band excitation, phonon relaxation brings the NV into one of the excited states. At room temperature, the NV primarily fluoresces into the broad phonon sideband (640-800 nm), with only $\sim$4 % of the emission going into the zero-phonon line [30]. The dipole transition between the ground and excited states is primarily spin conserving. However, experiments and calculations have shown [30, 31] that the $|\pm 1\rangle$ states in the excited electronic configuration can also decay, with lower probability, through a set of metastable singlet states into the $|0\rangle$ magnetic sublevel of the ground state electronic configuration. This mechanism allows the NV center to be optically pumped into the $|0\rangle$ state. Additionally, the reduction of fluorescence intensity due to the non-radiative decay of the NV through the metastable singlet

states allows us to distinguish the populations of the $|0\rangle$ and $|\pm1\rangle$ states. In practice, this reduction in fluorescence intensity is approximately 30-40%.

1.3.2 Decoherence of NV Centers

Most NV-based sensing applications require that the NV spin be well-isolated from unwanted sources of noise in its environment. In practice, the NV spin coherence is typically limited by interactions with impurities in the diamond lattice. The most common of these are ^{13}C nuclear spins (I = 1/2), which comprise 1.1% of the carbon in natural-abundance diamond. Indeed, it has been observed that enriching the diamond with the spinless isotope ^{12}C dramatically reduces the effects of dephasing and decoherence (the timescales associated with these processes are commonly referred to as $1/T_2^*$ and $1/T_2$, respectively) for NV centers deep within the bulk of the diamond crystal [32]. For NV centers formed within a few nanometers of the diamond surface, additional sources of noise (likely caused by electronic spin defects associated with the surface) further limit the NV spin coherence [33].

Typically, the spin dephasing time T_2^* is measured via a Ramsey experiment [30]. The T_2^* time is typically limited by inhomogeneities in the local magnetic field, which can be partially cancelled by applying a rephasing π-pulse in the middle of the free evolution interval [30]. This type of measurement, referred to as a spin-echo experiment, typically extends the spin coherence time, which in this context is typically referred to as the T_2 time. Applying additional π-pulses during the free evolution interval, often referred to as pulsed dynamical decoupling, can further extend the T_2 time [34]. The extension of the spin coherence time with the application of multiple

π-pulses can be understood in terms of cancelling out progressively higher frequencies of the environmental magnetic noise spectrum [35].

1.3.3 Population Relaxation of NV Centers

The NV spin also interacts with lattice phonons, which typically lead to spin-lattice relaxation on a timescale characterized by T_1. This mechanism is highly temperature dependent and typically results in population relaxation times of $\sim$10 ms at room temperature [36]. It has been shown that shallow NV centers, and particularly NV centers in nanodiamonds can have additional sources of population relaxation, likely associated with surface defects [26, 25]. Typically, the population relaxation time T_1 is measured simply by optically initializing the NV spin state, waiting a variable duration of time and finally measuring the state.

1.3.4 NV-Based Magnetometry

It has been demonstrated [23, 22] that NV centers in both bulk and nanocrystal diamond can be used as nanoscale magnetic field sensors. Various types of NV-based sensing protocols have by now been demonstrated, each of which is optimized for different applications. For example, sensing of DC fields is typically accomplished by monitoring the frequency of the ESR transition [37] or via Ramsey interferometry [22], where (in the rotating frame) the superposition of the $|0\rangle$ and $|1\rangle$ states accumulates a phase proportional to the local magnetic field. A spin echo experiment is no longer sensitive to the DC component of the magnetic field, but instead can be used for AC magnetometry, as described in [23]. Applying additional π-pulses (for example,

as in CPMG or XY8) [38, 27] further narrows the range of frequencies the NV is sensitive to, while at the same time increasing the spin coherence time. The continuum limit of pulsed dynamical decoupling, often referred to as spin-locking, has also been demonstrated for NV-based magnetic sensing [39].

When the spectral density of the target field is very broad (for example in the case of Gd spins fluctuating at $\sim$10 GHz frequencies, see Chapter 4), dynamical decoupling techniques are no longer applicable. In such cases it is nevertheless still possible to detect the field by monitoring the population relaxation of the NV spin state, which is sensitive to the Fourier component of the fluctuating field at the sensor frequency (2.87 GHz when no external magnetic field is applied). Variation of the applied field allows probing of different frequency components of the noise spectrum.

In this thesis we discuss using shallow NV centers to sense magnetic fields created by electronic and nuclear spins positioned on the diamond surface. In all cases that we consider, the target spins that we sense are unpolarized (the magnetic field created by the nuclear spins, averaged over many iterations of the experiment, is zero). The variance of the magnetic field, however, is non-zero and consequently, our protocols are optimized to detect this variance. Sensing variance allows us to work at low magnetic fields (where thermal polarization is negligible) but has the disadvantage of being only quadratically sensitive to small fields (see Section A.6). We discuss improvements to our technique which would allow us to be linearly, rather than quadratically, sensitive in Chapters 2 and 3.

Chapter 2

Nuclear Magnetic Resonance Detection and Spectroscopy of Single Proteins Using Quantum Logic

2.1 Introduction

Nuclear magnetic resonance (NMR) spectroscopy is a powerful tool for the structural analysis of organic compounds and biomolecules. Conventional NMR spectroscopy, however, relies on detecting the weak magnetization of a thermally polarized ensemble of nuclear spins and therefore typically requires high magnetic fields and macroscopic sample quantities [17]. We utilize a sensor, consisting of two quantum bits corresponding to an electronic spin of an NV center and an ancillary nuclear spin,

to demonstrate room temperature magnetic resonance detection and spectroscopy of multiple nuclear species within individual ubiquitin proteins attached to the diamond surface. Using quantum logic to improve readout fidelity and a surface treatment technique to extend the spin coherence time of shallow NV centers, we demonstrate magnetic field sensitivity sufficient to detect individual proton spins within one second of integration. This gain in sensitivity enables high-confidence detection of individual proteins and allows us to observe spectral features that reveal information about their chemical composition.

2.2 Measurement Scheme

In our approach (Fig. 2.1), we measure individual Fourier components of the time-varying magnetic field created by a statistically polarized subset of proximal nuclear spins contained within a protein. The transverse magnetization of the spin ensemble undergoes precession at the nuclear Larmor frequency with a phase and amplitude that vary stochastically with every repetition of the sequence. Averaging over many iterations yields a zero mean magnetization but a nonzero variance, resulting in a measurable magnetic resonance signal. In order to use the NV center as a sensor, its spin state is manipulated with a series of periodic microwave (MW) pulses separated by free evolution intervals of length τ (Fig. 2.1B). This periodic modulation of the NV center spin creates a narrow band-pass frequency filter, allowing phase accumulation when the modulation frequency, defined as $1/\tau$, is close to twice the nuclear Larmor frequency [22, 38]. Varying the spacing between the π-pulses yields a frequency spectrum which encodes information about the nuclear spins within the protein.

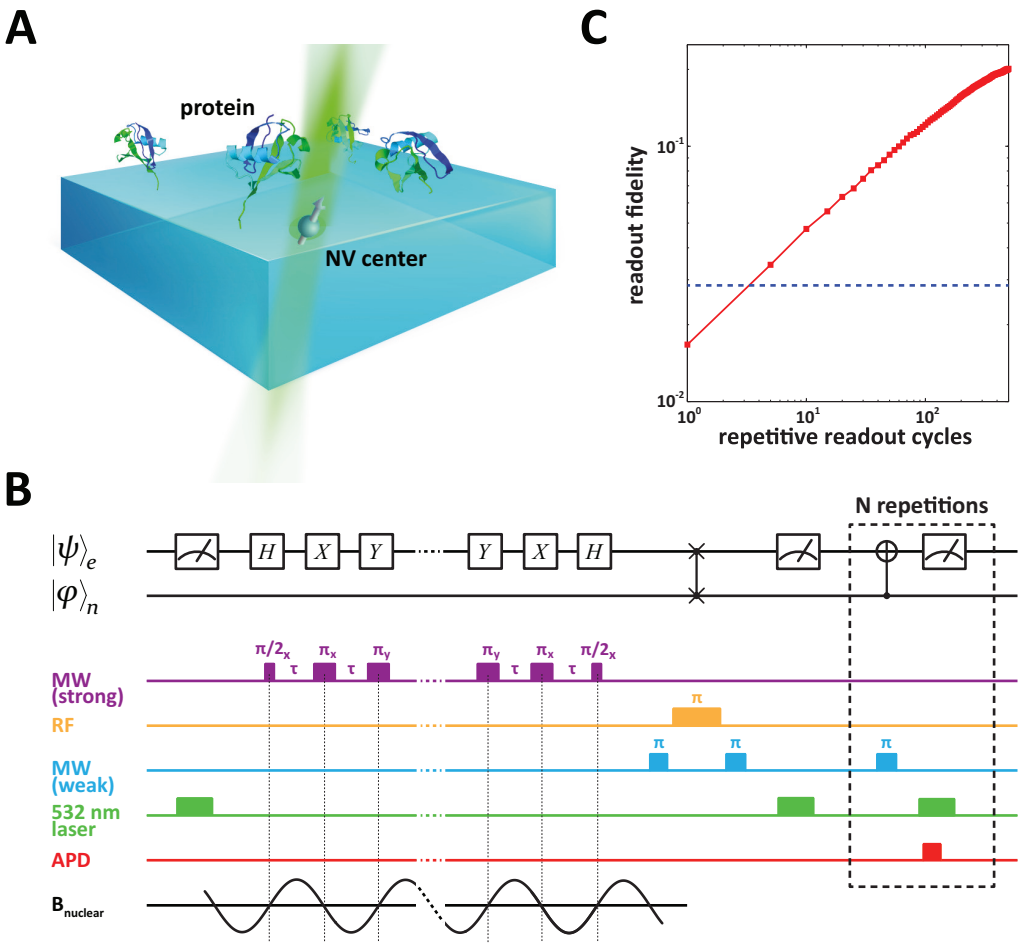

Figure 2.1: **Experimental setup and magnetometry with repetitive readout.** **(A)** Schematic of experimental setup. Ubiquitin proteins attached to the diamond surface are probed using a proximal quantum sensor consisting of a NV center electronic spin and its associated ^{15}N nuclear spin. Image of ubiquitin was taken from Research Collaboratory for Structural Bioinformatics Protein Data Bank (PDB ID: 1UBQ) [40] **(B)** Quantum circuit diagram and experimental magnetometry pulse sequence. Here the NMR signal is measured using a modified XY8-k dynamical decoupling sequence (Appendix A) and detected using repetitive readout of the electronic spin state. **(C)** Measured gain in the readout fidelity $\mathcal{F}$ as a function of repetitive readout cycles. The dashed blue line indicates the measured fidelity using conventional readout. The readout fidelity is measured by detecting the average number of photons scattered from the NV center after preparing it in the $m_s = 0$ or $m_s = 1$ sublevel and applying Eq. 9 (Appendix A).

2.3 Sensitivity

Assuming that the spins are situated on the diamond surface at distance d directly above the NV center, the optimal sensitivity of this technique, defined by the minimum number N of nuclear spins detectable after one second of integration, is achieved when the pulse sequence duration is approximately equal to the coherence time T_2 of the NV electronic spin [22], and is given by (see Appendix A)

$$N \approx \frac{16\pi^4 d^6}{(\mu_0 \hbar \gamma_e \gamma_n)^2 \mathcal{F}} \frac{\sqrt{T_2 + T_R}}{T_2^2}. \tag{2.1}$$

Here, $\gamma_e = 1.76{\times}10^{11}$ s^{-1} T^{-1} and γ_n are the electron and nuclear gyromagnetic ratios (for proton spins $\gamma_n = 2.68{\times}10^8$ s^{-1} T^{-1}), d is the NV center depth, μ_0 is the vacuum permeability and T_R is the readout time. The readout fidelity $\mathcal{F} = \left[1 + 2(\alpha_0 + \alpha_1)/(\alpha_0 - \alpha_1)^2\right]^{-\frac{1}{2}}$ is determined by the mean number of photons α_0, α_1 detected, per shot, from the $m_s = 0$ and $m_s = 1$ spin sublevels of the NV center, respectively. The readout fidelity encapsulates the effect of photon shot noise and approaches unity for an ideal, projection noise-limited measurement.

2.3.1 Quanum Logic-Based Readout of the Spin State

One limitation to the sensitivity is due to the imperfect readout of the NV center. For typical fluorescence collection efficiencies, $\mathcal{F} \approx 0.03$ (Section A.6). Thus $\sim 10^3$ repetitions of the experiment are required to distinguish the fluorescence of the $m_s = 0$ and $m_s = \pm 1$ sublevels. To circumvent this imperfection, we utilize a two-qubit quantum system consisting of an NV center electronic spin and its associated ^{15}N nuclear spin, such that after the sensing sequence, the resulting NV spin

can be repeatedly probed without resetting its state via optical pumping [41, 42]. We use quantum logic (Fig. 2.1B) to manipulate the two coupled qubits and to improve readout fidelity (see Appendix A for details). The experimentally measured gain in the readout fidelity as a function of readout cycles (Fig. 2.1C, red points) demonstrates an almost 10-fold improvement for several hundred repetitions as compared to conventional readout (dashed blue line). We note that although repetitive readout of the electronic spin state leads to an increase in the readout time T_R (Appendix A), the sensitivity is only weakly dependent on this variable. Therefore, in the regime where T_R is on the order of T_2, we achieve a significant gain in sensitivity.

2.3.2 Reduction of Decoherence Rate via Oxygen Termination

Another key limitation to the sensitivity is due to the decoherence of near-surface NV centers [33] (i.e. with small d). To quantify the effect of the surface on the NV spin coherence, the decoherence rates ($1/T_2$) and depths (Appendix A) were measured for a large number of NV centers created by implantation of 2 keV ^{15}N ions. As shown in Table S1, the depths and decoherence rates of shallow NV centers are inversely correlated. To improve the coherence properties, we use wet oxidative chemistry combined with a 465 °C anneal [43, 44] in a dry oxygen environment (Appendix A). This procedure etches away the diamond surface, while improving the coherence times by more than an order of magnitude. This increase in T_2, when combined with the 10-fold improvement in readout fidelity resulting from quantum logic-based readout, yields shallow (3 - 6 nm) NV centers with an overall sensitivity gain of more than

a factor of 500 (Fig. 2.2A), exceeding sensitivities reported in previous experiments (Appendix A). The resulting sensitivity is sufficient to detect a single proton spin or approximately 10 statistically polarized ^{13}C or ^{2}H spins after one second of integration (see Fig. 2.2A and (Appendix A).

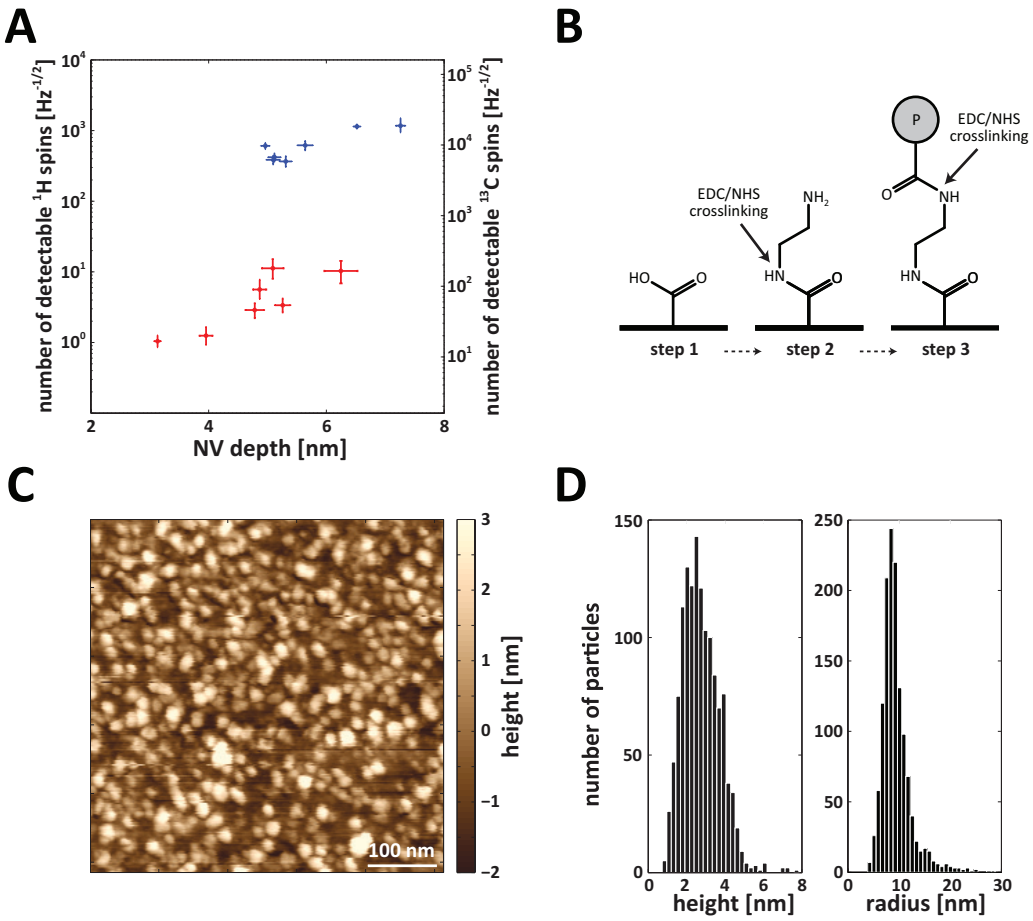

Figure 2.2: **Surface preparation of diamond samples and single protein attachment. (A)** Measured depths and sensitivities (^{1}H and ^{13}C spins) for a representative sample of NV centers before (blue) and after (red) oxygen surface treatment and quantum logic-based readout. See Table S1 for numerical values of measured depths and decoherence rates. **(B)** Attachment protocol using carbodiimide crosslinker chemistry (see Appendix A). **(C)** AFM height image of diamond surface after protein attachment. Color bar indicates height values. **(D)** Histograms of heights and radii of circular features in a 1x1 μm AFM image (see Appendix A).

2.4 Protein Sample Preparation

We use our enhanced sensitivity to probe ubiquitin, a small regulatory protein consisting of 76 residues that is found in almost all eukaryotic cells [45]. The size of this protein [40] is on the order of the NV detection area/volume (Appendix A), determined by the NV center depth for $d \sim 3 - 5$ nm. Thus, any observed NMR signals can be attributed to individual or small aggregates of proteins. We immobilize the proteins on the diamond surface using carbodiimide crosslinker chemistry [46, 47] (see Fig. 2.2B and Appendix A). An atomic force microscope (AFM) is used to characterize the topography of the diamond surface after protein attachment (Appendix A). The AFM images (Fig. 2.2C) exhibit circular features with heights and radii (Fig. 2.2D) that are consistent with the known size of the protein. We observe almost no features with height larger than 5 nm, suggesting that our attachment protocol does not lead to aggregation. The resolution in the lateral dimensions is consistent with the limit imposed by the radius of the AFM probe (9 ± 2 nm). We confirm that individual spots in Fig. 2.2C mostly correspond to individual proteins by conjugating the proteins to Cy3 fluorophores and comparing the resulting mean fluorescence rate with that of optically-resolved Cy3+ubiquitin complexes and individual Cy3 dye molecules (Appendix A). We find that the mean protein spacing as extracted from optical measurements (20.9 ± 1.4 nm) is in excellent agreement with that based on AFM measurements (21.6 ± 0.4 nm). Importantly, these measurements show that the mean spacing of the proteins is much greater than the typical NV center depth ($d \approx 4$ nm) and the protein size. Due to the strong $\sim 1/r^6$ dependence of the NMR contrast on the NV-protein separation r (Appendix A), the NMR signal

is negligible for proteins located far outside the NV detection area. Therefore, with our protein density, we expect approximately 10% of NV centers to contain a single protein within their detection areas. The statistical probability of detecting two or more proteins using a single NV center is about 1% (Appendix A).

In order to spectrally differentiate the magnetic fields produced by protein nuclear spins from background sources, such as ^{1}H spins on the diamond surface [48] and ^{13}C spins in the diamond lattice, we use diamond samples enriched in ^{12}C (99.999% abundance) and proteins enriched in the rare isotopes ^{2}H and ^{13}C (both at $> 98\%$ abundance).

2.5 NMR of Individual Ubiquitin Proteins

We first carried out NMR measurements on 20 shallow NV centers, with isotopically enriched ubiquitin proteins attached to the diamond surface. Three of the NV probes exhibited NMR signals at both the ^{2}H and ^{13}C Larmor frequencies (Appendix A). No instances occurred in which only one of these nuclear species was detected. Representative spectra (Figs. 2.3A,B) were obtained by varying the spacing of the periodic π-pulses. Here the data were normalized to subtract the effect of NV decoherence (Appendix A). The ^{2}H and ^{13}C spectra were acquired using XY8-507 and XY8-1011 pulse sequences (Appendix A), respectively, and measured via 500 repetitive readout cycles. The identities of the nuclear species were verified by observing the linear scalings of the nuclear Larmor frequencies with the applied magnetic field (Fig. 2.3C - blue and red points).

The spectral resolution $\Delta\nu$ of the present method is Fourier-limited by the total

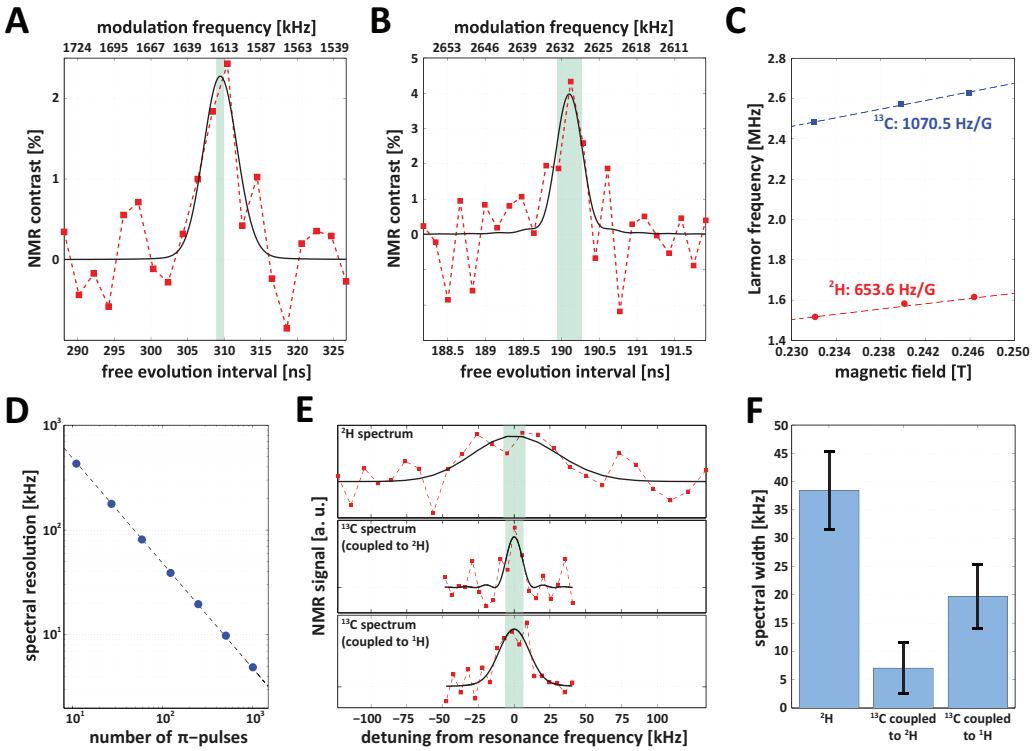

Figure 2.3: **NMR detection and spectroscopy of individual Ubiquitin proteins. (A)** ^{2}H NMR spectrum at B = 2473 G using XY8-507 sequence with 500 repetitive readout cycles (red points) and fit (black solid line). The spectrum consists of the NV optical signal, normalized by the Rabi contrast and corrected for the reduced contrast caused by decoherence (Appendix A). **(B)** Analogous ^{13}C NMR spectrum at B = 2457 G using XY8-1011 sequence with 500 repetitive readout cycles (red points) and fit (black solid line). **(C)** Scalings of resonance frequencies with applied magnetic field. Red and blue indicate the deuterium and ^{13}C resonances, respectively (see Appendix A). The expected scalings based on the known gyromagnetic ratios are indicated with dashed lines. Error bars are approximately on the scale of the marker sizes. **(D)** Measured spectral resolution (blue points) as a function of number of π-pulses. Dashed black line indicates theoretical limit imposed by the detector filter function (Appendix A). A 2.63 MHz RF waveform, corresponding to τ = 190 ns, applied using an external coil, was used as the calibration signal and the resulting NMR signal was measured using an XY8 sequence. **(E)** ^{2}H and ^{13}C NMR linewidths (red points) measured on deuterated (top and middle panel) and non-deuterated (bottom panel) ubiquitin proteins. B = 2422 G (top), 2402 G (middle), 2455 G (bottom). In (a), (b), and (e), fitted curves are gaussian functions, convolved with the detector filter function. Green shaded regions correspond to the spectral resolution (Appendix A). **(F)** The average spectral widths from several independent measurements of ^{2}H and ^{13}C NMR spectra (Appendix A). Here the observed spectra have been deconvolved from the detector filter function to yield the true linewidths (as extracted from fits presented in Appendix A). The error bars correspond to the standard errors of the mean of the spectral widths, for each of the three categories of spectra. For all ^{13}C spectra of non-deuterated proteins, we verified that the ^{13}C signal disappears when the proteins are removed from the diamond (Appendix A).

duration of the coherent evolution of the quantum spin sensor (Fig. 2.3D). Note that the 10-fold increase in the coherence time T_2 demonstrated in Fig. 2.2A directly yields a corresponding 10-fold improvement in spectral resolution (Appendix A), allowing us to resolve features in the protein spectra and revealing information about its chemical composition.

Figure 2.3E shows the ^{2}H and ^{13}C NMR spectra (top two panels), corresponding to ubiquitin proteins enriched with ^{2}H and ^{13}C, performed on another NV center. Consistent with the results of Figs. 2.3A,B for the first NV center, we find that the deuterium spectrum exhibits an extremely broad lineshape while the ^{13}C spectral width is considerably narrower and is consistent with the Fourier limit. The bottom panel in Fig. 2.3E shows the ^{13}C NMR spectrum after attaching ubiquitin proteins enriched only in ^{13}C. We observe a ^{13}C lineshape that is significantly broader ($\sim$ 20 kHz) than that of the deuterated proteins. The spectral resolution, determined by the external magnetic field and the number of applied π-pulses, is indicated by the shaded green regions. Figure 2.3F shows the average deconvolved spectral widths of ^{2}H and ^{13}C, as observed in independent measurements of three NV centers with deuterated proteins and three NV centers with non-deuterated proteins.

Previous studies [49] have shown that solid-state ^{2}H NMR spectra typically exhibit line broadening due to the inhomogeneous distribution of quadrupole shifts within the protein [50] (see also Fig. 2.4A). The broadening of our ^{2}H spectra is consistent with this effect. Our ^{2}H NMR signals are likely dominated by the deuterons in methyl groups, which rotate rapidly at room temperature about the methyl group symmetry axis. The remaining (non-averaged) quadrupolar shifts are on the order of 30 kHz [49]

(the deuterons in other chemical groups, such as methylene or aromatic, give rise to much broader spectral features and hence smaller signals). The ^{13}C linewidths are consistent with the expected broadening created by dipolar interactions with proximal ^{2}H (in deuterated proteins) and ^{1}H (in non-deuterated proteins) spins [49], with ^{1}H giving rise to broader linewidths due to its larger gyromagnetic ratio.

Our method can be extended in a number of ways. The sensitivity can be further improved by utilizing spin-to-charge readout [51] or the use of more advanced pulse sequences that could extend the coherence time to the limit imposed by the population relaxation time T_1 (see for example Appendix A, where we demonstrate coherent spin locking for up to 1 ms). Nuclear hyperpolarization (Appendix A), such as Hartmann-Hahn double resonance [39], can also be used to improve sensitivity by directly detecting nuclear magnetic moments, rather than their variances. Alternatively, reporter spin-based sensing can be used to reach single spin sensitivity by resolving individual nuclear spins in a field gradient created by an electronic reporter spin [52]. Similarly, if background protons can be removed from the diamond surface (protons in liquid water diffuse quickly and do not contribute to the NMR signal [53]) by deuterating the surface [27], ^{1}H spins, with their large gyromagnetic ratio, can be used for indirect detection of nuclei with low magnetic moments [54]. In addition, the coupling to a long-lived quantum memory associated with an ancillary nuclear spin qubit and the use of new pulse sequences [52, 55] should allow further improvement in spectral resolution to the limit determined by the lifetime of the nuclear spin ancilla, which could be less than 10 mHz [56]. Independently from the NV and nuclear spin manipulation, the detection sensitivity and utility of the method can be significantly

enhanced by deterministically positioning the molecules in close proximity to an NV center; e. g. by activating local chemical sites using super-resolution microscopy [57] or by placing them with a magnetized AFM tip [20, 21]. While at present the inability to position the protein over a desired NV center resulted in long required integration times (Appendix A), deterministic placement, combined with a factor of ∼3 improvement in coherence time would enable detection of an individual deuteron after several seconds of integration (see Appendix A).

2.6 Quadrupolar Spectroscopy for Single Molecule Structure Determination

The demonstrated technique, along with these potential improvements, may enable applications for probing the structure and dynamics of biological systems at the single-molecule level. For example, the single molecule NMR method using quadrupolar nuclei with $I > 1/2$, can be used to study conformations and electrostatic environments within individual molecules. One can use the dependence of the nuclear spin level structure on the orientation of its quadrupolar axes with respect to the applied magnetic field to determine the spin's electrostatic environment (quadrupole coupling constant $\bar{Q}$ and asymmetry parameter) as well as the orientation of its molecular axes (Fig. 2.4A) [49]. While in our experiments (Fig. 2.3E) these quadrupolar shifts result in broadening of the observed spectral line, if the number of nuclear spins in the molecule N_m is such that $\bar{Q}/(N_m \Delta\nu) > 1$, a condition which ensures that the spectral range $\sim \bar{Q}$ is not over-crowded with resonances, the spectral lines associated

with individual nuclei can be resolved and analyzed. As an example, Fig. 2.4B shows the simulated ^{2}H and ^{14}N quadrupolar spectra of a single phenylalanine molecule for two orthogonal orientations (top and second panels) and for two distinct conformations (second and third panels). These orientation-dependent shifts wash out in bulk NMR measurements (lower panel). Unlike in bulk NMR with crystallized samples, the weights of the various single molecule NMR resonances in a finite magnetic field (Fig. 2.4C) encode information about the positions of the spins within the molecule, thus allowing structural information to be deduced (Appendix A) irrespective of the location of the target molecule.

2.7 Outlook

Our approach provides a set of tools, complementary to conventional NMR, that can be used to probe the structure and dynamics of biological and chemical systems at the single-molecule level and reveal properties normally obscured in ensemble measurements. With additional improvements in sensitivity these (Appendix A) can potentially be useful for NMR-based label-free single molecule detection and analysis, for characterizing the structure and conformational changes in systems not easily accessible by conventional techniques and for studies of dynamic phenomena such as protein folding [58] and enzyme-substrate interactions at the single-molecule level [59].

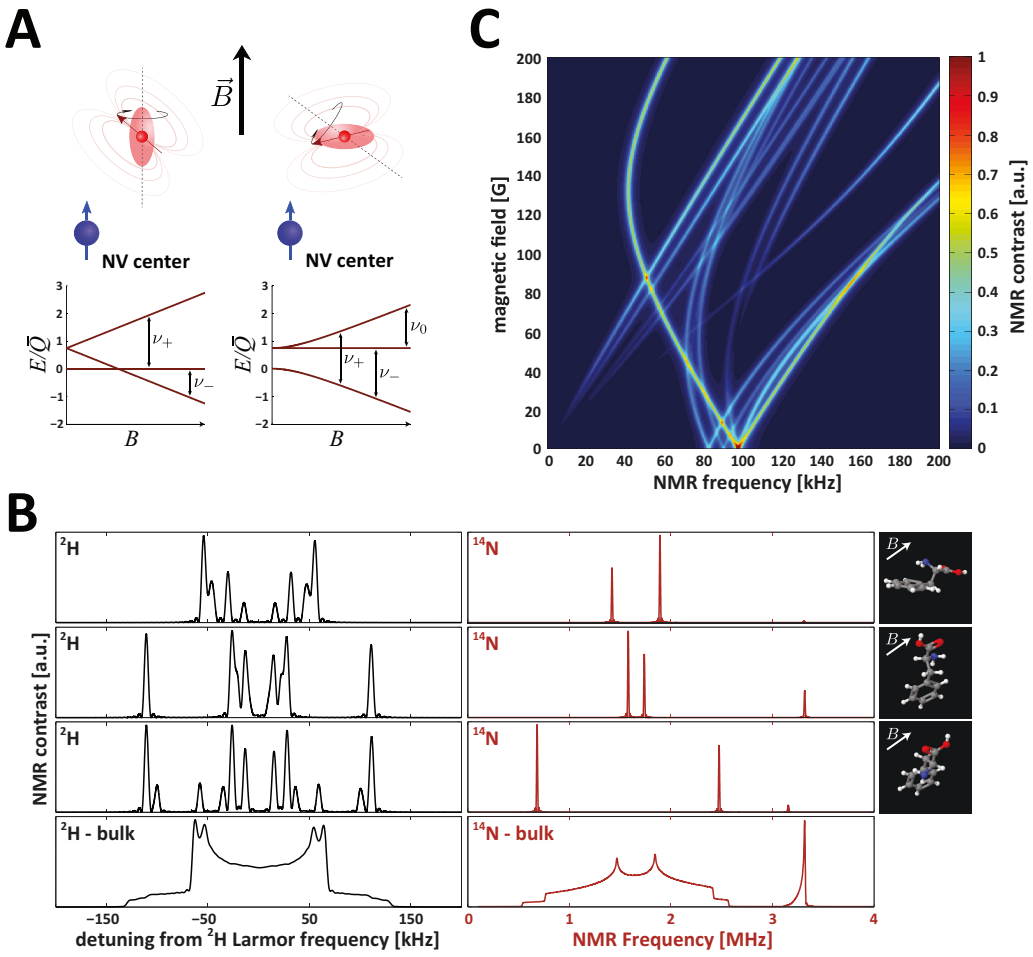

Figure 2.4: **Proposed Analysis of Individual Molecules (A)** Orientation-dependent level structure of quadrupolar nuclear spins in an external magnetic field. The two spin-1 nuclei shown are interacting with a proximal NV center through magnetic dipole-dipole interactions. The major axes of the ellipses denote the orientation of the molecular axis. The quantization axis in each case is indicated by the dashed line. The effect of a non-zero asymmetry parameter is neglected. Allowed transitions ($\nu_\pm$ and ν_0) are indicated by arrows (Appendix A). **(B)** Simulated quadrupolar ^{2}H and ^{14}N spectra of deuterated Phenylalanine in two orthogonal orientations relative to the diamond surface (top and second panels), two distinct conformations (second and third panels) and the simulated bulk spectra (bottom panels), where all possible orientations contribute equally to the spectrum. Images of Phenylalanine are taken from the Research Collaboratory for Structural Bioinformatics Protein Data Bank (PDB ID: PHE) and visualized using Jmol: http://www.jmol.org/. For the case of ^{2}H, only the spectral lines corresponding to $\nu_\pm$ (Appendix A) are shown. We assume that a magnetic field of 0.5 T is applied along the NV symmetry axis. **(C)** Magnetic field dependence of ^{2}H spectrum corresponding to panel 3 in (b) at low magnetic field. Color bar represents NMR contrast.

Chapter 3

Magnetic Resonance Spectroscopy of an Atomically Thin Material Using a Single Spin Qubit

3.1 Introduction

Two-dimensional (2D) materials offer a promising platform for exploring condensed matter phenomena and developing technological applications. However, the reduction of material dimensions to the atomic scale poses a challenge for traditional measurement and interfacing techniques that typically couple to macroscopic observables. We demonstrate a method for probing the properties of 2D materials via nanometer-scale nuclear quadrupole resonance (NQR) spectroscopy using individual atom-like impurities in diamond. Coherent manipulation of shallow nitrogen-vacancy (NV) color centers enables the probing of nanoscale ensembles down to $\sim$30 nuclear

spins in atomically thin hexagonal boron nitride (h-BN). The characterization of low-dimensional nanoscale materials could enable the development of new quantum hybrid systems, combining atom-like systems coherently coupled with individual atoms in 2D materials.

3.2 Hexagonal Boron Nitride

Hexagonal boron nitride (h-BN) is an insulating material consisting of equal concentrations of boron (80% ^{11}B, 20% ^{10}B) and nitrogen (close to 100% ^{14}N) in a honeycomb layered structure [60]. The individual atomic layers of h-BN are held together by weak van der Waals interactions, allowing the preparation of samples with varying numbers of layers via mechanical exfoliation (Appendix B). Nanometer-thick h-BN flakes are being extensively used as dielectric spacers and passivation layers for graphene and transition metal dichalcognides [60, 61]. Recent studies have shown that atomically thin h-BN can be the host for interesting quantum defects [62]. We investigate both the electron density distribution and spin-spin interactions in nanoscale h-BN volumes by analyzing the magnetic fields produced by ^{11}B, ^{10}B and ^{14}N spins using nanoscale nuclear quadrupole resonance (NQR) spectroscopy [27, 28].

3.3 Principles of NQR Spectroscopy

Conventional NQR spectroscopy is a powerful tool for chemical analysis that relies on detecting the bulk magnetization of quadrupolar ($I > 1/2$) nuclear spins in a weak magnetic field [50, 49]. The NQR spectrum is determined by the interaction between

the nuclear electric quadrupole moments and the local electric field gradients [63], and is thus dependent upon the electrostatic environment of the measured spins. In the case when the target material is axially symmetric and no external magnetic field is applied, the quadrupolar interaction defines a principal axis for the nuclear spins. For the special case of $I = 3/2$, application of a small magnetic field yields a set of perturbed spin eigenstates with energies that depend on the orientation of the applied field with respect to the principal axis (Fig. 3.1B). NQR spectroscopy yields the transition frequencies and relaxation/decoherence rates, which in turn can be related to various material properties [64, 65] (e.g. chemical composition, bond lengths and angles). However, conventional magnetic resonance methods require macroscopic samples [17] and are not suitable for experiments with atomically thin layers.

3.4 NV-based NQR Spectroscopy of h-BN

In our approach, individual NV centers in diamond are used as sensitive, atomic-scale magnetic field sensors to probe nanoscale h-BN samples under ambient conditions [23, 27, 28, 66]. Formed using ion implantation within several nanometers from the diamond surface, NV centers can have sensing volumes that are many orders of magnitude smaller than most conventional magnetic sensing techniques [67] (Appendix B). In our experiments, a target h-BN flake is transferred onto the surface of a diamond (Appendix B) and a proximal NV center is used to detect NQR signals from small ensembles of nuclear spins within the h-BN crystal (Fig. 3.1A). Importantly, the coherence properties of the NV spin are not affected by the presence of the h-BN flake, indicating that the generation of a new quantum interface between a 2D

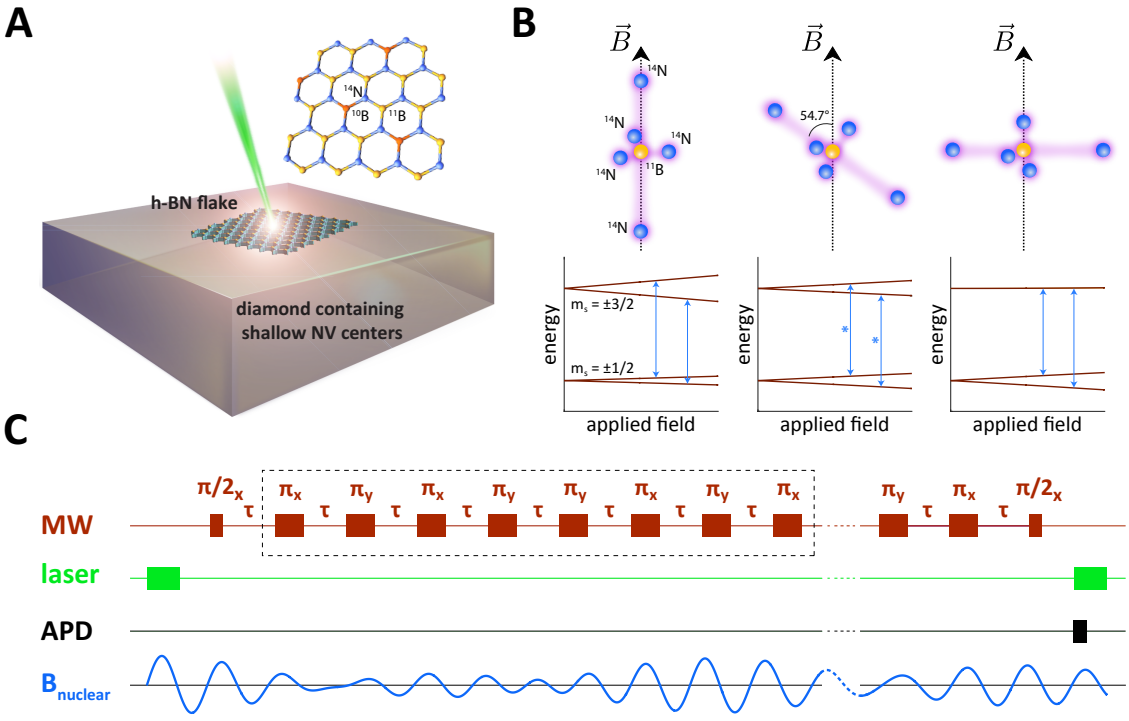

Figure 3.1: **Experimental setup and sensing scheme (A)**, Schematic of experimental setup. The h-BN flake (structure shown on top) is transferred onto a diamond surface. A proximal shallow NV center is used to detect nuclear spins within the h-BN crystal. **(B)**, The dependence of the level structure of a quadrupolar nuclear spin on a small applied magnetic field. The three configurations shown correspond a spin-3/2 object where the external magnetic field is applied parallel, at a 54.7 degree angle and perpendicular to the principal axis. The central transitions are shown by blue arrows. In the middle configuration, the center transitions are degenerate (indicated by *). As a specific example, these configurations are illustrated for the case of a ^{11}B spin in h-BN, surrounded by its nearest five nitrogen atoms. **(C)**, NV center is subject to modified XY8-k pulse sequence used to measure the NQR spectrum. The unit indicated by dashed box is repeated (Appendix B). APD denotes the photodetector measurement window. The magnetic field created by target nuclear spins, containing several Fourier components, is shown at the bottom.

material and diamond is feasible. In order to use the NV center as a nanoscale NQR spectrometer, the NV electronic spin state is prepared in a coherent superposition of the magnetic sublevels $m_s = 0$ and $m_s = 1$ and is periodically modulated with k microwave (MW) π-pulses using modified XY8-k pulse sequence (see Fig. 3.1C and Appendix B). When the local magnetic field spectrum contains a Fourier component near half the modulation frequency, the NV spin state accumulates a net phase (resulting in a measurable population signal) while components at other frequencies are efficiently cancelled [35]. Repetition of this sequence at different modulation frequencies yields the NQR spectrum. While conventional NQR spectroscopy suffers from poor sensitivity due to low thermal polarization under small magnetic field [64], our method relies on measuring the statistical fluctuations of the spin polarization (proportional to $\sqrt{N}$, where N is the number of nuclear spins in the sensing volume), which is independent of the applied field. In the limit of small N, the statistical polarization can be much larger than the thermal polarization, resulting in effective polarizations as high as $\sim 3\%$.

In the ^{11}B ($I = 3/2$) NQR spectrum of a ∼30 nm thick h-BN flake, measured using an XY8-371 sequence (Fig. 3.2A), the resonance frequencies are determined by the quadrupole coupling constant $\overline{Q}$, which is the product of the scalar nuclear electric quadrupole moment and the largest eigenvalue of the local electric field gradient tensor[63]. The extracted $\overline{Q} = 2.9221 \pm 0.0006$ MHz is in excellent agreement with values measured in macroscopic NQR experiments (2.96 ± 0.10 MHz) [68]. The effective sensing volume is determined by the depth of the NV center (6.8 ± 0.1 nm) and corresponds to approximately 20 atomic layers of h-BN material (Appendix B). The exter-

nal magnetic field ($\sim$ 30 G) is applied parallel to the NV symmetry axis, which forms a 54.7 degree angle with the surface normal. In this configuration (Fig. 3.1B), the frequencies of the central transitions ($|m_I = \pm 1/2\rangle \rightarrow |\pm 3/2\rangle$) are degenerate whereas the satellite peaks, corresponding to dipole forbidden $|\mp 1/2\rangle \rightarrow |\pm 3/2\rangle$ transitions, become weakly allowed due to mixing by the magnetic field component perpendicular to the h-BN principal axis. Rotation of the polar angle of the magnetic field away from the NV axis lifts the degeneracy of the central transitions (Fig. 3.2D), in excellent agreement with theoretical prediction (Fig. 3.2E). Figures 3.2B and 3.2C show that when the magnetic field is increased so that the Zeeman and quadrupolar interactions are of the same order, the NQR spectrum becomes very sensitive to the magnetic field angle (sensitivity is $\sim$80 kHz/degree at $\sim$1700 G), enabling precise measurement of the h-BN crystal orientation (in our case perpendicular to the interface).

Measurement of the spectral shifts and linewidths sheds light on the dynamics and interactions governing the nuclear spins. Figure 3.3A shows the $|+1/2\rangle \rightarrow |-3/2\rangle$ ^{11}B NQR resonance alongside an externally applied calibration signal (indicated by the black arrow) whose width corresponds to the Fourier limit, determined by the spin coherence time T_2 of the NV sensor. Deconvolution of this calibration signal from the ^{11}B resonance gives the natural NQR linewidth. A similar procedure yields the linewidth of ^{10}B ($I = 3$) where the observed doublet (Fig. 3.3B) corresponds to two sets of triply degenerate transitions. Figure 3.3C shows the ^{14}N spectrum measured at $\sim$2000 G, where the quadrupolar interaction is manifested as a small shift from the nuclear Larmor frequency (Appendix B). The resonance frequencies and decoherence of NQR lines can also be measured directly (without deconvolution)

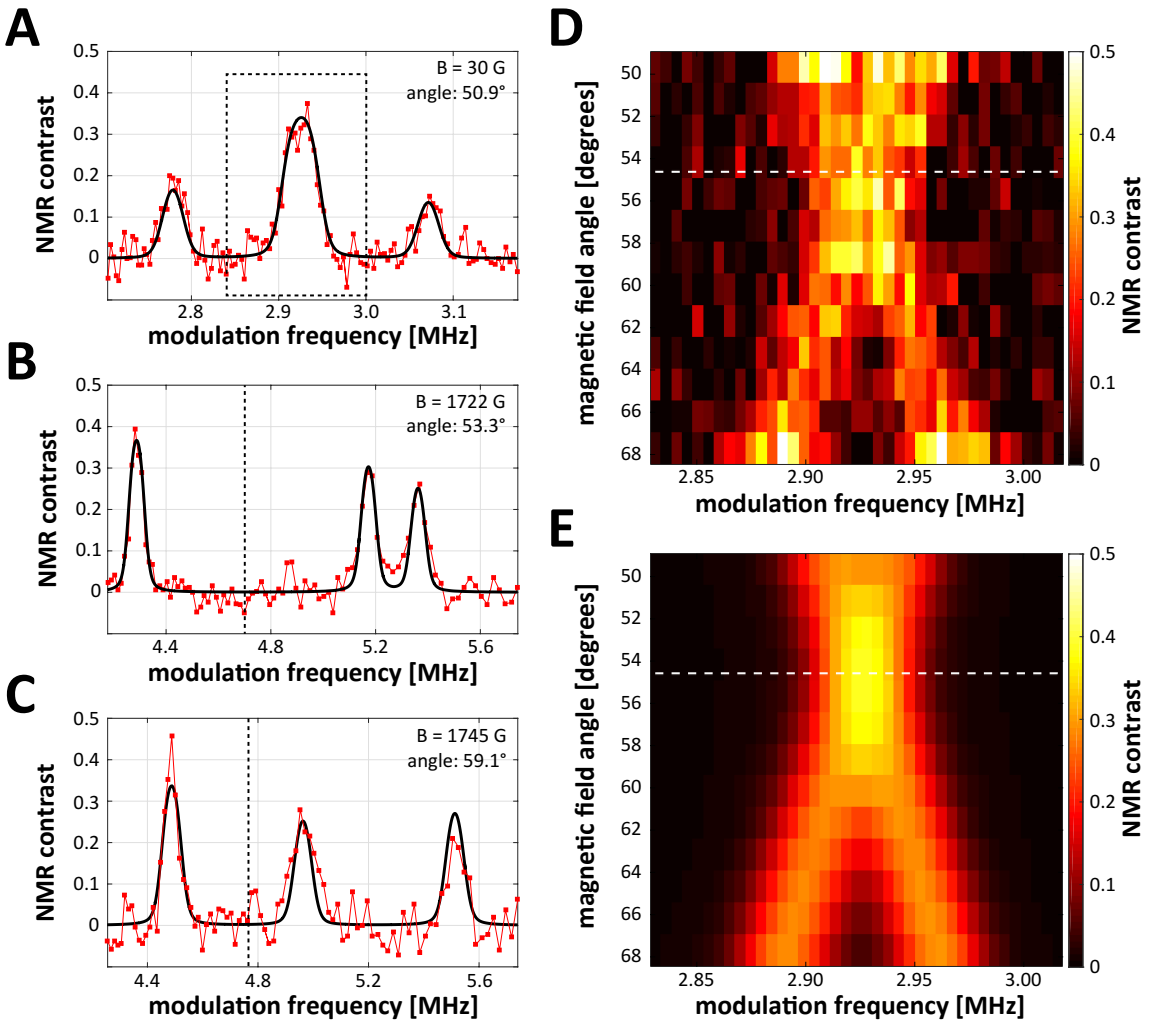

Figure 3.2: **^{11}B NQR spectroscopy of multi-layer h-BN flakes (A)**, NQR spectrum of ^{11}B using XY8-371 with magnetic field (30 G) aligned (approximately) to the angle at which the central transitions become degenerate. The NMR contrast corresponds to the fluorescence difference of the $m_s = 0$ and $m_s = 1$ magnetic sublevels of the NV center. The experimental data (as well as all subsequent spectra presented in this work) are fit to a theoretical model consisting of the local magnetic spectral density convolved with the detector filter function (Appendix B). **(B,C)**, Spectra of ^{11}B using XY8-251 at ∼1700 G taken at two different angles of the magnetic field. Here the Larmor frequency is indicated by the vertical dashed lines. **(D)**, Dependence of the spectrum at 30 G on the magnetic field angle. Here the spectrum was measured in the region denoted by the dotted rectangle in **(A)**. The angle at which the central transitions are degenerate is indicated by horizontal dashed line. **(E)**, Simulation of magnetic field angle dependence shown in **(D)**.

in the time domain using correlation spectroscopy [53] (Fig. 3.3D (top)). Here we apply two identical pulse sequences (similar to XY8-k) separated by a variable free evolution interval T, which can be longer than the coherence time T_2 of the NV sensor and is limited only by the NV population relaxation time T_1. As a result, this technique yields improved spectral resolution at the expense of sensitivity (due to the additional free precession interval T). Figure 3.3D (bottom) shows the resulting ^{11}B time evolution, where the envelope (consistent with the linewidth measured in Fig. 3.3A, here modeled using a Gaussian decay) is modulated by fast oscillations (corresponding to $\overline{Q}$).

Figure 3.3E shows the measured ^{11}B, ^{10}B and ^{14}N linewidths (blue bars) and the corresponding simulated linewidths (orange bars), where we assumed that the spins interact only via magnetic dipole-dipole coupling (Appendix B). The simulated values are in excellent agreement with our measurements, demonstrating that nanoscale volumes of h-BN constitute nearly ideal, dipolar-coupled spin systems. Figure 3.3F shows the measured values of $\overline{Q}$ for ^{11}B, ^{10}B and ^{14}N (blue bars), along with calculated values (orange bars) based on density functional theory (DFT) simulations. Here we used an all-electron model (see Appendix B for details) in the local density approximation (LDA), which yields the calculated quadrupole coupling constants within 2% of the measured values.

3.5 Measurements of Atomically Thin h-BN

Figure 3.4A shows the ^{11}B NQR spectrum of a h-BN monolayer as compared to that of a thick (> 50 nm) flake. The monolayer was characterized using Raman spec-

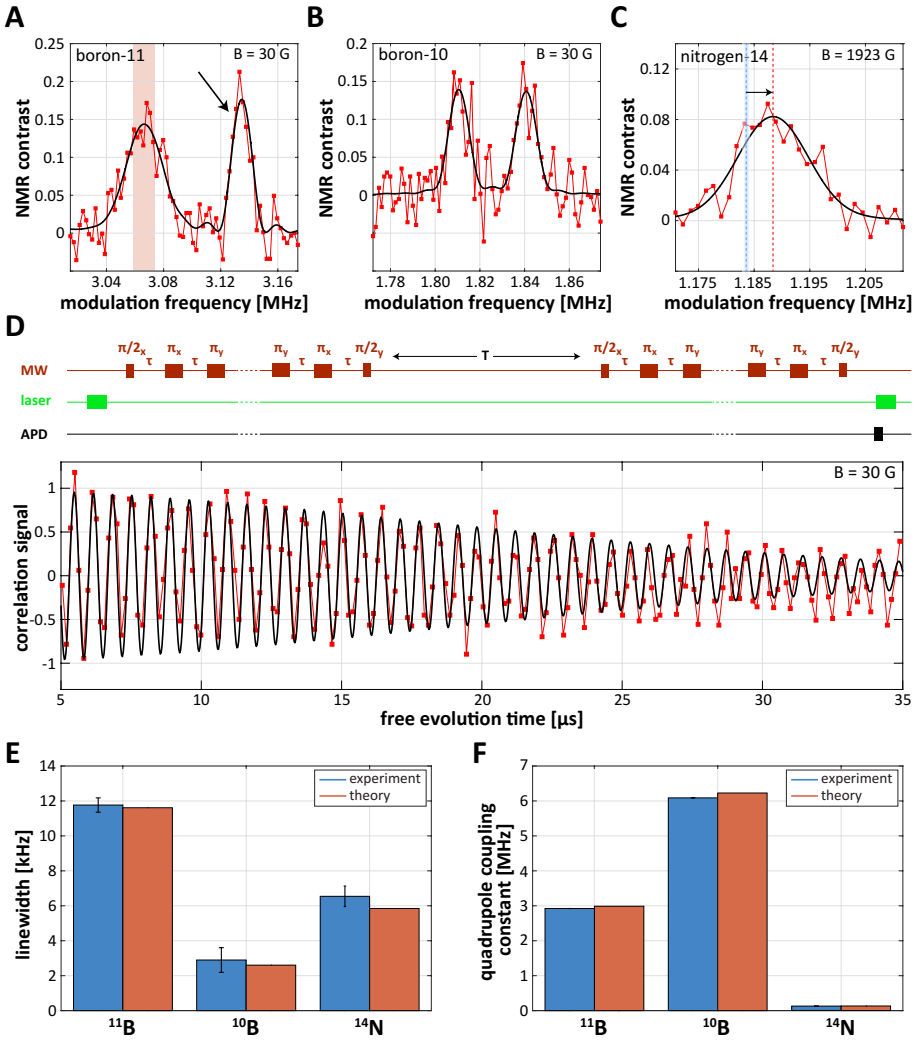

Figure 3.3: **NQR linewidth and quadrupole coupling constant measurements (A)**, NQR spectrum of $|+1/2\rangle \rightarrow |-3/2\rangle$ transition of ^{11}B using XY8-371 at 30 G. A calibration signal (indicated by black arrow) is applied at frequency 1.567 MHz using an external coil. Spectral resolution of NQR signal shown by shaded region. **(B)**, ^{10}B NQR spectrum using XY8-371 at 30 G. The observed spectrum corresponds (approximately) to the degenerate $|0\rangle \rightarrow |\pm1\rangle$, $|\pm1\rangle \rightarrow |\pm2\rangle$ and $|\pm2\rangle \rightarrow |\pm3\rangle$ transitions. **(C)**, ^{14}N spectrum using XY8-187 taken at approximately 2000 G with the field aligned to the NV symmetry axis. At this special angle the $|0\rangle \rightarrow |\pm1\rangle$ transitions are degenerate. The quadrupole interaction is manifested as a small shift of the ^{14}N resonance (indicated by dashed red line) relative to the Larmor frequency (indicated by dashed blue line, with uncertainty shown by blue band). **(D)**, Pulse sequence used for time-domain measurement of linewidth (top). The result of this measurement for ^{11}B is shown at the bottom. The time-trace is the free induction decay of the boron-11 spin, where the slow decay envelope (corresponding to the nuclear spin decoherence) is modulated by fast oscillations (corresponding to the ∼2.9 MHz quadrupole coupling constant). **(E)**, Linewidths, measured in Figs. 3.3A-D, of ^{11}B, ^{10}B and ^{14}N (blue bars) along with simulated values (orange bars) based on dipolar coupling model (Appendix B). Error bars are 1-sigma uncertainties. **(F)**, Measured quadrupole coupling constants of ^{11}B, ^{10}B and ^{14}N (blue bars) along with theoretical values (orange bars) based on DFT. The 1-sigma errors corresponding to ^{11}B, ^{10}B and ^{14}N are 370 Hz, 1.4 kHz and 5.9 kHz, respectively and are too small to be visualized on the scale of this plot.

troscopy, atomic force microscopy (AFM) and second harmonic generation microscopy (see Appendix B). This monolayer signal corresponds to approximately $\sqrt{N} = 30$ polarized ^{11}B spins and exhibits a 17 ± 3 kHz shift of $\overline{Q}$ relative to the bulk value. Figure 3.4B shows the shifts of $\overline{Q}$ and the corresponding linewidths for measurements for several NV centers under a monolayer flake (red) and a bilayer flake (green), as compared to measurements on several thick layers (blue). We find that the bilayer shifts are in between the monolayer and bulk values and the signals for all the NV centers in both the monolayer and bilayer configurations shift in a consistent manner.

The origin of the $\overline{Q}$ shifts can be understood qualitatively by considering the reduction of the dimensionality of the h-BN crystal. As the number of layers in the crystal is reduced we expect that the electric field gradient experienced by a nuclear spin will deviate from its bulk value. A toy model in which in-plane sp^2 bonding electrons are modeled as point charges placed at interstitial sites between the boron and nitrogen ions yields an electric field gradient shift in the correct direction, although the magnitude is a factor of $\sim$20 smaller than the observed value (Appendix B). In order to study this effect quantitatively, we performed DFT simulations of the electric field gradient in the monolayer, bilayer and bulk configurations (Appendix B). These simulations indeed show that reducing the number of layers in the crystal shifts $\overline{Q}$ to lower frequencies. We find that the calculated shifts (-15 kHz for bilayer; -25 kHz for monolayer) are within 50% of the measured values. Remarkably, DFT calculations show that the contribution to the electric field gradient shift resulting from the removal of the outer layers (and their associated charges) accounts for only $\sim$20% of the shift. The dominant contribution arises from a partial redistribution of the elec-

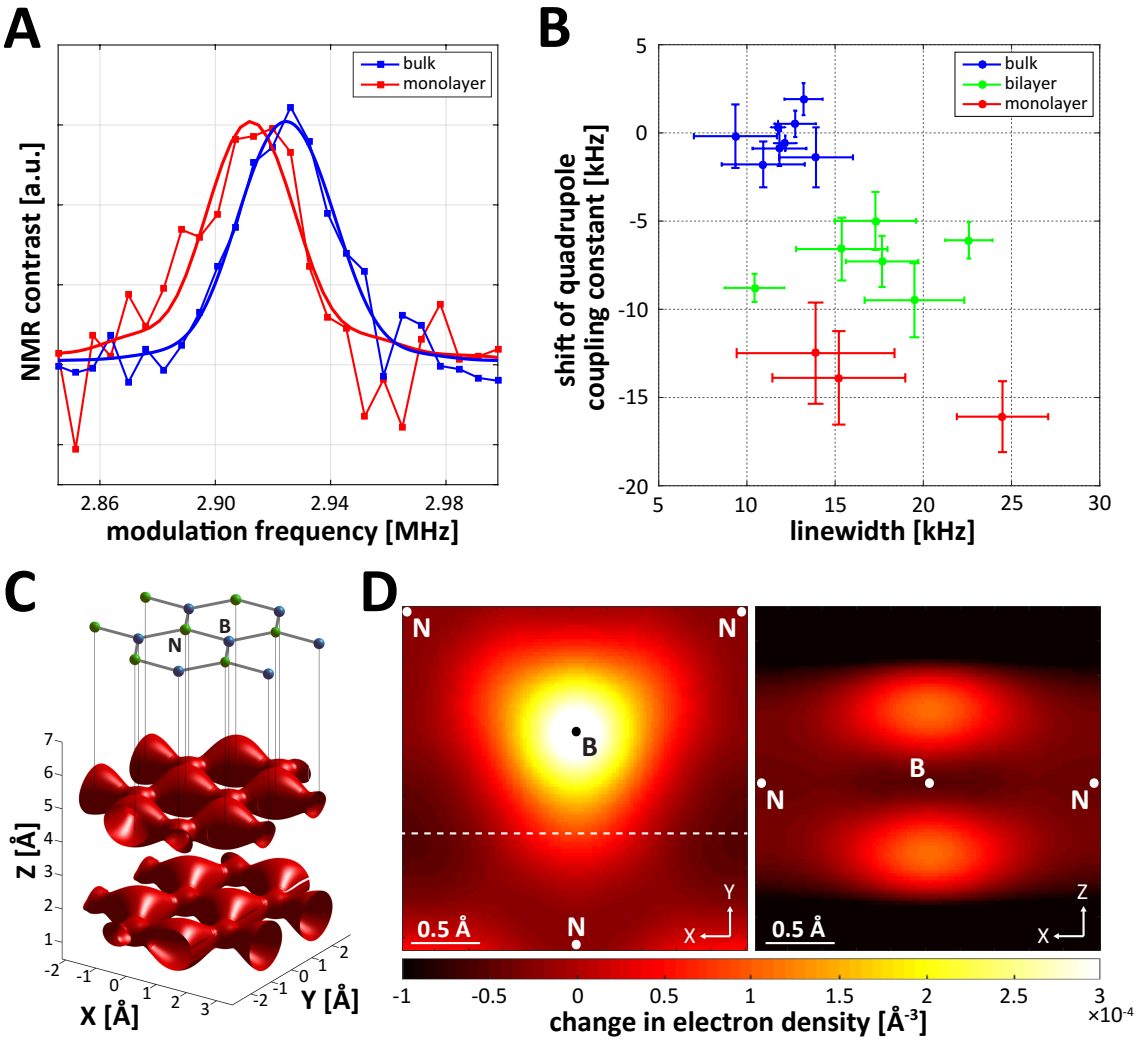

Figure 3.4: **NQR spectroscopy of a h-BN monolayer and bilayer (A)**, ^{11}B NQR spectrum using XY8-187 of thick (greater than 50 nm) h-BN flake (blue) as compared to a monolayer (red). Magnetic field is aligned with respect to NV symmetry axis. Spectra have been normalized so that the resonances have the same magnitude, for comparison. The integration time for the monolayer data was approximately one day, or one hour per datapoint. **(B)**, Values of the shift of $\overline{Q}$ and deconvolved linewidths for several NV centers under a monolayer flake (red), a bilayer flake (green) and five bulk flakes (blue). Error bars correspond to 1-sigma uncertainties. **(C)**, Visualization of electron density for two layers of bulk h-BN, as calculated with DFT. A single contour, corresponding to a density of $\sim$1 Å^{-3} is shown. Boron and nitrogen sites are indicated in the schematic of atomic structure (top) **(D)**, Left panel: visualization of the excess electron caps in the X/Y plane (0.8 Å above the atom plane). A single unit cell is shown. The image corresponds to the difference between the monolayer and bulk electron densities. Right panel: visualization of the excess electron caps in the X/Z plane (Y value indicated by dashed line in left panel). Projected positions of boron and nitrogen ions indicated.

tron density (at the level of 10^{-4} of an elementary charge) from its bulk configuration (see Fig. 3.4C) into a pair of negative charge "caps" above and below boron in the monolayer configuration (Fig. 3.4D). The additional broadening observed in some of the monolayer and bilayer spectra is likely due to dipolar interactions with proximal ^{1}H spins contained within the polycarbonate stamp as well as in the ubiquitous proton layer at the diamond surface, associated with adsorbed hydrocarbons (see [69] and Appendix B), where we probe this layer directly via ^{1}H NMR). Note that in addition to changes in the electrostatic and magnetic environment due to the reduction in layers, differences in lattice strain between the bulk and 2D configurations or the presence of the diamond and polycarbonate substrates may also contribute to shifts and broadening.

3.6 Outlook

These observations provide new insight into the local properties of two-dimensional materials. The sensitivity and spectral resolution can be improved using spin-to-charge conversion readout [51] and advanced photonic structures for improved collection efficiency. With these improvements individual ^{11}B spins can be detected within one second of integration time (Appendix B). The use of correlation spectroscopy (Fig. 3.3D) provides a way of extending the sensing time beyond the coherence time of the NV center. Combined with advanced nuclear decoupling pulse sequences [32] and modest cooling of the diamond samples to $\sim$100 K [36] this method can be used to improve the spectral resolution down to the level of $\sim$1 Hz. Scanning diamond tips[70] or optical super-resolution techniques [57] can be used for nanoscale imag-

ing of local strain fields, localized defects, piezoelectric properties and crystallinity in nanoscale materials [71, 61, 72].

In addition to providing a new sensing modality, our approach can be used to observe and coherently control dynamics of individual nuclear spins in 2D materials. In particular, NV centers can be used as actuators to coherently control nuclear spins in 2D materials [73, 74, 38]. Nuclear spin polarization and control can be achieved by selectively pumping individual quanta of polarization from the NV center to the desired nuclear spin via Hartmann-Hahn Double Resonance [73, 39], while interactions among nuclear spins can be engineered via pulsed RF control [74]. Our experiments show that nuclear dynamics in 2D materials can be limited by dipole-dipole interactions (the additional broadening observed in some of our measurements can likely be controlled by removing proton spins from the diamond surface [27]). Such a coherently coupled system can be used as a novel hybrid platform for quantum information processing [74] and for studying quantum dynamics of isolated strongly interacting nuclear spin systems [75].

Chapter 4

All-Optical Sensing of a Single-Molecule Electron Spin

4.1 Introduction

We demonstrate an all-optical method for magnetic sensing of individual molecules in ambient conditions at room temperature. Our approach is based on shallow nitrogen-vacancy (NV) centers near the surface of a diamond crystal, which we use to detect single paramagnetic molecules covalently attached to the diamond surface. The manipulation and readout of the NV centers is all-optical and provides a sensitive probe of the magnetic field fluctuations stemming from the dynamics of the electronic spins of the attached molecules. As a specific example, we demonstrate detection of a single paramagnetic molecule containing a gadolinium (Gd^{3+}) ion. We confirm single-molecule resolution using optical fluorescence and atomic force microscopy to co-localize one NV center and one Gd^{3+}-containing molecule. Possible

applications include nanoscale and *in vivo* magnetic spectroscopy and imaging of individual molecules.

In our approach the target molecules are covalently attached to the diamond surface, and magnetic sensing of these molecules is performed under ambient conditions using a single shallow NV center as an all-optical nanoscale magnetometer (Fig. 4.1A). Importantly, the shallow NV center is close enough to the surface that it can detect the fluctuating magnetic field produced by the electronic spin of a single paramagnetic molecule, while maintaining good NV center spin coherence and optical properties. We apply this technique to detect a single paramagnetic molecule composed of a gadolinium ion (Gd^{3+}) chelated by an amine-terminated organic ligand (abbreviated as Gd^{3+} molecule below). Single-molecule sensing is confirmed by identifying NV centers that have only a single target molecule within the sensing area on the diamond surface.

4.2 Sample Preparation

Our scheme for covalently attaching molecules to the diamond surface relies on the coupling of the amine-functionalized Gd^{3+} molecule to the carboxylic group on the diamond surface: in order to improve this coupling efficiency, we activated the surface carboxylic group using a water-soluble mixture of 1-ethyl-3-(3-dimethylaminopropyl)carbodiimide (EDC) and *N*-hydroxysulfosuccinimide (NHS) (Fig. 4.1B). This method yielded uniform surface coverage of molecules, with little clumping (see Appendix C), and the surface density of molecules could be controlled by varying the concentration of the Gd^{3+} molecules during the reaction. This procedure can be used to covalently at-

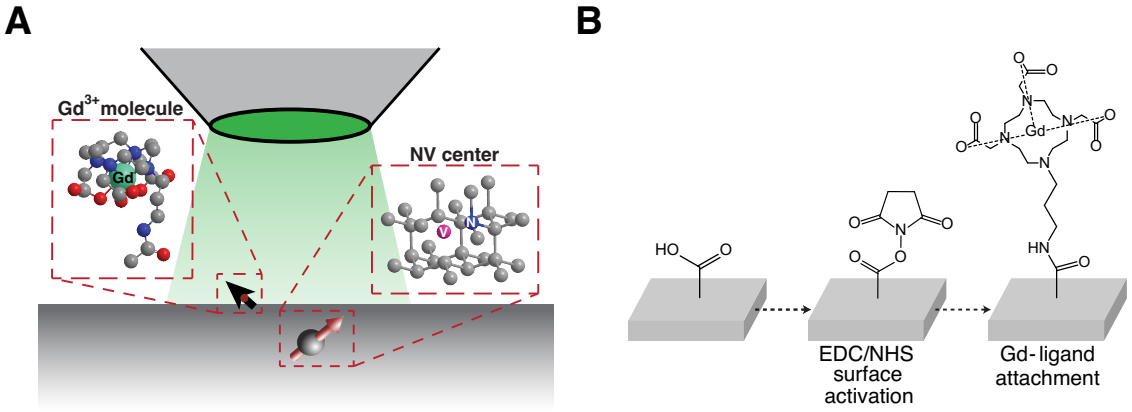

Figure 4.1: **Schematic of measurement setup and sample preparation. (A)** Single-molecule electron spin detection using a single shallow NV center in bulk diamond. Gd^{3+} molecules are attached to the surface of a bulk diamond crystal with widely separated NV centers located at a nominal depth of 6 nm below the diamond surface. NV center optical pumping and fluorescence detection is performed using a confocal microscope (objective shown). **(B)** Chemical procedure for attaching Gd^{3+} molecules to the diamond surface. 1-ethyl-3-(3-dimethylaminopropyl)carbodiimide (EDC) and *N*-hydroxysulfosuccinimide (NHS) are used to activate carboxyl groups on the diamond surface so that they react readily with Gd^{3+} molecules functionalized with amine groups.

tach any water-soluble amine-terminated molecule to the diamond surface, with controlled surface coverage. Since covalent attachment utilizes diamond surface carboxylic groups, the resulting molecular surface density was always less than a monolayer.

In our experiments, we used atomic force microscopy (AFM) to quantify the surface density of these molecules, and to identify their proximity to a given shallow NV center. AFM measurements show that a clean diamond surface exhibits atomically-smooth regions of typically a few square micrometers. When the Gd^{3+} molecules were attached, we observed circular features with mean height of 8 $\mathring{A}$ in the AFM scans. The heights, radii, and density of these features were consistent with single Gd^{3+} molecules covalently attached to the diamond surface (molecular dimensions

were estimated from bond lengths and angles, see Appendix C). As an independent check of the surface molecule density, we added a single Cy3 dye molecule to each Gd^{3+} molecule, and then attached the resulting molecule to the diamond surface using the same chemical procedure as before. We then performed surface fluorescence measurements to deduce the Cy3 surface density, and compared the result to the density of the surface molecules measured using AFM. The results of these independent measurements were consistent with each other, providing strong evidence that the 8 $\mathring{A}$-high AFM features are indeed single molecules (see Appendix C).

In order to determine the proximity of Gd^{3+} molecules to a given shallow NV center with nanoscale precision, we performed a three-step co-localization experiment (Fig. 4.2). First, we coated the diamond surface (via electrostatic attachment) with 100 nm-diameter gold nanoparticles that fluoresce in the same spectral region as the NV centers and are optically resolvable individually. Second, we performed a fluorescence scan to determine the locations of individual NV centers and gold nanoparticles optically (Fig. 4.2A). Finally, we performed AFM topography measurements to determine the locations of gold nanoparticles and Gd^{3+} molecules (Fig. 4.2B). Because the nanoparticles appear in both optical and AFM images, we can use the locations of nanoparticles to combine the fluorescence and AFM measurements and deduce the lateral positions of Gd^{3+} molecules relative to an NV center, with uncertainty of approximately 15 nm (see Appendix C). Figure 4.2C shows an example of this co-localization experiment: an AFM image of Gd^{3+} molecules together with the position of a single shallow NV center, marked by a cross (the circle shows the NV center position uncertainty at one standard deviation). When the Gd^{3+} molecules were removed

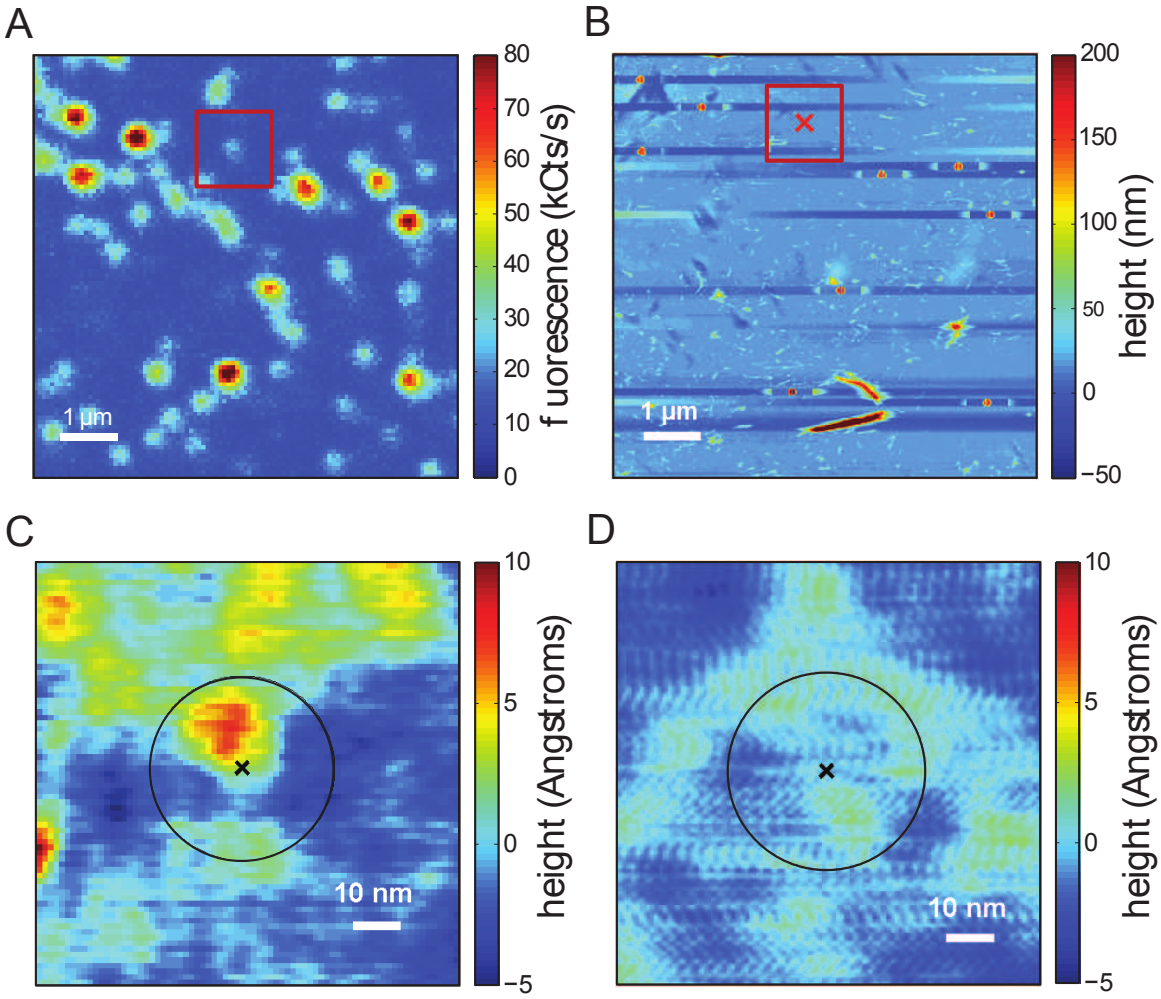

Figure 4.2: **Co-localization of a single shallow NV center and a Gd^{3+} molecule. (A)** Fluorescence image of a 7.5 μm × 7.5 μm area of the diamond crystal, showing several gold nanoparticles (bright spots), and NV centers (less intense spots). Location of a single NV center, marked by a red square, was determined in relation to the gold nanoparticles. **(B)** AFM image of the same region of the diamond surface, showing gold nanoparticles (red dots). The red cross marks the location of the NV center, deduced from the fluorescence image. **(C)** AFM image of the 100 nm × 100 nm region of the diamond surface centered at the location of the NV center (marked by a black cross). The black circle shows the one standard deviation uncertainty in the NV center position, with a single Gd^{3+} molecule present within the circle (bright spot). **(D)** AFM image of the same area as in (C), after Gd^{3+} molecules were removed from the diamond surface.

from the diamond surface, the AFM scan of the same region showed the absence of 8 $\mathring{A}$-high features, confirming the successful removal of molecules (Fig. 4.2D).

4.3 All-Optical Sensing of Gd Spins

Once we located a single Gd^{3+} molecule with a nearby NV center, we performed all-optical magnetic sensing of this molecule. At room temperature the $S = 7/2$ electron spin of the Gd^{3+} ion fluctuates with a relaxation rate (γ_{Gd}) on the order of 10 GHz [76, 77]. These spin-flips give rise to a fluctuating magnetic field at the location of the NV center, with a Fourier spectrum of width $\approx \gamma_{Gd}$. The Fourier component of this fluctuating magnetic field at the frequency corresponding to the zero-field splitting of the NV center ground state spin manifold (S = 1) drives magnetic dipole transitions between these sublevels (Fig. 4.3A). We detected these transitions by first optically pumping the NV center into the $m_s = 0$ sublevel, and then measuring its spin-state-dependent fluorescence after a variable delay time τ (Fig. 4.3B, inset). In the absence of Gd^{3+} molecules, the NV spin-state population difference decayed with rate $\Gamma_{intrinsic}$ due to spin-lattice relaxation. However, when the NV center was in proximity to a Gd^{3+} molecule, the measured NV population relaxation rate increased to $\Gamma_{total} = \Gamma_{intrinsic} + \Gamma_{induced}$ (see Appendix C), which constitutes magnetic sensing of single-molecule electron spin. For example, the red circles in Fig. 4.3B show the result of the NV spin-state relaxation measurements for the NV-Gd^{3+} molecule pair displayed in Fig. 4.2C (the red line is an exponential fit); the blue squares in Fig. 4.3B illustrate the spin-state relaxation rate of the same NV center prior to attachment of the Gd^{3+} molecule. The comparison of these measurements clearly shows a dramatic

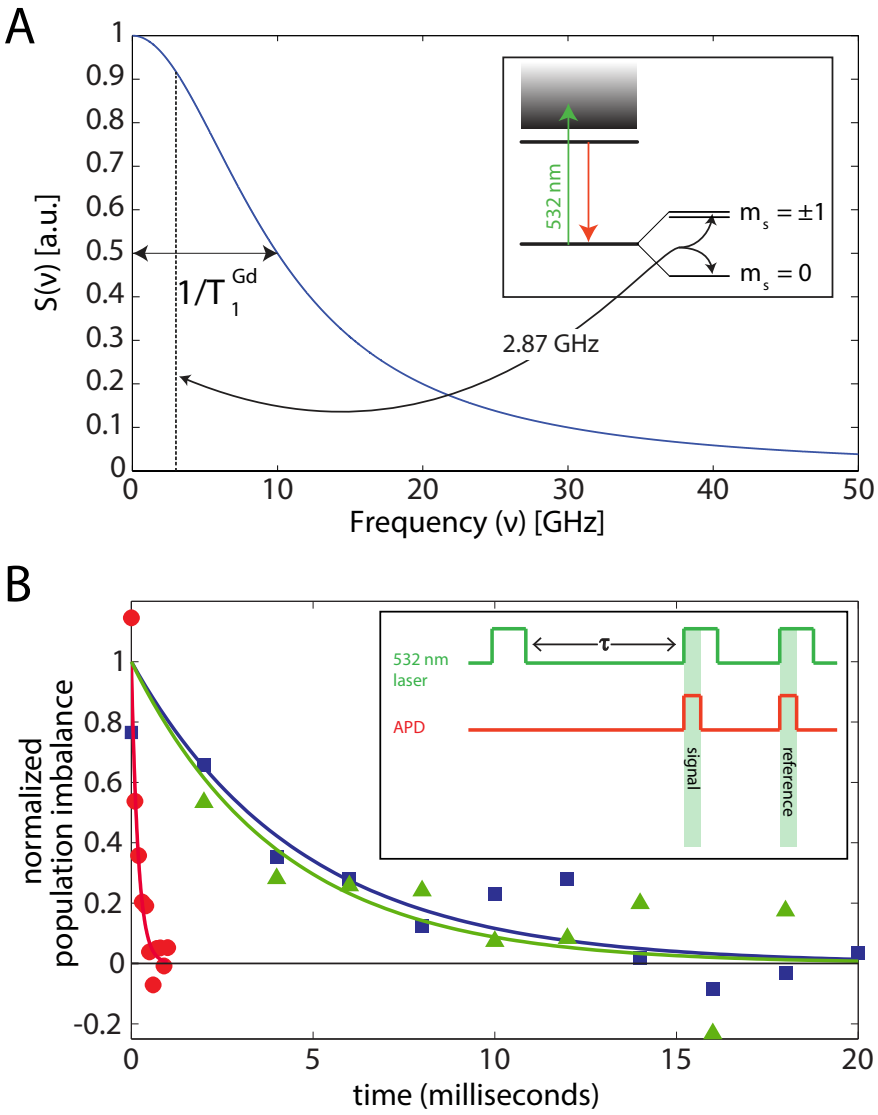

Figure 4.3: **Measurement of magnetic noise from a single Gd^{3+} molecule attached to a diamond surface using a single shallow NV center. (A)** Schematic power spectrum of the fluctuating magnetic field due to relaxation of the Gd^{3+} electronic spin (inset: NV-center electronic excited and ground states, with ground-state spin sublevels). Fourier components of this spectrum near the frequency resonant with the NV center zero-magnetic-field splitting lead to an increase in the NV center spin-state population relaxation rate. **(B)** Demonstration of NV magnetic sensing of a single Gd^{3+} molecule on the surface of bulk diamond. Measurements of the NV center spin-state population difference relaxation and exponential fits. Clean diamond surface: blue squares and blue line. Gd^{3+} molecules attached to the diamond surface: red circles and red line. Re-cleaned diamond surface: green triangles and green line. The AFM image for this NV center is shown in Fig. 4.2C, where it is demonstrated that it is in proximity to a single Gd^{3+} molecule. The scatter of the experimental data points is consistent with photon shot noise, with total averaging time on the order of an hour (not including the time needed to correct for setup drifts). Inset: Pulse measurement scheme for measuring the NV center spin-state relaxation rate. An avalanche photodiode (APD) was used for NV-center red fluorescence detection.

increase of the relaxation rate in presence of a single Gd^{3+} molecule. Once the molecule was removed (Fig. 4.2D), the relaxation returned to the intrinsic rate (green triangles in Fig. 4.3B).

The inset of Figure 4.4 summarizes the measured Gd-induced relaxation rates of for multiple NV-Gd^{3+} molecule pairs, with varying NV-molecule separations. We performed a total of 23 co-localization experiments, together with population relaxation measurements of the corresponding NV centers. In 14 of the 23 co-localization experiments, we could reliably identify single Gd^{3+} molecules and extract the separation between an NV center and a Gd^{3+} molecule; while in the remaining 9 experiments, we could not do so because of finite AFM tip resolution or rough surface topography. Seven of the data points exhibit a significant (greater than two standard deviation) increase in NV spin relaxation, and the corresponding co-localization measurements show the presence of a single Gd^{3+} molecule near the NV center position. As noted above, removal of the Gd^{3+} molecules from the diamond surface resulted in the relaxation rate returning to its intrinsic value in all cases.

A comparison of these data with Monte Carlo simulations (shown as background color plot in the inset of Fig. 4.4) provides further evidence of NV magnetic detection of a single-molecule electron spin. In the simulation, we calculated the probability density of obtaining a particular NV spin relaxation rate for a given NV-Gd^{3+} molecule separation (see Appendix C) within experimental uncertainties. We used an NV center depth of 6 nm, derived from calculations for 3 keV nitrogen ion implantation energy; a mean Gd^{3+} molecule spacing of 20 nm, derived from the AFM and Cy3 measurements described above; and a Gd^{3+} spin-relaxation rate of 10 GHz [76, 77].

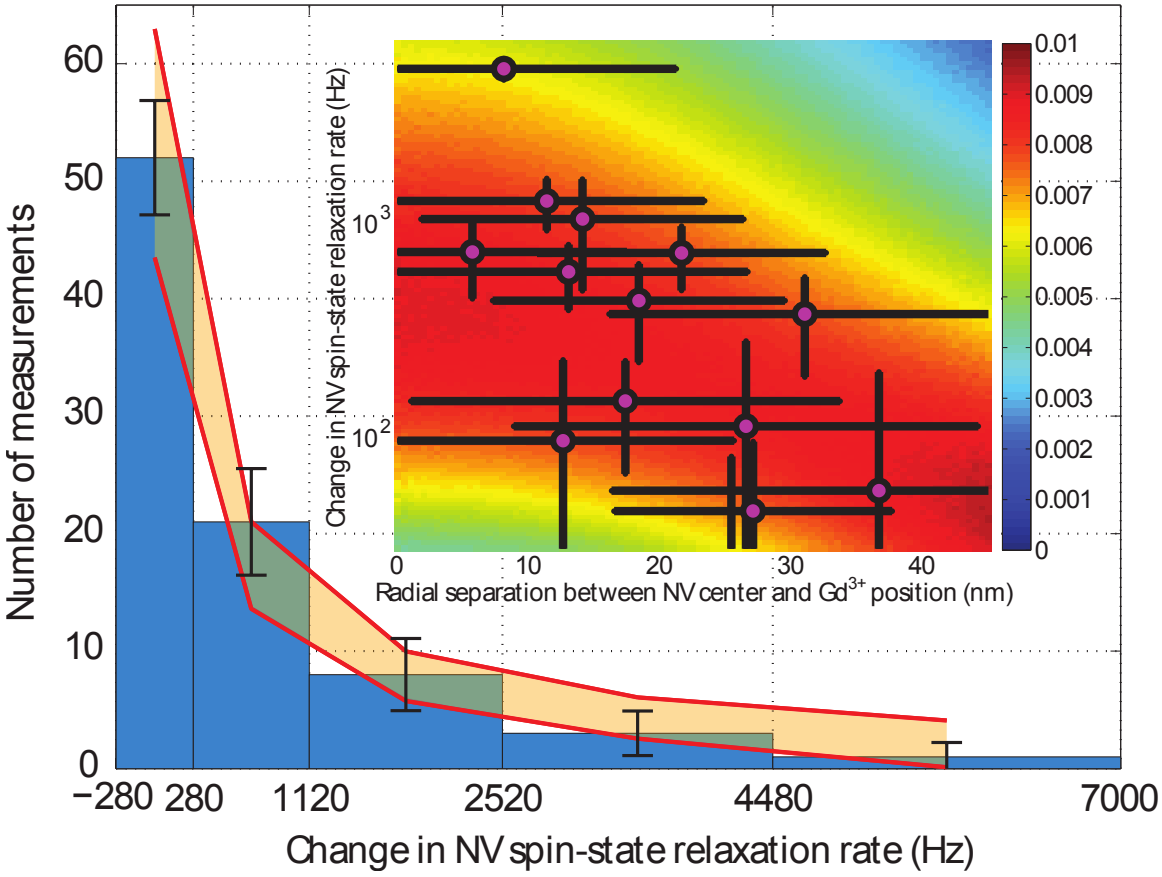

Figure 4.4: **Magnetic noise measurements in the single Gd^{3+} molecule sensing regime.** Results of 85 Gd-induced NV center spin-state relaxation rate measurements, along with a Monte-Carlo simulation band. The experimental data are grouped into five bins, with the error bars calculated by combining bin sampling uncertainty and relaxation rate fitting uncertainty (see Appendix C)). The theoretical band was obtained from Monte Carlo simulations of the experiment, with parameters given in the text. Inset: results of 14 co-localization and NV center spin-state relaxation rate measurements in which a single Gd^{3+} molecule was identified near a single shallow NV center. The background displays the results of Monte Carlo simulations of the experiment, with the color scale indicating the probability density of obtaining a particular NV center spin-state relaxation rate for a given separation between the NV center and the proximal Gd^{3+} molecule. The simulation was performed for 20 nm separation between Gd^{3+} molecules, and NV center co-localization uncertainty of 15 nm. For a quantitative comparison, we performed a two-variable Kolmogorov-Smirnov statistical test, resulting in the Z-statistic value of 1.1, which indicates that the data points are consistent with the simulated distribution (see Appendix C).

As seen in the inset of Fig. 4.4, the experimental data points are consistent with the simulated probabilities (see Appendix C).

Additional evidence for magnetic detection of single-molecule electron spins is provided by an independent set of 85 spin relaxation rate measurements that we performed on 26 shallow NV-centers over several cycles of Gd^{3+} molecule attachment and removal. As shown in the main plot of Fig. 4.4, the resulting data are grouped into five bins, with the error bars calculated by combining the bin sampling and relaxation rate fitting uncertainties (see Appendix C). Also shown in this figure is a band of theoretically calculated NV spin relaxation rates, which we obtained from Monte Carlo simulations of the experiment, with the NV center depth of 6 nm, Gd^{3+} spin-flip rate varying in the range 10 to 20 GHz, and mean Gd^{3+} surface density varying in the range $1/(20\text{ nm})^2$ to $1/(25\text{ nm})^2$. These parameters yield simulated NV-center spin relaxation rate distributions that are consistent with experimental data, again confirming that the observed NV spin relaxation rate increase is due to the proximity of a single-molecule electron spin. While other sets of model parameters can, in principle, be fit to the experimental data, all realistic model fit parameters correspond to regimes in which only a single Gd^{3+} spin contributes to increased NV center spin-state relaxation rate (see Appendix C). The "sensing radius" of an NV-center (defined as the NV-Gd^{3+} molecule separation for which the change in NV-center spin relaxation rate is equal to the measurement uncertainty) is determined to be approximately 12 nm. This means that, with probability over 80%, only a single Gd^{3+} molecule can substantially contribute to the induced NV-center spin relaxation rate even for highest Gd^{3+} molecule densities used.

4.4 Outlook

The detection sensitivity of our experiment is limited by photon shot noise. By monitoring NV-center fluorescence after optical pumping and a relaxation-in-the-dark period of $\approx$ 2 ms, chosen to be on the order of the NV-center intrinsic T_1 time, a single Gd^{3+} molecule spin at a distance of 10 nm can be detected after approximately five minutes of averaging (see Supporting Information). The sensitivity to other paramagnetic species depends on their magnetic moments and the magnitude of their fluctuating magnetic fields at the frequency corresponding to the $m_s = 0 \rightarrow m_s = \pm 1$ transition (see Supporting Information), which can be varied by applying a constant magnetic field. In order to detect radicals with long relaxation times, such as some nitroxides, NV spin coherence relaxation (affecting the measured T_2 time) may be most suitable [78].

Our method for all-optical magnetic sensing of single paramagnetic molecules using shallow NV centers in diamond has potential implications to studies of a wide range of bio-chemical molecules and processes. Together with recent experiments demonstrating NV magnetic sensing of nanoscale ensembles of nuclear spins [28, 27], the combination of single-molecule covalent attachment, co-localization, and magnetic sensing techniques is an important step towards magnetic imaging measurements on individual biological molecules attached to the diamond surface [79]. Our magnetic measurement scheme directly detects the magnetic field created by a paramagnetic molecule, without the need for fluorescent tagging, and can be applied to detect and study small molecules without suffering from blinking or photo-bleaching [80]. Since NV center-based magnetometry was recently shown to be bio-compatible [81], our

approach can also be used for *in vivo* magnetic sensing with single-molecule sensitivity. Specifically, our covalent attachment scheme can be extended to nanodiamonds, functionalizing them to target certain cellular organelles, as well as functionalizing with chemical species (spin traps) that react with short-lived free radicals to produce persistent paramagnetic molecules, which can then be magnetically detected. Since radicals are thought to play a key role in biochemical processes such as cellular signaling, aging, mutations, and death [10, 11, 12, 82], the ability to detect small concentrations (approaching 100 μM, corresponding to mean separation of approximately 25 nm) of short-lived radicals inside living cells could be a powerful tool in studying these processes, with possible applications for disease detection and drug development. Finally, our methods could also find applications in nanoscale and materials science, for example in studies of molecular magnets on a diamond surface, and, when combined with the recently demonstrated scanning probe techniques [83], they could enable imaging of rapidly fluctuating magnetic fields near the surfaces of materials such as superconductors [84], topological insulators [85, 13], and others (ferromagnets, multiferroics, etc).

Chapter 5

Magnetic Resonance Detection of Individual Proton Spins Using Quantum Reporters

5.1 Introduction

We demonstrate a method of magnetic resonance imaging with single nuclear-spin sensitivity under ambient conditions. Our method employs isolated electronic-spin quantum bits (qubits) as magnetic resonance "reporters" on the surface of high purity diamond. These spin qubits are localized with nanometer-scale uncertainty, and their quantum state is coherently manipulated and measured optically via a proximal nitrogen-vacancy (NV) color center located a few nanometers below the diamond surface. This system is then used for sensing, coherent coupling and imaging of individual proton spins on the diamond surface with angstrom resolution. Our

approach may enable direct structural imaging of complex molecules that cannot be accessed from bulk studies. It realizes a new platform for probing novel materials, monitoring chemical reactions, and manipulation of complex systems on surfaces at a quantum level.

5.2 Reporter Spins on Diamond Surface

5.2.1 Background

Our approach to magnetic sensing and imaging makes use of electronic spin-1/2 qubits on the surface of a high purity diamond crystal, coupled to a nearby single nitrogen vacancy (NV) color center a few nanometers below the diamond surface (Fig. 5.1A) [86]. Clean (100) diamond surfaces in ambient conditions are known to host stable electron spins with $S = 1/2$ and g-factor of 2 [87, 88]. These spins have been considered to be deleterious because they are thought to cause decoherence of NV electronic spins within a few nanometers of the diamond surface [89, 90]. However, with proper quantum control, the surface electron spins can be turned into a useful resource. They can be coherently manipulated and measured, thereby serving as a network of quantum "reporters" [91, 92] that probe and "report" the local magnetic environment. The key advantage of such surface spins is their proximity to sensing targets in samples placed on or near the diamond surface. As suggested in recent theoretical work [86], surface electron spins coupled to NV centers can also effectively "amplify" small magnetic field signals, allowing for sub-nanometer localization of individual nuclear spins.

5.2.2 Manipulation and Readout of Reporter Spins

To read out the quantum states of surface electron reporter spins through the NV-reporter magnetic dipole interaction, the nearby shallow NV center is initialized into the $m_s = 0$ sublevel using an optical pumping laser pulse at 532 nm; the spin states of the NV center and of the reporter spins are independently manipulated using pulsed magnetic resonance sequences; and the final quantum state of the NV center is read out using its spin-state-dependent fluorescence (Fig. 5.1B). The $m_s = 0 \leftrightarrow m_s = -1$ NV spin transition is addressed at the angular frequency $\omega_{nv} = \Delta - \gamma_e B$, and the $m_s = +1/2 \leftrightarrow m_s = -1/2$ surface reporter spin transition is driven at frequency $\omega_s = \gamma_e B$. Here $\Delta = 2\pi \times 2.87$ GHz is the NV zero-field splitting, B is the magnitude of the static magnetic field applied along the NV axis, and $\gamma_e = 2\pi \times 2.8$ MHz/G is the electron gyromagnetic ratio (Figs. 5.1C and 5.1D).

The magnetic dipole coupling between the NV center and the surface electron reporter spins is characterized using a generalized spin-echo (double electron-electron resonance or DEER) sequence, shown in Fig. 5.1B. Figure 5.1E shows that for one typical shallow NV center (NV A) the measured spin-echo signal decays on a time scale $T_2^{(nv)} \approx 5$ μs (Fig. 5.1E). However when a π-pulse flips the surface reporter spin population simultaneously with the NV-center π-pulse, the NV-reporter magnetic dipole interaction causes more rapid NV spin echo collapse (Fig. 5.1E, red circles), with a form that depends on the locations of the surface electron spins around the NV center. Because the magnetic dipole interaction is long-range, the NV center can be coupled to multiple surface reporter spins, with the coupling strengths dependent on their positions on the diamond surface. When we treat the diamond with a

strongly-oxidizing reflux mixture of concentrated nitric, sulfuric, and perchloric acids (Appendix D) and repeat the DEER experiment on the same NV center, the DEER signal is clearly modified (Fig. 5.1E, blue triangles), suggesting that this surface treatment "re-sets" the positions of the electron reporter spins and confirming that they indeed reside on the diamond surface.

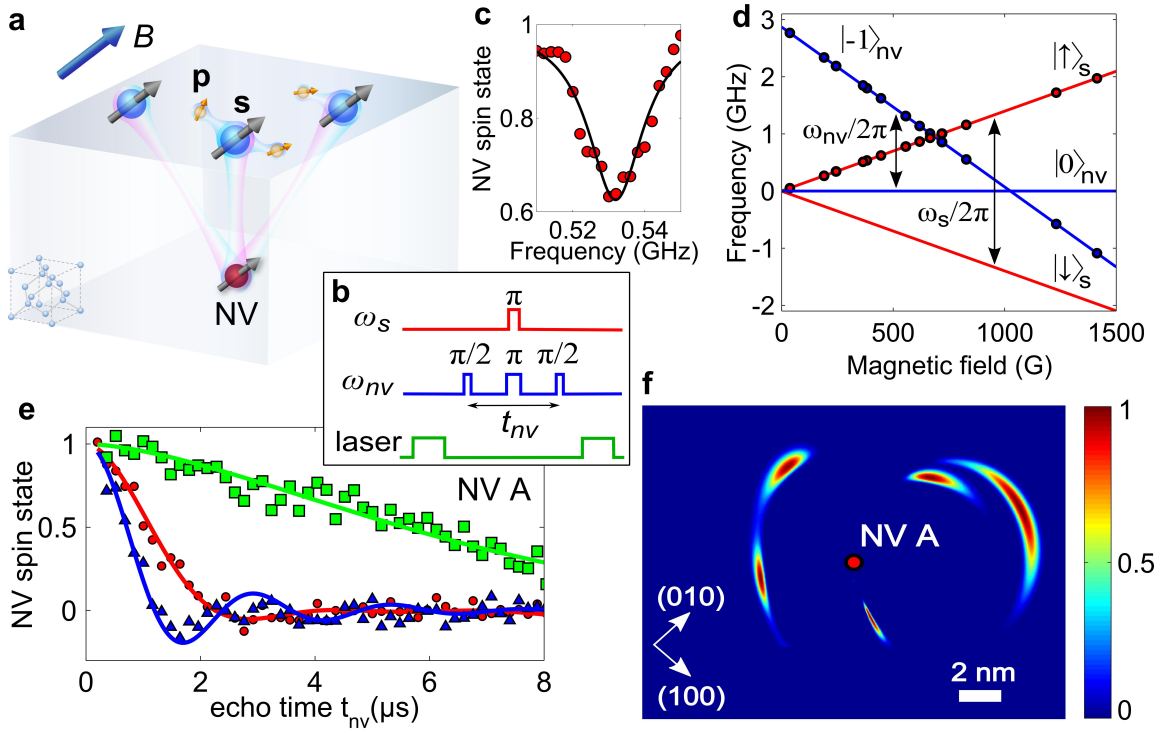

Figure 5.1: **Characterization of surface reporter spins using a shallow NV center. (A)**, Schematic of a network of reporter electron spins, **s**, on the surface of a diamond crystal, that can be used to detect and localize surface proton spins, **p**. **(B)**, DEER pulse sequence. **(C)**, Measured DEER signal as a function of reporter spin frequency ($\omega_s/2\pi$) for fixed t_{nv}. **(D)**, Measured and calculated Zeeman shifts of NV (blue) and reporter (red) spin states. **(E)**, Results of DEER experiment with varying echo delay time t_{nv}. Green squares and line: NV center spin echo decay data and fit. Red circles: DEER measurements. Blue triangles: DEER measurements after oxidizing acid treatment. Red and blue lines are fits using a model with positions of reporter spins on the diamond surface as fitting parameters. In this and subsequent figures, spin state populations are scaled to range between -1 and +1. **(F)**, Probability density map for surface reporter spins near NV A (depth (3.3 ± 0.2) nm), marked by red dot. Arrows mark diamond crystallographic axes; NV center is aligned along (111).

To determine the reporter spin positions, we repeat the DEER measurements

while changing the direction of the applied magnetic field $\boldsymbol{B}$. The magnetic dipole interaction between the NV center and a surface spin depends on their separation and the angle that the vector between them makes with the vector $\boldsymbol{B}$. By rotating $\boldsymbol{B}$, we change this angle, and thus the strength of this interaction (similar methods have been employed to localize ^{13}C spins and other NV centers inside the diamond lattice [93, 94]). By combining the results of the DEER experiments at 7 different magnetic field angles, we reconstruct the positions of 4 reporter spins, constrained to be on the diamond surface, that are nearby to NV A. The positions of these 4 reporter spins relative to NV A are shown in Fig. 5.1F, where the color scale represents the reporter spin position probability density (normalized to unity), corresponding to the best-fit chi-squared statistic, performed with each reporter spin position fixed at the associated map coordinate (Appendix D). In particular, the surface reporter spin closest to the NV center can be localized with nanometer-level uncertainty.

5.2.3 The Reporter Pulse Sequence

The DEER pulse sequence is a useful tool for characterizing the surface reporter spins on the diamond surface, but it is limited by the decoherence time of the shallow NV center, $T_2^{(nv)}$, which is usually on the order of several microseconds. In order to manipulate and probe the reporter spins on time scales longer than $T_2^{(nv)}$, we implement a new "reporter pulse sequence", shown in Fig. 5.2A, inset. This protocol, inspired by Ramsey interferometry in atomic physics [95], consists of two "probe" segments, in which the NV center probes the quantum state of the reporter spin network, separated by an "evolution" segment, in which this state can be manipulated.

In essence, this protocol enables the comparison of the reporter-spin quantum states before and after the evolution segment. Importantly, the duration of the evolution segment is limited by the NV center $T_1^{(nv)}$ time (typically milliseconds), rather than its $T_2^{(nv)}$, thereby extending the evolution timescale by orders of magnitude [96]. In the measurements described below, the duration of the probe segments is kept short (≈ 0.9 μs) to ensure that the NV readout signal is dominated by the coupling to the proximal (most strongly coupled) reporter spin (Appendix D).

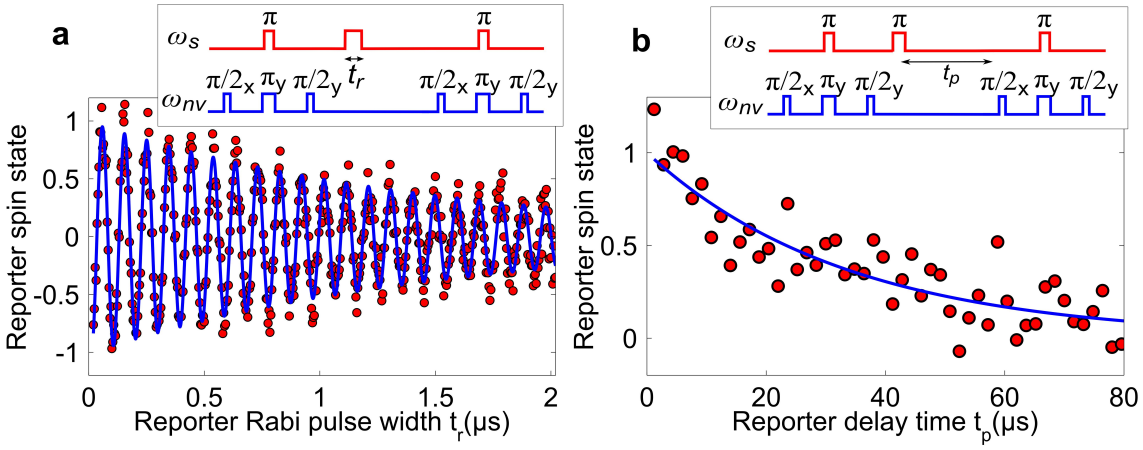

Figure 5.2: **Manipulation and interrogation of the surface reporter spin network with a "reporter" pulse sequence. (A)**, Coherent control of reporter spins. Rabi oscillations between spin states with a variable-width pulse (red points) with an exponentially-damped fit (blue line). Inset: RF pulse sequence. **(B)**, Population relaxation dynamics of the reporter spins (red points) with an exponential-decay fit (blue line). Inset: RF pulse sequence.

To demonstrate coherent control of the surface reporter spins, we vary the length of the radiofrequency (RF) pulse applied at the reporter spin resonance frequency, as shown in Fig. 5.2A. We observe Rabi oscillations with decay time of ≈ 1 μs, which is much longer than the reporter-spin Rabi period, indicating that the pulses can be used for coherent control of the reporter spins. Next, the population relaxation time $T_1^{(s)}$ of the surface spin network is measured by varying the delay time t_p between

the two probe segments in the pulse sequence, Fig. 5.2B. The extracted value of $T_1^{(s)} = (29.4 \pm 2.3)$ μs can be used to place a lower limit of ≈ 5 nm on the mean separation between surface reporter spins: if they were closer together, their mutual magnetic dipole flip-flop interaction would give rise to a shorter population relaxation time (Appendix D). Note that this observation is consistent with the reconstructed spin locations shown in Fig. 5.1F.

5.3 Magnetometry Using Reporter Spins

We next use the reporter electron spins to perform measurements of the magnetic fields on the diamond surface, using the RF pulse sequence shown in Fig. 5.3A. The time-varying magnetic field at the site of a reporter spin gives rise to a phase shift during its spin-echo precession time t_s, which is converted to a change in its spin state population, and is then detected by the NV center. By varying the time t_s, we implement a frequency filter, whereby the measurement is sensitive to magnetic-field Fourier components at angular frequencies ω on the order of $2\pi/t_s$, which show up as reporter spin echo collapses at delay times $t_s = 2\pi k/\omega$, where $k = 1, 3, ...$ [22]. The experimental data exhibit collapses and revivals characteristic of a time-varying magnetic field created by nuclear spins on the diamond surface, precessing in the applied magnetic field B with Larmor frequency $\omega_n = \gamma_n B$, where γ_n is the nuclear spin gyromagnetic ratio. Figure 5.3A shows example results for a particular NV center (NV A), and the data are consistent with the reporter spin coupled to an oscillating magnetic field created by surface protons with root-mean-squared amplitude of $B_n =$ 0.3 G and angular frequency of $\omega_n = 10.6$ μs^{-1}.

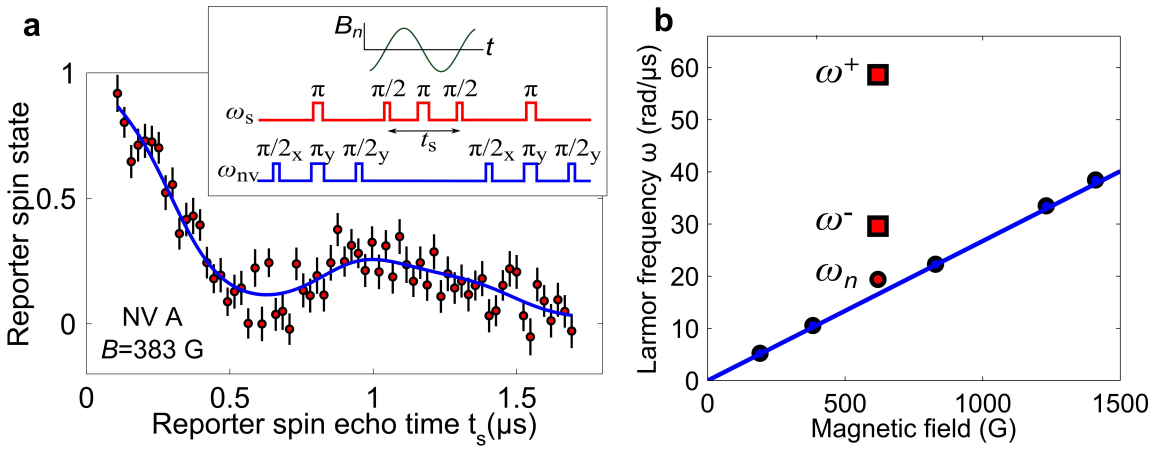

Figure 5.3: **Detection of the magnetic field created by protons, using the surface electron reporter spins. (A)**, Measurement with NV A of the reporter spin echo modulation at $B = 383$ G (red points), fit with a model for echo modulation of a reporter spin coupled to a nuclear spin bath (Appendix D) (fit shown by blue line, reduced chi-squared is 1.2). The error bars on this and subsequent plots show standard deviations of the data points obtained from averaging approximately 5 million repetitions of the pulse sequence, and are consistent with photon shot noise. Inset: reporter echo pulse sequence. **(B)**, Measured values for ω_n at 5 different settings of the applied static magnetic field (blue points), consistent with the proton gyromagnetic ratio of $2\pi \times 4.26$ kHz/G (blue line). The red points mark the ω_n, ω^-, and ω^+ oscillation frequencies, see text.

5.4 Detection of Single Proton Spins

In order to determine the nature of these nuclear spins, we repeat the measurements and analysis at several magnetic fields, and find that the reporter spin echo modulation frequency scales with the applied magnetic field in agreement with the proton gyromagnetic ratio of $2\pi \times 4.26$ kHz/G (Fig. 5.3B, blue points).

Remarkably, however, this simple scaling is not observed at all values of the magnetic field. For example, the data taken with NV A at the magnetic field of 619 G show modulation at frequencies very different from the Larmor frequency expected for the coupling of the reporter spin with a semiclassical proton spin bath (Fig. 5.3B, red points). This high-frequency modulation, seen in the data plotted in Fig. 5.4A, indicates the presence of coherent dynamics between the reporter and proximal proton spins. In order to reproduce and further explore this coherent coupling, another NV center (NV B) is studied at a similar magnetic field. The experimental points, shown in Fig. 5.4B, again display strong modulation, crossing the abscissa axis. This signals coherent population transfer between the proton spin states, mediated by the interaction with a single reporter spin, which cannot occur in the absence of reporter/proton entanglement.

To understand these observations, we analyze the coherent dynamics of a reporter electron spin interacting with proximal proton spins on the diamond surface. The hyperfine interaction between them can be described by the Hamiltonian $H = \hbar a J_z I_z + \hbar b J_z I_x$, where J is the spin operator of the reporter spin, I is the nuclear spin operator, and the z-axis is along the applied magnetic field [97] (Appendix D). This Hamiltonian can be interpreted as an effective hyperfine field, created by the

reporter spin at the site of the proton spin (Fig. 5.4C), which in turn gives rise to splitting of the reporter electron spin states, $\omega^{\pm} = \sqrt{(\pm a/2 - \omega_n)^2 + b^2/4}$, as shown in Fig. 5.4D. This level splitting causes reporter spin echo modulation at frequencies ω^+ and ω^-, with the modulation depth scaling as $2b\omega_n/\omega^+\omega^-$ [97]. When the proton Larmor frequency ω_n is close to half of the hyperfine interaction strength, the reporter spin echo signal is strongly modulated at ω^+ and ω^-, whereas the signal modulation decreases when ω_n is substantially different from a, b. Data taken at such off-resonance magnetic fields can, within their signal-to-noise ratio, be successfully described with a semiclassical nuclear spin bath model (Appendix D).

To analyze the experimental data quantitatively, we compare our measurements with a model that includes coherent hyperfine coupling of a reporter electron spin with a proximal proton, as well as the semiclassical spin bath of protons on the diamond surface (Appendix D). For NV A, the fit to the experimental data shown in Fig. 5.4A yields spin echo modulation frequencies of $\omega^+ = 30\ \mu\text{s}^{-1}$ and $\omega^- = 59\ \mu\text{s}^{-1}$, shown as red squares in Fig. 5.3B, from which we extract hyperfine coupling parameters $a = (66 \pm 18)\ \mu\text{s}^{-1}$ and $b = (52 \pm 20)\ \mu\text{s}^{-1}$. Both the point magnetic dipole interaction and the contact hyperfine interaction contribute to the parameters a and b: $a = a_0 + (\hbar\gamma_e\gamma_n/r_n^3)\,(1 - 3\cos^2\theta_n)$, and $b = (\hbar\gamma_e\gamma_n/r_n^3)\,(3\cos\theta_n \sin\theta_n)$, where a_0 is the contact hyperfine interaction, r_n is the separation between the reporter spin and the proton spin, θ_n is the angle that the vector between them makes with the applied magnetic field (Appendix D). The low chemical reactivity of the reporter spins (see discussion below) suggests that direct overlap between the reporter spin wavefunction and a surface proton is likely minimal, implying that the magnitude of

a_0 is small. If we neglect a_0, the position of the proximal proton with respect to the reporter spin most strongly coupled to NV A is $r_n = (2.2 \pm 0.2)$ $\mathring{A}$ and $\theta_n = (26 \pm 15)^\circ$, with the azimuthal angle not quantified by the data. The data for NV B (Fig. 5.4B) are consistent with the presence of two proximal protons, coherently coupled to the reporter spin: their best-fit positions are $r_n^{(1)} = (2.6 \pm 0.2)$ $\mathring{A}$, $\theta_n^{(1)} = (47 \pm 3)^\circ$ and $r_n^{(2)} = (3.2 \pm 0.2)$ $\mathring{A}$, $\theta_n^{(2)} = (19 \pm 4)^\circ$, as shown in Fig. 5.4E in a probability density map. In order to quantify the uncertainty in the proton positions due to our lack of information about the magnitude of the contact interaction, we use 40 μs^{-1} as the range of possible values for a_0, since this is the measured contact hyperfine interaction with the OH-group proton in a hydroxylated carbon-centered radical [98], similar to our presumed bonding configuration (see below). For this range of a_0, the locations of the detected protons are constrained to be within the contours shown in Fig. 5.4E. We note that in diamond a_0 is likely be much smaller due to positive electron affinity of the oxidized diamond surface.

While the origin of the reporter spins cannot be unambiguously determined from this study alone, they are likely unsaturated (or "dangling") bonds, localized near the top two carbon atom layers. We observe that they are stable in ambient conditions over time scales of many days, which indicates that they are sterically protected from direct chemical reactions with species outside the diamond lattice. Nevertheless, the reporter spins are close to the surface, since they experience strong hyperfine coupling with surface protons, and their positions change when exposed to the strongly-oxidizing 3-acid mixture (this surface treatment also modifies the results of the reporter echo experiments, see Appendix D). Furthermore they are absent from

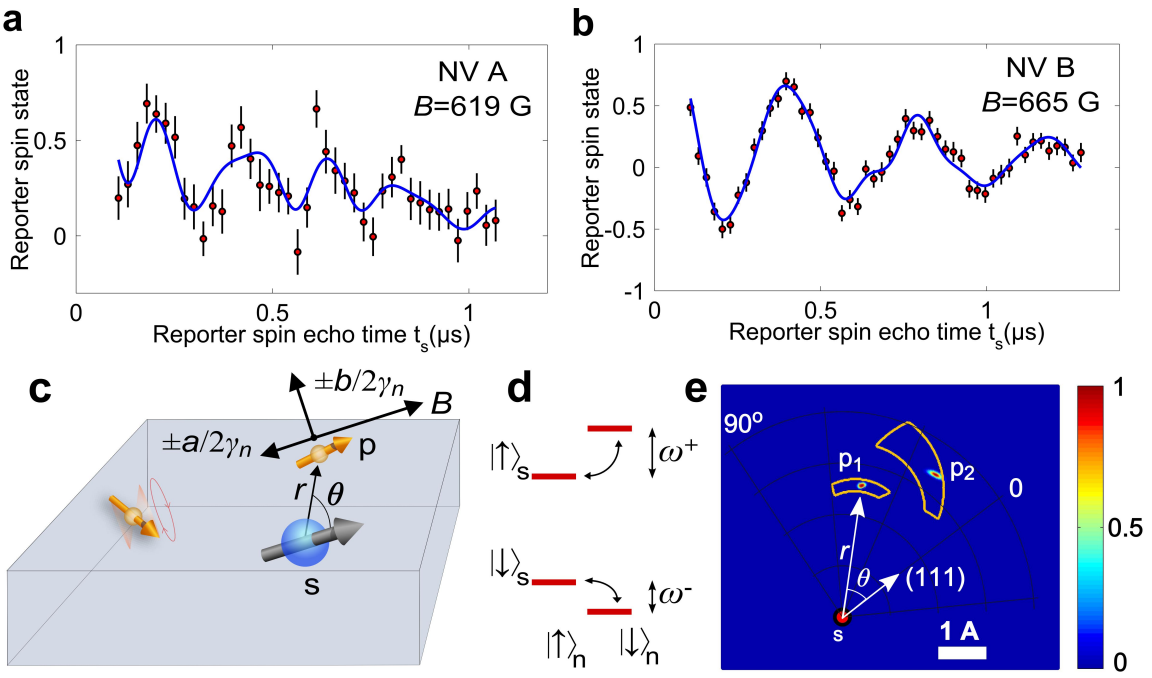

Figure 5.4: **Coherent dynamics between individual surface electron and proton spins. (A)**, Reporter spin echo modulation for NV A at B = 619 G (red points), and fit using a model with the reporter qubit, proximal to the NV center, coupled to one proton spin (blue line). **(B)**, Reporter spin echo modulation with NV B at B = 665 G (red points). The best-fit (blue line, reduced chi-squared value of 1.1) corresponds to a model with the reporter qubit, proximal to the NV center, coupled to two proton spins. **(C)**, Schematic illustrating hyperfine coupling between the reporter electron spin, s, and the proton spins (gold arrows). The weakly-coupled protons far from the reporter spin precess in the applied magnetic field B at the Larmor frequency. The proximal proton spin, p, experiences the vector sum of B and the effective hyperfine fields $\pm a/2\gamma_n$ and $\pm b/2\gamma_n$, whose signs depend on the reporter spin state. **(D)**, Energy level diagram for the coupled system of the reporter spin and proximal proton spin. **(E)**, Localization of the two proximal proton spins (p_1 and p_2) relative to the reporter spin, s, that is most strongly coupled to NV B. The color scale shows the probability density for each proton location, extracted from a fit to the data shown in **(B)** (Appendix D).

the diamond surface (no DEER signals) after the diamond is annealed at 465°C in an O_2 atmosphere [43] (Appendix D). The detected protons are likely from covalently-bound hydroxyl (OH) or carboxyl (COOH) groups terminating the clean diamond surface under ambient conditions [99]. Their relative locations are consistent with density-functional-theory calculations of these groups on an oxidized diamond surface [100].

5.5 Outlook

NV centers in diamond have emerged as a nanoscale magnetic-field sensor with exquisite sensitivity under ambient conditions [22, 23, 37], enabling magnetic sensing and imaging of single electron spins [101, 102, 24] and nanoscale ensembles of nuclear spins [27, 28, 69, 103]. Our method extends these recent advances into a new domain, enabling magnetic resonance detection and imaging on surfaces with single nuclear spin resolution. Several paths towards further improving the sensitivity and the broad applicability of our approach should be noted. It may be possible to extend the electron reporter spin coherence times using decoupling pulse sequences, together with dilution of the proton magnetic moments on the diamond surface, e.g. by deuteration. Individual addressing of the reporter spins may be achievable with a careful choice of the duration of the "reporter pulse sequence" readout intervals, as described above, or via frequency separation of different reporter qubits using a practical magnetic field gradient (less than 1 G/nm) [88]. Polarization transfer from the NV center to the reporter spins [104], and possibly to strongly coupled surface nuclear spins, may allow initialization and entanglement of the surface spin network [105] and hyperpolariza-

tion of target nuclei. The hyperfine field gradient, produced by the reporter spins, may also be used to encode spatial information for magnetic imaging. Finally, other reporter spin candidates, such as stable nitroxide radicals, can be explored, possibly providing a more flexible route for sensing applications because they can be directly attached to a reactive site of interest on a molecule under study.

Our approach, with improvements in the coherence properties and robust control of the reporter spins, can enable a number of unique applications. NMR and MRI of individual molecules and proteins under ambient conditions is one direction that can be pursued. Reporter-based sensing may also find applications in measurements of magnetic fields near complex materials, such as superconductors and topological insulators. Beyond applications in sensing and imaging, our approach provides a powerful new platform for coherent manipulation of coupled electronic and nuclear spins on surfaces or in 2D materials, which can be used to realize and explore new classes of self-assembled quantum systems [74].

Chapter 6

Conclusions and Outlook

Extending the functionality of conventional magnetic sensing methods to the nanoscale is an interesting and important challenge in science and technology. Our approach provides a set of techniques, complementary to conventional NMR and EPR, that can be used to achieve this goal. These tools open the door to many unique and exciting applications.

In Chapter 2 we showed that shallow NV centers can be used to probe individual ubiquitin protein molecules attached to the proximal diamond surface. While such shallow NV centers have been shown to have poor coherence properties [33], as compared to bulk NV centers, we showed that a novel surface termination technique as well as a readout scheme based on quantum-logic can be used to dramatically reduce the decoherence rates of these NVs and therefore improve their sensitivities. In fact we demonstrated sensitivities sufficient to detect a single proton spin within one second of integration time. As shown in Section 2.6, this technique can potentially be used to probe the structure and conformational dynamics of complex biological

molecules at the single-spin level.

In Chapter 3 we demonstrated the first magnetic resonance spectroscopy of an atomically thin material. This experiment made use of NV-based NQR to extract information about the electric field gradients, bond orientations and nuclear spin dephasing rates at various atomic sites within the target crystal of hexagonal boron nitride. We also showed that the NQR spectrum is modified as the number of layers in the crystal approaches the monolayer limit and concluded that this shift is likely the result of a rearrangement of the electron density into lobes of negative charge around the boron sites. Our technique can potentially used to characterize systems not easily accessible via conventional measurement and interfacing techniques. With some modest improvements in sensitivity and spectral resolution, as outlined in Section 3.6, our technique can be used to realize a hybrid quantum system, consisting of a 2D material interfaced with a single-spin defect in diamond, that could potentially be used for quantum information processing and quantum simulation.

Chapter 4 reports on the realization of all-optical, room-temperature detection of an individual electronic spin. Specifically, we showed that by monitoring the population relaxation rate of a shallow NV center, we can detect the magnetic noise created by the fluctuations of an individual proximal Gd spin. Our method allows the direct detection of paramagnetic ions or molecules without the need for fluorescent labelling. This technique can be used to study fast spin motion associated with conformational changes in biomolecules. By utilizing shallow NV centers in diamond nanocrystals, our technique could potentially be used to detect short-lived free radicals in living cells.

Finally, in Chapter 5, we demonstrated the ultimate limit of magnetic resonance sensitivity - namely, the detection of a single nuclear spin at room temperature. Here we made use of a network of stable spin defects associated with the diamond surface to amplify dipolar interactions with proximal nuclear spins. An individual shallow NV center was then used to readout the state of this reporter spin network. In this work, we demonstrated the detection of individual proton spins with sub-angstrom resolution.

Despite these demonstrations, there is still much that remains unknown about the properties of these systems. For example, the interactions of shallow NV centers with sources of magnetic noise associated with the diamond surface, as well as methods to remove these noise sources, remain poorly understood. An additional source of uncertainty is the chemical environment of the diamond surface, which needs to be understood and well-controlled before the most exciting applications outlined above can be realized. Nevertheless, our experiments provide compelling evidence that NV centers can be used to realize novel applications in nanoscale sensing as well as provide a powerful new solid-state platform for quantum information processing.

Appendix A

Supporting material for Chapter 2

A.1 Chemical Attachment of Ubiquitin Proteins

Ubiquitin proteins (human, recombinant) labelled with 2H and 13C were purchased from Giotto Biotech (G03UBQ01). Ubiquitin proteins labelled with 13C were purchased from Medical Isotopes, Inc (C3225). Unlabelled Ubiquitin was purchased from Sigma-Aldrich (709417). The reagents 1-ethyl-3-(-3-dimethylaminopropyl) carbodiimide hydrochloride (EDC), N-hydroxysuccinimide (NHS) and ethylenediamine were purchased from Sigma-Aldrich (E6383, 130672 and E26266, respectively).

We use carbodiimide crosslinker chemistry to attach ubiquitin proteins to the diamond surface. This procedure is designed so that any carboxylic acids terminating the diamond are conjugated to the linker molecule ethylenediamine, which is subsequently attached to the C-terminus of the protein. Conjugation of primary amines with carboxylic acids is achieved by crosslinking with the carbodiimide compound 1-ethyl-3-(-3-dimethylaminopropyl) carbodiimide hydrochloride (EDC). N-hydroxysuccinimide

(NHS) is included in the reaction mixture to improve coupling efficiency.

A.2 NMR Sensing Area

For an NV center with depth d and a uniform, two-dimensional distribution of spins on the diamond surface, we determine that more than 70% of the NMR signal comes from a region of area πd^2 directly above the NV center. We denote this region as the sensing area.

For typical NV depths (d $\sim$ 4 nm) and the measured protein spacing ($\sim$21 nm), we expect to observe a 2H NMR signal with amplitude of ¿ 1% in approximately 10% of NV centers. Of these detection events, more then 90% are expected to be due to an individual protein. Here, detection of an individual protein is defined as the case in which more than 70% of the observed signal is created by a single protein.

A.3 Diamond Sample Processing

All experiments presented in this work were performed using two (100)-oriented, unpolished, electronic-grade diamond samples (henceforth referred to as samples A and B), consisting of a 50 μm ^{12}C-enriched (99.999% abundance) layer epitaxially-grown using plasma-enhanced chemical vapor deposition on a natural-abundance diamond substrate (Element Six). The concentrations of substitutional nitrogen and boron impurities were less than 5 parts per billion (ppb) and 1 ppb respectively. Sample A was implanted using a $^{15}N^+$ dosage of 10^9 cm^{-2} and an implantation energy of 2.0 keV. It was annealed in vacuum using the following procedure: (a) 6 hour ramp

to 400°C, (b) 6 hours at 400°C, (c) 6 hour ramp to 800°C, (d) 8 hours at 800°C and (e) 6 hour ramp to room temperature. Sample B was implanted using a $^{15}N^{+}$ dosage of 10^{10} cm^{-2} and an implantation energy of 1.6 keV. It was annealed in vacuum using the following procedure: (a) 2 hours at 200°C, (b) 1 hour ramp to 800°C, (c) 1.5 hours at 800°C and (d) 2 hour ramp to room temperature.

After vacuum annealing, the samples were cleaned in a boiling 3-acid mixture (equal volumes of H_2SO_4, HNO_3, and $HClO_4$) for three hours. In order to reduce the decoherence rates of shallow NV centers, the samples were annealed in an oxygen environment (Tystar, Mini Tytan 4600) for 4 hours at 465°C. The oxygen anneal followed the following procedure: (a) ramp to 465°C for 2 hours, (b) anneal at 465°C for 4 hours, (e) ramp down to 250°C for 2 hours. The samples were placed in a Piranha solution (2:1 mixture of concentrated H_2SO_4 and 30% hydrogen peroxide) immediately before and after the anneal.

A.4 Optical Setup

We used a home-built, inverted confocal microscope to address individual NV centers. Here optical excitation was performed using a 532 nm diode-pumped solid-state (DPSS) laser (Information Unlimited, MLLIII532-200-1) modulated with an acousto-optic modulator (Isomet Corporation, 1250C-974) in a double-pass configuration. NV center fluorescence was separated from the reflected excitation beam using a dichroic beamsplitter, filtered using 532 nm notch and 633 nm long-pass filters and collected using a fiber-coupled single-photon counting module (PerkinElmer, SPCM-AQRH-14-FC). A Nikon Plan Fluor 100x oil immersion objective (NA = 1.3)

was positioned under a microwave-frequency coplanar waveguide, used to hold the diamond sample. A layer of objective immersion oil (Micro Video Instruments, Inc, MVA22024) was placed between the waveguide and the sample to reduce aberrations and increase collection efficiency. Lateral steering of the laser beam was performed using a closed-loop scanning galvanometer (Thorlabs GVS012) while the vertical position of the focus was controlled with a with a piezoelectric stage (Physik Instrumente P-721 PIFOC). The acousto-optic modulator and the single-photon counting module were gated using TTL pulses produced by a 500 MHz PulseBlasterESR-PRO pulse generator from Spincore Technologies.

A.5 Coherent Control of Two-Qubit Register

A.5.1 Manipulation of Electronic Spin Qubit

We apply microwave-frequency (MW) drive fields using a coplanar waveguide fabricated on a silicate glass substrate (Ted-Pella, Inc, #260320). Here we use a Sharon Thermal Evaporator to deposit a three-layer metal structure consisting of a 50 nm titanium adhesion layer, 1000 nm of of copper and 300 nm of gold. The metal surface is then coated with Shipley S1813 positive photoresist and a coplanar transmission line structure is generated using optical lithography (SUSS MicroTec MJB4). The resist is developed using Microposit MF CD-26 developer and the exposed metal is removed using Au etch and hydrofluoric acid (HF). The unexposed resist is removed with acetone and the finished waveguide is cleaned using Buffered Oxide Etch (7:1). In order to prevent the diamond sample from coming into direct contact with the

metal, the waveguide is coated with a 20 nm film of aluminum oxide (Al_2O_3) using Atomic Layer Deposition (Cambridge NanoTech, S200).

We apply strong MW pulses at the carrier frequency $\frac{\gamma_e}{2\pi}B - \Delta$ in order to rotate the electronic spin irrespective of the ^{15}N spin state (Hadamard, Pauli-X and Pauli-Y gates). Here $\Delta = 2.87$ GHz is the NV center zero-field splitting, $\gamma_e = 1.76\times10^{11}$ s^{-1} T^{-1} is the electron gyromagnetic ratio and B is the magnitude of the external magnetic field applied along the NV symmetry axis. For all measurements presented in this work, strong MW pulses are 12-25 ns in duration. The MW signal is generated by a Stanford Research Systems SG384 signal generator where the built-in IQ modulation inputs are used to control the x and y quadrature amplitudes of the output signal. The MW pulses are gated by a dual-output Tektronix 3052C Arbitrary Function Generator (AFG), which is in turn triggered by TTL pulses. A second AFG controls the IQ modulation of the output signal.

We apply a weak MW π-pulse resonant with one of the ^{15}N hyperfine transitions to implement the C-NOT gate (henceforth referred to as C-NOT$_{e|n}$)

$$|0\downarrow\rangle \rightarrow |0\downarrow\rangle, |1\downarrow\rangle \rightarrow |1\downarrow\rangle, |0\uparrow\rangle \rightarrow |1\uparrow\rangle, |1\uparrow\rangle \rightarrow |0\uparrow\rangle, \tag{A.1}$$

where the electronic spin is flipped conditioned on the nuclear spin state. Here the carrier frequency of the tone is set to $\frac{\gamma_e}{2\pi}B - \Delta - A/2$, where $A \approx 3.05$ MHz is the hyperfine coupling between the NV center electronic spin and the ^{15}N nuclear spin. The MW signal is synthesized using a Rhode&Schwarz SMC100A signal generator, frequency-doubled with a Mini-Circuits ZX90-2-36-S+ multiplier and power boosted with a Mini-Circuits ZHL-16W-43-S+ amplifier. Setting the duration of the π-pulse to $\sim$280 ns yields a frequency profile with a zero at the detuning that corresponds

to the other ^{15}N hyperfine line, effectively applying a 2π-pulse to the off-resonant transition.

An external static magnetic field was applied using a permanent neodymium magnet on a goniometric stage (Edmund Optics, #66-532).

A.5.2 Modified XY8-k Sequence

We optically-polarize the NV center electronic spin into the state $|0\rangle$ and apply a Hadamard gate to create the superposition state $(|0\rangle + |1\rangle)/\sqrt{2}$. The spin then undergoes k periodic π-phase rotations separated by intervals of free evolution, after which a final Hadamard gate converts any accumulated phase into a measurable population difference. In contrast to the canonical XY8-k sequence, the $k+2$ spin rotations are implemented using a train of identically-spaced MW pulses where the amplitudes are controlled via IQ modulation. The phases of the π-pulses follow the pattern

$$[X]_1[Y]_2[X]_3[Y]_4[Y]_5[X]_6[Y]_7[X]_8 \cdots [X]_{k-2}[Y]_{k-1}[X]_k, \tag{A.2}$$

where $[X]$ and $[Y]$ correspond to Pauli-X and Pauli-Y gates, respectively. In order to cancel the DC component of the magnetic field noise spectrum we require an odd number of π-pulses. As an illustration, an XY8-11 sequence in this scheme would have the form

$$[X]_{\pi/2}[X]_\pi[Y]_\pi[X]_\pi[Y]_\pi[Y]_\pi[X]_\pi[Y]_\pi[X]_\pi[X]_\pi[Y]_\pi[X]_\pi[X]_{\pi/2}, \tag{A.3}$$

with each pulse separated by time interval τ.

A.5.3 Manipulation of Nuclear Spin Qubit

A radio-frequency (RF) drive field is delivered through a copper coil positioned above the diamond sample. We use a high-purity alumina rod as the inductor core in order to efficiently dissipate heat created by the high power RF pulses.

The RF tone at the carrier frequency $A - \frac{\gamma_N}{2\pi}B$, where γ_N is the ^{15}N gyromagnetic ratio, is used to implement the C-NOT gate (henceforth referred to as C-NOT$_{n|e}$)

$$|0\downarrow\rangle \rightarrow |0\downarrow\rangle, |0\uparrow\rangle \rightarrow |0\uparrow\rangle, |1\downarrow\rangle \rightarrow |1\uparrow\rangle, |1\uparrow\rangle \rightarrow |1\downarrow\rangle. \tag{A.4}$$

Here the signal is synthesized using a second Rhode&Schwarz SMC100A generator and amplified using a ENI A-500 RF amplifier. For all measurements presented in this work the RF pulses are 50-60 μs in duration.

A.5.4 SWAP Operation

A SWAP operation, which interchanges the nuclear and electronic spin states, is equivalent to the sequence C-NOT$_{e|n}$ – C-NOT$_{n|e}$ – C-NOT$_{e|n}$. For repetitive readout of the electronic spin populations, where the coherence of the final state is irrelevant, the last C-NOT$_{e|n}$ gate is not strictly necessary.

A.5.5 Quantum Logic-based Readout

The inefficiency of optical readout of NV centers is due to the fact that the optical excitation used for readout also re-polarizes the NV center spin before enough photons can be detected to accurately determine its state. In order to improve the readout fidelity, we utilize a two-qubit quantum register, consisting of an NV center electronic

spin and its proximal ^{15}N nuclear spin. Here, the nuclear and electronic qubits are coupled through the hyperfine interaction, resulting in the level structure shown in Fig. A.1, where the $|0\rangle$ and $|1\rangle$ correspond to the $m_s = 0$ and $m_s = 1$ magnetic sublevels of the NV electronic spin, respectively, while the states $|\downarrow\rangle$ and $|\uparrow\rangle$ denote the eigenstates of the ^{15}N nuclear spin ancilla. As shown in Fig. 2.1B of the main text, by applying a SWAP quantum gate followed by an electronic repumping operation, an arbitrary electronic spin state $\alpha\,|0\rangle + \beta\,|1\rangle$ is stored in the ancilla qubit, resulting in the state $|0\rangle \otimes (\alpha\,|\downarrow\rangle + \beta\,|\uparrow\rangle)$, irrespective of the initial nuclear spin state. Subsequently, a controlled-NOT (C-NOT) gate, implemented using a weak MW pulse resonant with one of the ^{15}N hyperfine transitions (blue arrow in Fig. A.1), creates the entangled state $\alpha\,|0\downarrow\rangle + \beta\,|1\uparrow\rangle$. An optical measurement (of duration 800 ns) then projects this state into either $|0\downarrow\rangle$ or $|1\uparrow\rangle$ and re-polarizes the electronic spin. The sequence of C-NOT and optical readout is then repeated with each additional cycle (of duration 1.1 μs) yielding more information about the initial spin populations.

In all measurements employing repetitive readout, the transition frequency of the $m_s = 0$ and $m_s = 1$ magnetic sublevels of the NV center is tuned as far as possible from the excited state level anti-crossing [42]. This ensures that the effect of the depolarization of the ^{15}N nuclear spin mediated by hyperfine coupling in the excited state of the NV center is minimized.

In order to reduce the effect of spurious noise (e. g. slow drift of the ESR line), the repetitive readout sequence is repeated twice. The first run includes the magnetic signal acquisition while the second run includes instead a single strong MW pulse, used for normalization. For all NMR measurements presented in this work, where

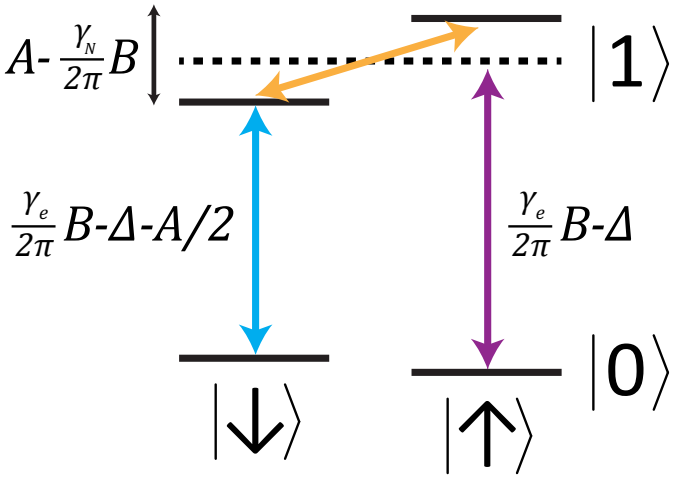

Figure A.1: **The level structure of the two-qubit register consisting of a NV center electronic spin and its associated ^{15}N nuclear spin.** The driving fields used for coherent control of the register are indicated. Here $A = 3.05$ MHz is the splitting of the nitrogen hyperfine levels, γ_N is the ^{15}N gyromagnetic ratio and B is the magnitude of the external magnetic field applied along the NV symmetry axis.

repetitive readout is utilized, we use 500 readout cycles.

A.6 Theoretical Model of NMR Spectrum

Application of the modified XY8-k pulse sequence with free evolution interval τ leads to a population signal of the form $S(\tau) = \frac{1}{2}\Big(1 - \cos\phi\Big)$, where ϕ is the total accumulated phase at the end of the pulse sequence. Averaging over many realizations of the experiment and assuming that the accumulated phase is Gaussian-distributed with zero mean, the signal becomes

$$S(\tau) = \frac{1}{2}\Big(1 - e^{-\langle\phi^2\rangle/2}\Big) \tag{A.5}$$

Here the phase variance $\langle\phi^2\rangle$ is given by [35]

$$\langle\phi^2\rangle = \frac{\gamma_e^2}{2\pi}\int_{-\infty}^{\infty} d\omega S_B(\omega)|g(\omega\tau)|^2, \tag{A.6}$$

where γ_e is the electron gyromagnetic ratio, $S_B(\omega)$ is the double-sided magnetic spectral density and $|g(\omega)|^2$ is the detector filter function. For the modified XY8-k sequence, the filter function is given by [106]

$$|g(\omega\tau)|^2 = 2\sin^2\left(\frac{(k+1)\omega\tau}{2}\right)\tan^2\left(\frac{\omega\tau}{2}\right), \tag{A.7}$$

where we have neglected evolution during the spin rotations. As shown in [35], the spectral density for a uniform spin distribution of thickness h is given by the expression

$$S_B(\omega) = 9\rho\Big(\frac{\mu_0\hbar\gamma_n}{4\pi}\Big)^2\Big(\tilde{\Gamma}_x f^{x,x}(\omega) + \tilde{\Gamma}_y f^{y,y}(\omega)\Big), \tag{A.8}$$

where ρ is the spin density, μ_0 is the vacuum permeability, $\hbar$ is the reduced Planck's constant and γ_n is the gyromagnetic ratio of the target nuclear spin species. The geometrical factors $\tilde{\Gamma}_x$ and $\tilde{\Gamma}_y$ depend on the NV depth d and the angle α of the NV symmetry axis relative to the surface normal and are given by the expressions

$$\tilde{\Gamma}_x(\alpha) = -\frac{\pi}{3}\left(\frac{3\cos(4\alpha)-35}{768}\right)\left[\frac{1}{d^3} - \frac{1}{(d+h)^3}\right] \tag{A.9}$$

$$\tilde{\Gamma}_y(\alpha) = \frac{\pi}{3}\left(\frac{3\cos(2\alpha)+5}{192}\right)\left[\frac{1}{d^3} - \frac{1}{(d+h)^3}\right]. \tag{A.10}$$

For the special case of a [100]-oriented diamond, where the NV symmetry axis makes a $\sim$54.7° angle relative to the surface normal, these expressions reduce to

$$\tilde{\Gamma}_x = \frac{7\pi}{432}\left[\frac{1}{d^3} - \frac{1}{(d+h)^3}\right] \tag{A.11}$$

$$\tilde{\Gamma}_y = \frac{\pi}{144}\left[\frac{1}{d^3} - \frac{1}{(d+h)^3}\right]. \tag{A.12}$$

The transverse correlation functions $f^{x,x}$ and $f^{y,y}$ are given by

$$f^{x,x}(\omega) = \frac{2}{Tr(\mathbf{1})}\sum_{n,m}\Big|\langle n_z|\, I_x\, |m_z\rangle\Big|^2\delta\big(\Delta\omega_{n,m}-\omega\big) \tag{A.13}$$

$$f^{y,y}(\omega) = \frac{2}{Tr(\mathbf{1})}\sum_{n,m}\Big|\langle n_z|\, I_y\, |m_z\rangle\Big|^2\delta\big(\Delta\omega_{n,m}-\omega\big), \tag{A.14}$$

where $Tr(\mathbf{1})$ denotes the trace of the identity operator for the target nuclear spin, $\mathbf{I} = \{I_x, I_y, I_z\}$ are the generalized spin matrices, and the indices n and m correspond to the complete set of spin eigenstates of the nuclear spin where the energy difference of the states is given by $\omega_{n,m}$. Note that each pair of eigenstates corresponds to two spectral lines, one at a positive and one at a negative frequency.

A.6.1 NV Center Depth and Decoherence Rate Measurements

In this work the depths of NV centers are measured by immersing the sample into microscope objective immersion oil and detecting the amplitude of the ^{1}H NMR signal created at the NV center by the proximal proton spins. For the special case of protons ($I = 1/2$), the spectral density in Eq. A.8 corresponds to the expression

$$S_B(\omega) = \pi\langle B^2\rangle\delta(\omega - \omega_0) + \pi\langle B^2\rangle\delta(\omega + \omega_0). \tag{A.15}$$

where the magnetic field variance $\langle B^2\rangle$ is given by the expression

$$\langle B^2\rangle = \frac{5\rho\mu_0^2\mu_N^2 g_p^2}{1536\pi d^3}. \tag{A.16}$$

Here ρ is the proton density, μ_0 is the vacuum permeability, μ_N is the nuclear magneton, $g_p \approx 5.59$ is the proton g-factor and d is the NV center depth. In order to take into account the dephasing and motional effects of the proton bath, we replace the delta functions above with Lorentzian functions, parameterized by the width γ. With this substitution, the spectral density becomes.

$$S_B(\omega) = \frac{\langle B^2\rangle\gamma}{\gamma^2 + (\omega - \omega_0)^2} + \frac{\langle B^2\rangle\gamma}{\gamma^2 + (\omega + \omega_0)^2}. \tag{A.17}$$

We fit the measured ^{1}H NMR spectrum to the expressions given in Eq. A.5 using the field spectrum from the expression above. The fitting parameters γ and d yield the coherence timescale of the proton bath and the depth of the NV center, respectively. A more complete treatment of this topic is provided in [35].

The decoherence rates of NV centers are estimated by sampling the amplitude of the magnetic field noise spectrum $S_B(\omega)$ at different frequencies. Here we sweep the free evolution interval τ between π-pulses in the XY8-k sequence. The data is fit to the expression [33]

$$D(\tau) = \frac{1}{2}\Big(1 - \exp\left[-(\Gamma\tau)^p\right]\Big), \tag{A.18}$$

where Γ is the NV center decoherence rate and p is a value ranging from 1-3. All NMR measurements presented in this work are processed by subtracting the observed NMR signal from D and dividing by $1 - 2D$ to reflect the reduced contrast created by NV decoherence. Here the levels of 0 and 1 correspond to the fluorescence rates of the $m_s = 1$ and $m_s = 0$ magnetic sublevels of the NV center, respectively.

A.6.2 Detector Sensitivity and Spectral Resolution

In order to characterize the sensitivity we consider a monochromatic signal with random phase at frequency $2\pi\omega_0$, corresponding to the field spectrum

$$S_B(\omega) = \pi\langle B^2\rangle\delta(\omega - \omega_0) + \pi\langle B^2\rangle\delta(\omega + \omega_0). \tag{A.19}$$

The maximum of the NMR signal at this frequency occurs at $\tau_0 = \pi/\omega_0$ and is given by the expression

$$S(\tau_0) = \frac{\gamma_e^2}{\pi^2}\langle B^2\rangle\tau_0^2(k+1)^2 \tag{A.20}$$

Here we have made the small signal approximation $e^{-\langle\phi^2\rangle/2} \approx 1 - \langle\phi^2\rangle/2$. The maximum signal is achieved when the total sequence duration $\tau_0(k+1)$ is chosen to be approximately equal to the decoherence time T_2. Given a total averaging time T and a readout time T_R, $T/(T_2 + T_R)$ measurements can be performed, yielding the minimum detectable magnetic field variance δB^2, given by

$$\delta B^2 \approx \frac{\pi^2}{\gamma_e^2 T_2^2}\sqrt{\frac{T_2 + T_R}{T}}. \tag{A.21}$$

While this field variance is limited by spin projection noise, the dominant source of noise in our experiment is photon shot noise, which can be parameterized by the the NV center fluorescence readout fidelity [22]

$$\mathcal{F} = \left[1 + 2(\alpha_0 + \alpha_1)/(\alpha_0 - \alpha_1)^2\right]^{-\frac{1}{2}}. \tag{A.22}$$

We define the sensitivity figure of merit of our nuclear spin sensing experiment as the number N of ^{1}H spins, situated on the diamond surface directly above the NV center, that can be detected with unity signal-to-noise ratio after $T = 1$ second of integration. The magnetic field variance of a single ^{1}H spin in this configuration is given by

$$B_p^2 \approx \frac{(\mu_0 \hbar \gamma_p)^2}{16\pi^2 d^6}, \tag{A.23}$$

where $\gamma_p = 2.68{\times}10^8$ s^{-1} T^{-1} is the proton gyromagnetic ratio, d is the NV center depth and μ_0 is the vacuum permeability. Thus, the sensitivity is given by

$$N \approx \frac{1}{\mathcal{F}}\frac{\delta B^2}{B_p^2}, \tag{A.24}$$

which yields Eq. 1 of the main text.

Due to the dependence of $S(\tau)$ on the variance of the magnetic field, the NMR signal created by a single nuclear spin depends on the NV-spin separation r approximately as $1/r^6$. For an extended structure (e. g. an isotropic volume of protons, see below) the scaling could be significantly weaker. When the dimension of the structure is smaller than r, as is the case for the small protein considered in this work, the scaling is not appreciably different from that of a single nuclear spin.

The spectral resolution Γ is given by the linewidth of the filter function and is fundamentally limited by the decoherence rate $1/T_2$. In the small signal approximation the FWHM linewidth W_F of the filter function in Eq. A.7 is given by

$$W_F \approx \frac{0.886}{(k+1)\tau}. \tag{A.25}$$

As illustrated in Fig. 2.2A of the main text, the oxygen surface treatment combined with quantum logic-based readout yields shallow NV centers with sensitivities improved by more than a factor of 500 as compared to the same NV centers before surface treatment and using conventional readout. In Fig. A.2A we compare the sensitivity gain to a selection of previous work reported in the literature [27, 48, 89, 33]. Only studies where the NV depths were measured directly [35], as opposed to estimated from ion implantation simulations, are considered. Here the bars represent the mean values of the measured NV center sensitivities. The error bars correspond to 75% quantiles for cases when more than a single NV center was measured. We use a readout fidelity $\mathcal{F} = 0.2$ for the present case when quantum logic-based readout is used (as shown in Fig. 2.1C). A value of $\mathcal{F} = 0.03$, corresponding to a typical fluorescence rate of 100 kCts/s, a detection window of 250 ns and a fluorescence contrast of 35% between the $m_s = 0$ and the $m_s = \pm 1$ states of the NV center, is assumed

for all other cases. In all cases presented here, the coherence time was measured with an XY8-k pulse sequence with k between 64 and 448. In cases where the coherence time was measured using more than one value of k, we chose the maximum reported coherence time for the present analysis.

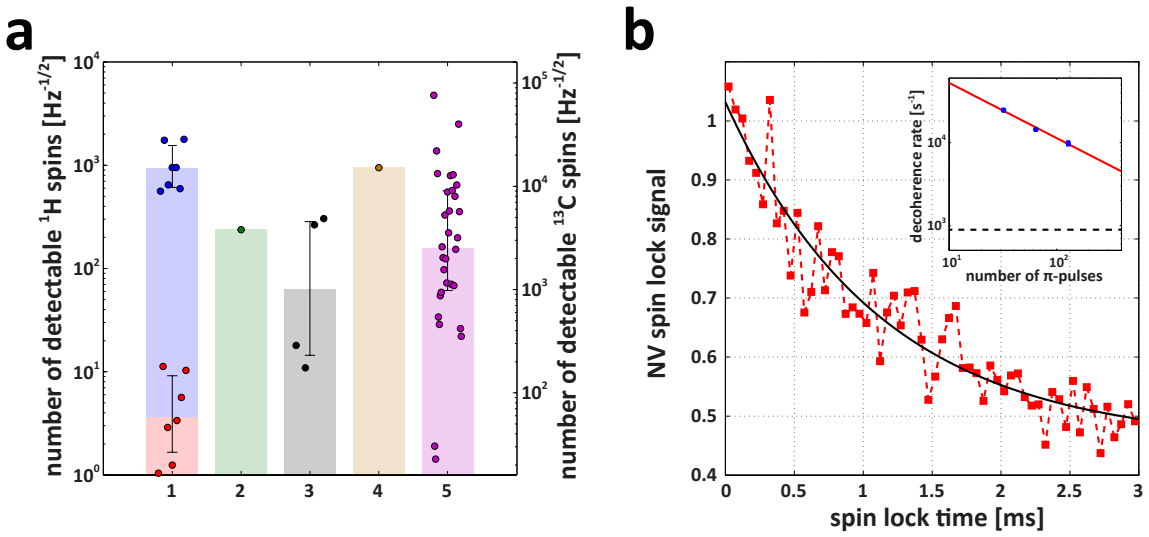

Figure A.2: **Minimum detectable number of ^{1}H and ^{13}C spins as measured in our experiments, and compared with previous work reported in the literature. (A)** The bars represent the following: **1)**. Measurements presented in Fig. 2.2A of the main text before surface treatment and quantum logic-based readout (blue points) and after surface treatment and employing quantum logic-based readout (red points). **2)**. Staudacher et al., Science 339, 561563 (2013), **3)**. Loretz et al., Applied Physics Letters 104, 033102 (2014), **4)**. Myers et al., Physical Review Letters 113, 027602 (2014), **5)**. Romach et al., Physical Review Letters 114, 017601 (2015) with additional NV centers measured by Ulm and Harvard groups on a nominally-identical sample. **(B)** Measurement of T_1^ρ using spin lock sequence using an NV center with depth 8.3 ± 1.1 nm. Here an initial $\pi/2$ pulse creates a coherent superposition of the $m_s = 0$ and $m_s = 1$ NV sublevels and a continuous microwave spin lock pulse, with an orthogonal phase, is applied. Subsequently, a second $\pi/2$ pulse converts the signal into a measurable population difference. Here, the spin lock frequency (6 MHz) is held constant while the duration of the spin lock pulse is swept. An exponential fit allows us to extract a $1/T_1^\rho$ rate of 887 ± 136 s^{-1}. **Inset**, Measurements of XY8-32, XY8-64 and XY8-128 decoherence rates for this NV center (blue points) and fit to $\sim k^{2/3}$ function. The measured value of $1/T_1^\rho$ is indicated by dashed black line.

The sensitivity can be further improved through several proposed routes. Employing Hartmann-Hahn double resonance (HHDR), the NMR sequence acquisition time can be increased from T_2 to T_1^ρ, the longitudinal relaxation time in the rotating

frame [39]. As shown in Fig. A.2B, we measure coherent spin locking times T_1^ρ up to ∼1 ms, more than a factor of 10 longer than T_2 with ∼100 π-pulses, which could translate to almost two orders of magnitude of additional increase in sensitivity. Furthermore, HHDR allows nuclear spins to be hyperpolarized, as demonstrated in [39]. This scheme yields a sensitivity figure-of-merit that is linearly, rather than quadratically, dependent on the nuclear magnetic moment [22], yielding a 10-fold improvement in detection sensitivity when the nuclear spin relaxation time T_1^n is longer than the signal acquisition time. If background protons can be removed from the diamond by deuterating the surface [27], ^{1}H spins can be used for indirect detection of nuclei with low magnetic moments [54]. In the specific case ^{2}H or ^{13}C sensing demonstrated here, this proton-assisted scheme would yield a 16-fold increase in sensitivity.

A.7 Characterization of Protein Attachment

A.7.1 Surface Topography Characterization using AFM

An Asylum MFP-3D Atomic Force Microscope (AFM) is used to characterize the surface topography of our diamond samples. We operate the AFM in tapping mode using Olympus AC240TS probes (tip radius 9 ± 2 nm, resonance frequency ∼70 kHz). The samples are mounted onto glass microscope slides using nonconductive double-sided adhesive discs. The microscope is calibrated using a 1.5 nm SiC step calibration sample (Ted Pella 629-90AFM).

After attaching ubiquitin proteins to the diamond surface, we characterize the resultant topographic features in AFM (Fig. 2.2C) by fitting a Gaussian surface to

each feature. We define the height and radius of each feature (Fig. 2.2D) as the maximum and the half-width, half-maximum of the Gaussian surface, respectively. The zero of height corresponds to the diamond surface and was determined by fitting several well-resolved features in the four corners of the image where the baseline offset was left as a free parameter. To determine which features to include in the histograms, we smooth the raw image with a Gaussian filter with standard deviation of 1 pixel and define the peaks as all pixels with a higher value than its eight immediate neighbors. Features with height lower than the diamond surface, likely corresponding to spurious noise peaks, as well as edge features are neglected. Using four large (1 x 1 μm) AFM scans, corresponding to three different diamond samples and three instances of the chemical attachment procedure, we extract a mean spacing of 25.8 $\pm$ 0.4 nm for the observed topographic features.

Assuming a randomly distributed ensemble of proteins (an assumption validated by experiments described below), we expect a fraction to be unresolved due to the resolution limit imposed by the size of the AFM probe. Thus the mean spacing of observed spots, as extracted using the method described above, underestimates the number of proteins on the surface. Accounting for this effect, we extract a corrected mean protein spacing of 21.6 $\pm$ 0.4 nm.

The proteins can be removed from the diamond surface by repeating the cleaning procedure outlined in Section A.3, as shown in Fig. A.3.

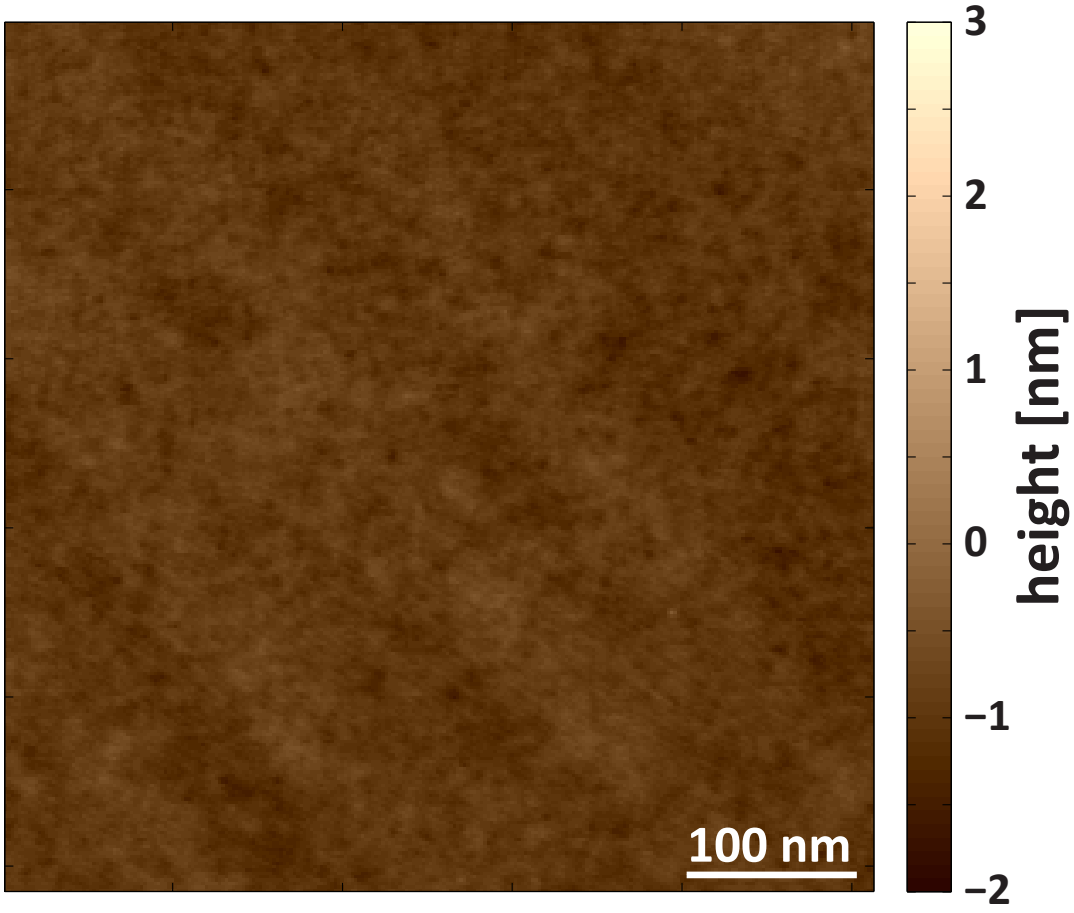

Figure A.3: **AFM characterization of clean diamond surface.** AFM height image of clean diamond surface acquired using a AC240TS probe. The diamond was cleaned using procedure described in Section A.3.

A.7.2 Protein Density Calibration using Cy3 Fluorophores

In order to independently calibrate the surface density of attached proteins, we conjugate Cy3 dye molecules to ubiquitin proteins using a commercial conjugation kit (Abcam ab188287) and attach the resulting complex to the diamond surface using the chemistry procedure described in Section A.1. The fluorophores are imaged using the confocal microscope setup described in Section A.4. Here, we use a 2 μW, 532

nm laser for excitation and detect the dye fluorescence using a 532 notch and a 633 shortpass filter. As shown in Fig. A.4A, the surface yields uniform fluorescence and the dye can be readily photobleached using continuous laser excitation (Fig. A.4B), where we observe the expected stretched exponential decay resulting from the range of photobleaching timescales of fluorophores located in different points within the Gaussian point spread function. The optical fluorescence spectrum of the surface (Fig. A.4C) shows the characteristic double-peaked structure of the Cy3 dye spectrum with a maximum at ∼570 nm.

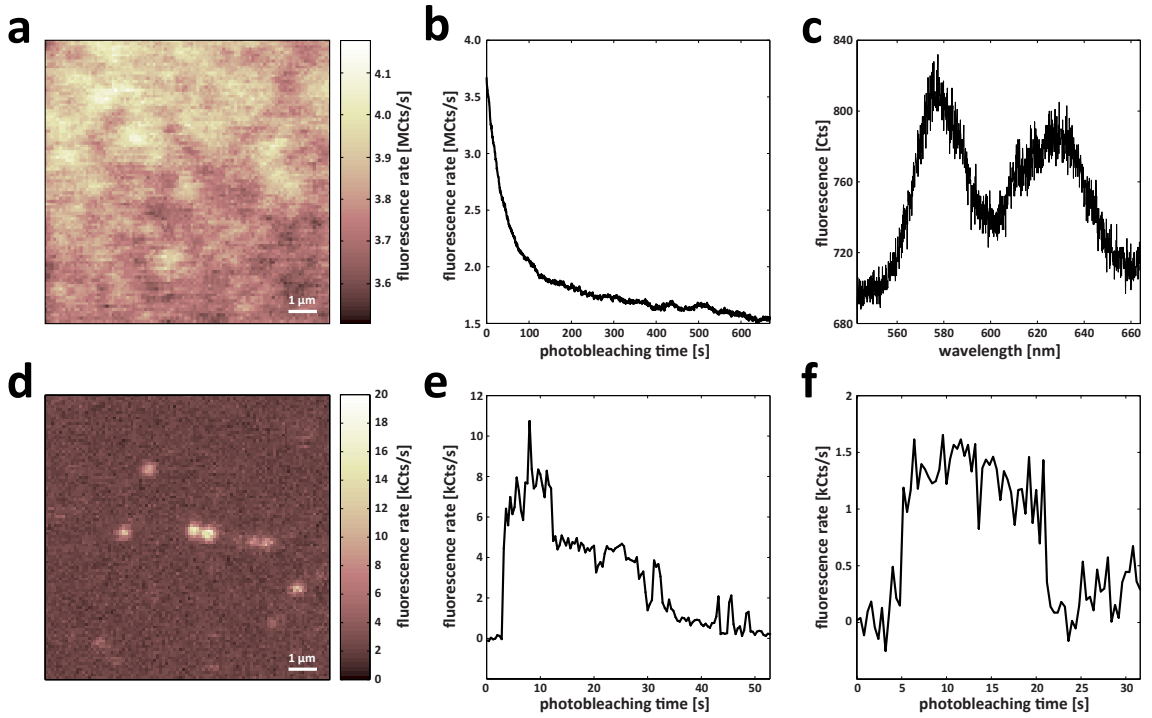

Figure A.4: **Protein density calibration using fluorophores.** **(A)** High concentration of Cy3+ubiquitin on diamond surface. **(B)** Photobleaching timetrace of high density Cy3+ubiquitin on diamond surface. **(C)** Fluorescence spectrum of high density Cy3+ubiquitin on diamond surface **(D)** Low concentration of Cy3+ubiquitin on diamond surface. **(E)** Photobleaching timetrace of a resolved Cy3+ubiquitin spot. **(F)** Bare Cy3 dye (no ubiquitin attached) photobleaching step.

We extract the surface protein density in two independent ways. First, we dilute

our Cy3+ubiquitin solution so that the resulting surface coverage yields well-resolved spots (Fig. A.4D) and find that the spots fluoresce significantly more below 633 nm than above this wavelength, consistent with the Cy3 spectrum measured at high concentration. Fig. A.4E shows a representative photobleaching timetrace of an individual spot. We image a large number of resolved spots and fit each one with a Gaussian surface function, extracting a mean fluorescence amplitude of 9.3 $\pm$ 1.1 kCts/s. Here, we acquire three consecutive images of the diamond surface. Only spots that appear in all three images and those that yield fits with amplitudes higher than one standard deviation above the background fluorescence level are chosen for analysis. The maximum fluorescence level of each spot is extracted from an average of the three images.

Assuming that the observed spots are individual Cy3+ubiquitin complexes, the mean fluorescence at low concentration allows us to extract a mean protein spacing at high concentration of 20.9 $\pm$ 1.4 nm, consistent with that measured in AFM. Here the error bar corresponds to the uncertainties in the mean fluorescence rate of individual Cy3+ubiquitin complexes as well as the mean surface fluorescence rate of Cy3+ubiquitin at high concentration (Fig. A.4A).

As an independent verification, we attach to the diamond surface a dilute concentration of bare Cy3 dye molecules and observe their characteristic photobleaching behavior (Fig. A.4F). From measurements of many such timetraces we extract a mean fluorescence rate of 1.5 $\pm$ 0.2 kCts/s. The performed conjugation chemistry described above is expected to attach a dye molecule to every exposed amine group with high probability. Assuming that all seven of the exposed Lysine residues in ubiquitin, as

well as its N-terminus are conjugated with Cy3, we extract a mean protein spacing at high concentration of 23.8 ± 1.6 nm, again consistent with that measured in AFM. Here the error bar corresponds to the uncertainties in the mean fluorescence rate of individual Cy3 dye molecules as well as the mean surface fluorescence rate of Cy3+ubiquitin at high concentration (Fig. A.4A).

A.8 NMR of ubiquitin proteins

A.8.1 Protein Samples

Ubiquitin proteins (human, recombinant) labelled with ^{2}H and ^{13}C were purchased from Giotto Biotech (G03UBQ01). Ubiquitin proteins labelled with ^{13}C were purchased from Medical Isotopes, Inc (C3225). Unlabelled Ubiquitin was purchased from Sigma-Aldrich (709417). The reagents 1-ethyl-3-(-3-dimethylaminopropyl) carbodiimide hydrochloride (EDC), N-hydroxysuccinimide (NHS) and ethylenediamine were purchased from Sigma-Aldrich (E6383, 130672 and E26266, respectively).

A.8.2 NV-based ^{2}H and ^{13}C NMR of ubiquitin proteins

Fig. A.5 shows ^{2}H and ^{13}C NMR spectra of ubiquitin proteins, enriched with deuterium and carbon-13, as measured on three NV centers (NV A, NV B and NV C, with corresponding depths of 2.9 ± 0.2 nm, 3.8 ± 0.1 nm and 3.8 ± 0.2 nm, respectively).

Fig. A.6 (panels A,C and E) shows ^{13}C NMR spectra of ubiquitin proteins, enriched only with carbon-13, as measured on three NV centers (NV D, NV E and

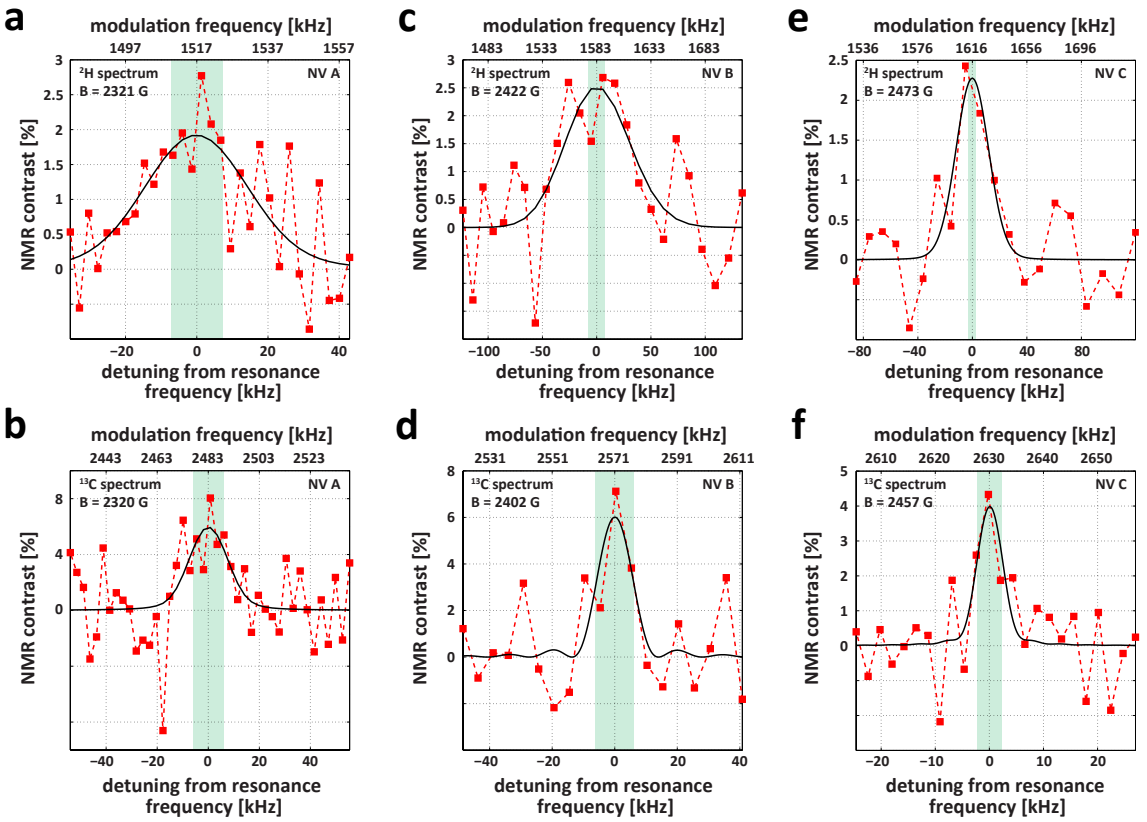

Figure A.5: **^{2}H and ^{13}C NMR of deuterated ubiquitin proteins. (A,C,E)** ^{2}H NMR spectra of deuterated ubiquitin performed on three NV centers. **(B,D,F)**, ^{13}C NMR spectra of deuterated ubiquitin performed on the same three NV centers. All spectra are fit with gaussian functions, convolved with the detector filter function. The filter function is determined by the spectral resolution, shown by green shaded regions.

NV F with corresponding depths of 3.8 ± 0.4 nm, 6.5 ± 0.6 nm and 3.6 ± 0.5 nm, respectively). Panels B, D and F show the NMR spectra (in the ^{13}C spectral range) measured on the same three NV centers after the proteins have been removed from the surface. The lineshapes for both the ^{2}H and ^{13}C NMR spectra are approximated by gaussian functions and convolved with the detector filter function. The shaded green regions denote the spectral resolution.

Fig. A.7 shows several examples of NMR spectra measured on NV centers where

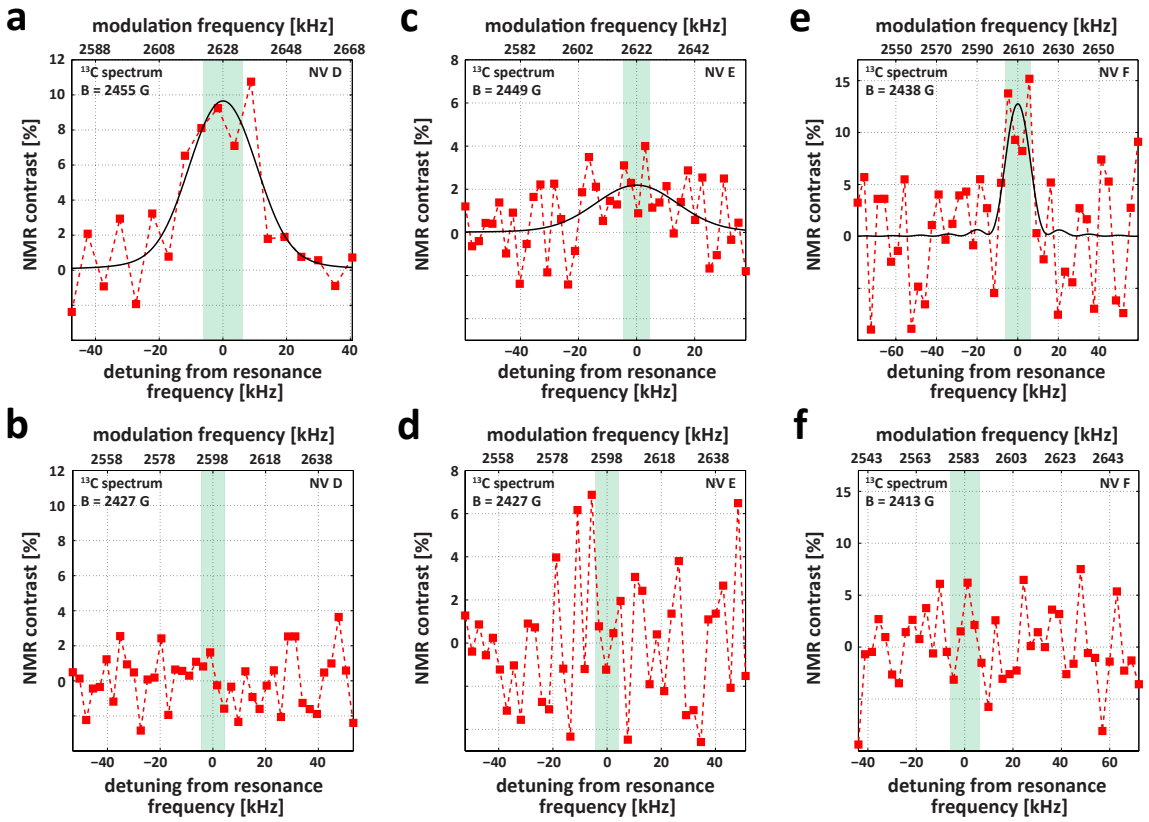

Figure A.6: **^{13}C NMR of non-deuterated ubiquitin proteins.** **(A,C,E)**, ^{13}C NMR spectra of non-deuterated ubiquitin performed on three NV centers. **(B,D,F)**, ^{13}C NMR spectra of the same three NV centers after proteins have been removed. All spectra are fit with gaussian functions, convolved with the detector filter function. The filter function is determined by the spectral resolution, shown by green shaded regions.

no proximal protein was detected. Panels A, C and E show ^{2}H NMR spectra measured on three NV centers (with depths of 4.7 $\pm$ 0.3 nm, 4.8 $\pm$ 0.4 nm and 4.1 $\pm$ 0.2 nm, respectively) after attaching deuterated ubiquitin proteins to the diamond surface. Here, twenty NV centers were studied in total. Panels B, D and F show ^{13}C NMR spectra measured on three NV centers (with depths of 4.2 $\pm$ 0.1 nm, 4.7 $\pm$ 0.3 nm and 3.7 $\pm$ 1.1 nm, respectively) after attaching non-deuterated ubiquitin proteins to the diamond surface. Here, ten NV centers were studied in total. The shaded green

regions denote the spectral resolution.

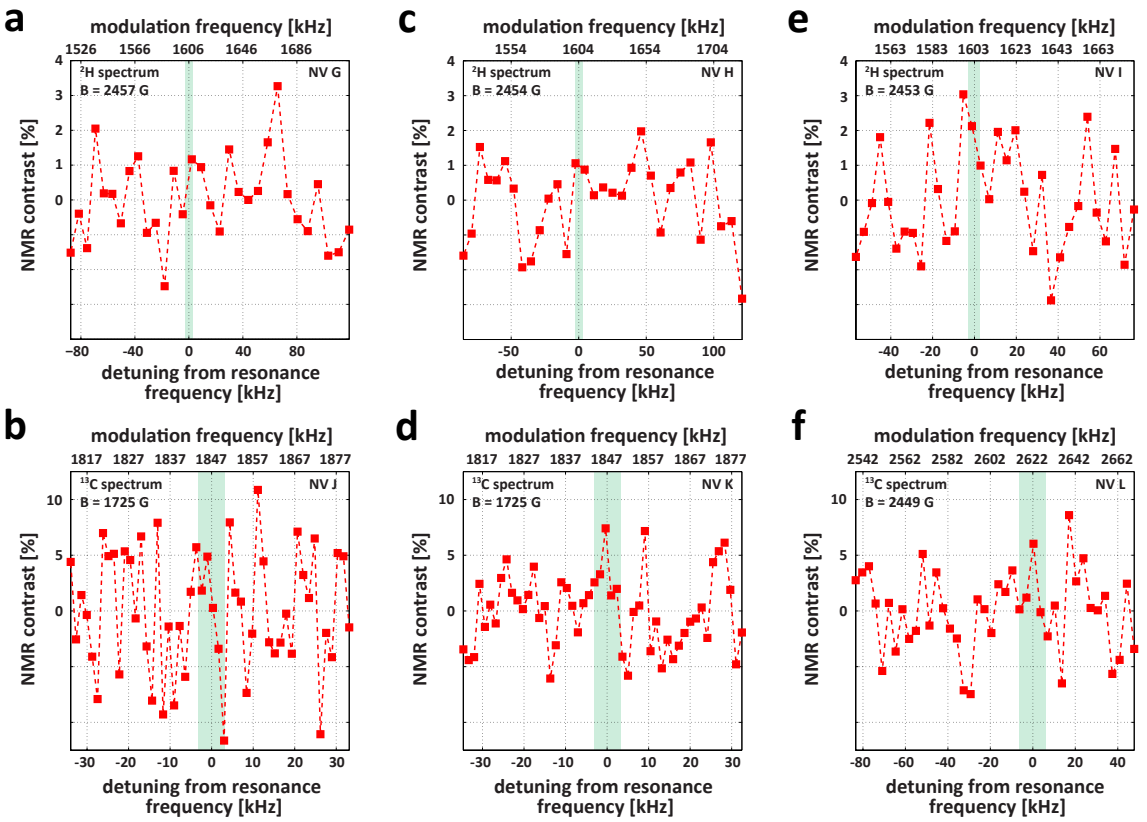

Figure A.7: **^{2}H and ^{13}C NMR spectra measured on NV centers with no proximal proteins.** **(A,C,E)**, ^{2}H NMR spectra measured on several NV centers after attachment of deuterated ubiquitin. **(B,D,F)**, ^{13}C NMR spectra measured on several NV centers after attachment of non-deuterated ubiquitin.

The magnetic field for each measurement is indicated. The microwave frequency can be determined by multiplying the magnetic field by the appropriate gyromagnetic ratio (1070.5 Hz/G for ^{13}C and 653.6 Hz/G for ^{2}H). All spectra presented here were acquired using integration times of approximately one to three days.

A.8.3 Characterization of Ubiquitin Proteins Using Conventional NMR

We verify the deuteration of the proteins by comparing the ^{1}H NMR spectrum of ^{2}H-labeled ubiquitin proteins to that of the unlabelled protein (Figs. A.8A and A.8B). Here the samples are suspended at 2 mg/ml in 90% H_20, 10% D_20. We use an Agilent DD2 600 MHz spectrometer and implement a Double Pulsed Field Gradient Spin Echo (DPFGSE) pulse sequence to suppress the background solvent signal. The deuterated-Ubiquitin spectrum is dominated by the NMR-active amide-protons in the protein backbone while the vast majority of deuterons are not solvent-accessible and therefore do not contribute to the ^{1}H spectrum.

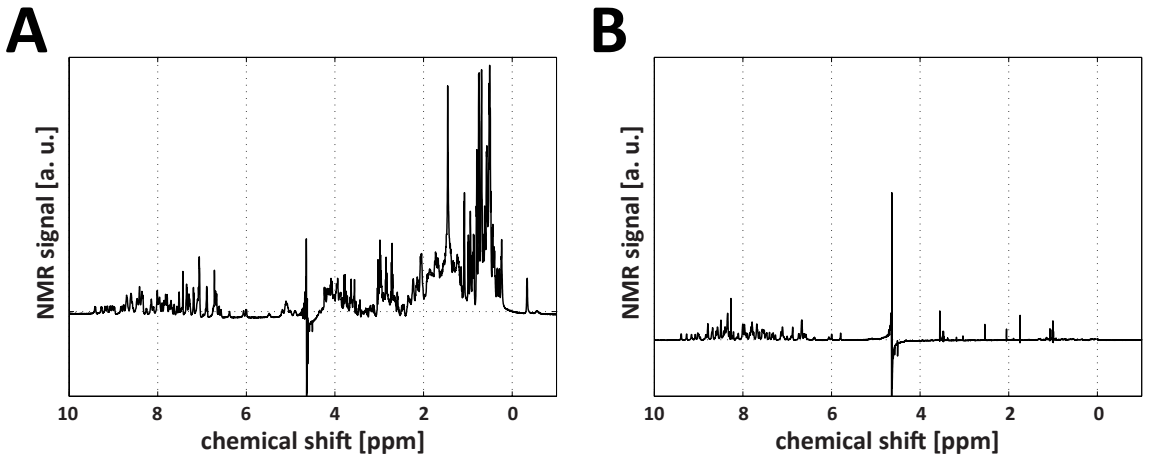

Figure A.8: **Conventional NMR spectra of ubiquitin. (A)**, Liquid-state ^{1}H NMR spectrum of unlabelled ubiquitin. Here the Double Pulse Field Gradient Spin Echo (DPFGSE) pulse sequence was used for solvent suppression. **(B)**, Analogous ^{1}H NMR spectrum of deuterated ubiquitin.

A.9 The Spurious 2/13 Harmonic of ^{1}H

As shown in [107], the spurious 2/13 harmonic of ^{1}H (which is within 0.3% of the ^{2}H Larmor frequency) can be present in XY8-k NMR spectra when coherent evolution during the π-pulses cannot be neglected. In order to rule out the presence of this harmonic, we apply an external calibration signal at frequency 10.312 MHz (simulating a large ^{1}H NMR signal) and measure the NMR spectrum in the vicinity of the 2/13 harmonic (1.587 MHz). We observe that in addition to the 2/13 harmonic, the simulated signal produces additional 4/25 and 4/27 harmonics with amplitude larger than the 2/13 harmonic (Fig. A.9). Due to the absence of these additional harmonics in our ^{2}H NMR spectra, we rule out that the observed deuterium signals arise from background hydrogen. We additionally note that the observed deuterium linewidths are a factor of $\sim$10 larger than that measured on the spurious hydrogen harmonic, providing additional verification that our signals cannot be attributed to background hydrogen.

A.10 NV-based Quadrupolar Spectroscopy of Individual Molecules

A.10.1 Physical Principles of Single Molecule Quadrupolar Spectroscopy

In this section, we outline the method for determining the structure of a molecule using quadrupolar spectroscopy. As is well-known from conventional Nuclear Quadrupole

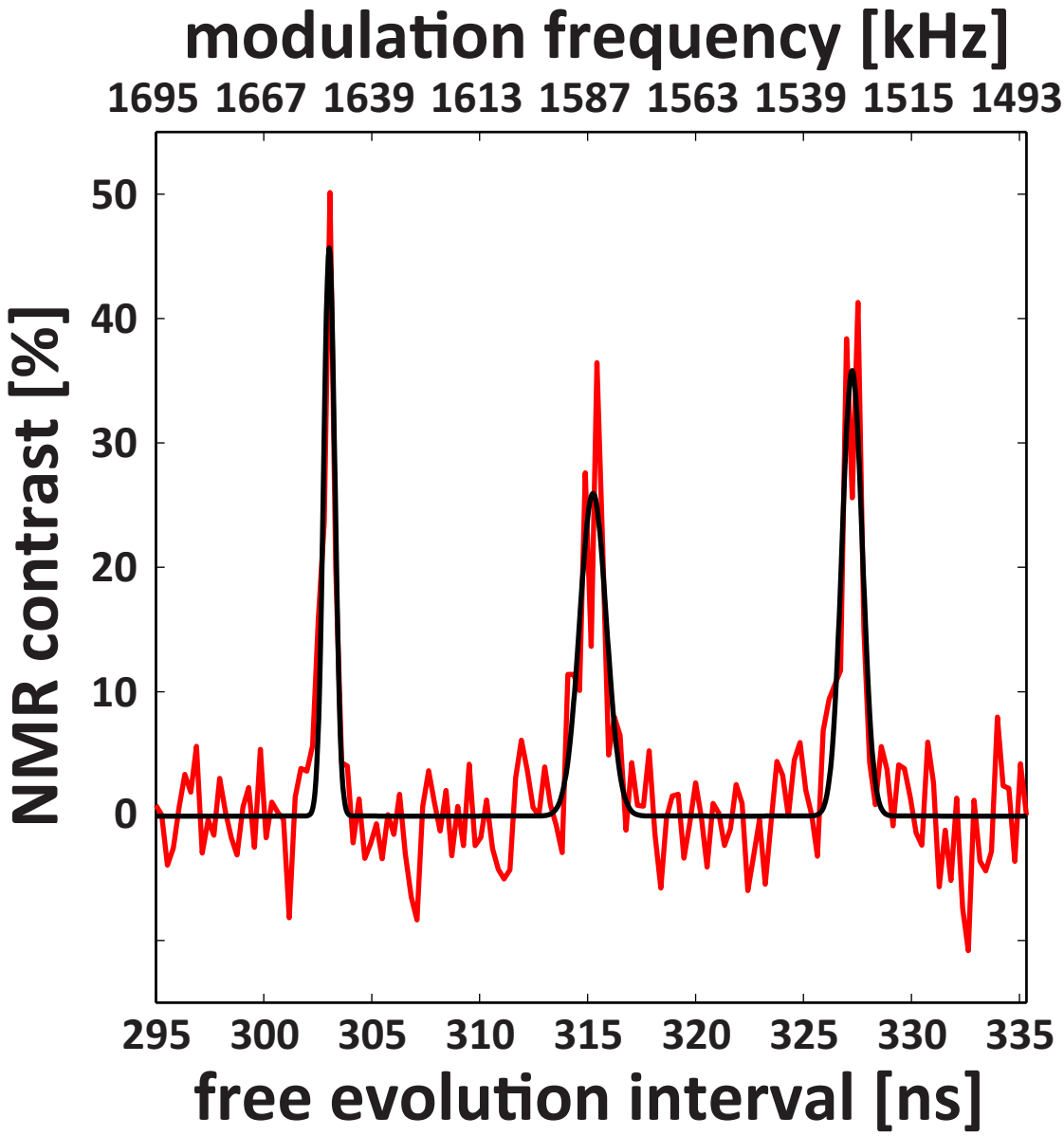

Figure A.9: **The spurious harmonics of hydrogen.** Measurement of spurious 4/25, 2/13 and 4/27 harmonics of XY8-k measured using external calibration signal at frequency 10.312 MHz.

Resonance (NQR) [50], a nuclear spin with $I > 1/2$ possesses an electric quadrupole moment Q. In the absence of a magnetic field, the Hamiltonian of such a spin with

$I = 1$ (e.g. ^{2}H or ^{14}N) is given by

$$H_q = \frac{e^2qQ}{4}\left[3S_{z'}^2 + \eta\left(S_{x'}^2 - S_{y'}^2\right)\right] \tag{A.26}$$

where e is the electric charge quantum, S_μ are spin vector operators in direction $\vec{\mu}$, and the parameters q and η are determined by the local electric field gradient (EFG) at the position of the nucleus in its principal coordinate system $\{\vec{x'}, \vec{y'}, \vec{z'}\}$ [108]. The quantities e^2qQ and η are conventionally known as the quadrupole coupling constant (QCC) and the asymmetry parameter (AP), respectively and are typically determined experimentally for each compound of interest. Defining $\bar{Q} = e^2qQ$, the eigenvalues of this Hamiltonian can be computed and are given by

$$E_0 = -\frac{1}{2}\bar{Q}, E_{\pm 1} = \frac{(1 \pm \eta)}{4}\bar{Q}, \tag{A.27}$$

up to a constant shift, with corresponding eigenstates $|m_s = 0\rangle, |\pm\rangle = (|m_s = 1\rangle \pm |m_s = -1\rangle)/\sqrt{2}$. In general, all three transitions between any two of these eigenstates have a non-zero matrix element for a spin vector operator, thereby creating magnetic field noise at the frequencies

$$\nu_\pm = \tfrac{3\pm\eta}{4}\bar{Q}, \tag{A.28}$$

$$\nu_0 = \tfrac{\eta}{2}\bar{Q}, \tag{A.29}$$

thus allowing both $\bar{Q}$ and η to be extracted for the zero-field spectrum.

When an external magnetic field is applied, the Zeeman coupling $H_z = -g\mu_B\vec{S}\cdot\vec{B}$ modifies the eigenvalues of the spin states, leading to a change in the magnetic field noise spectrum. We note that this modification is strongly dependent on the orientation of the external magnetic field with respect to the spin axes defined by

$\vec{x'}, \vec{y'}$ and $\vec{z'}$. Therefore, by measuring the noise spectrum at various magnetic fields, one can infer the orientation of the spin relative to the external magnetic field. As an example, in the limit of small magnetic field $B \ll \eta\bar{Q}/\mu_B g$, the second order correction to the spectral peak positions are given by:

$$\Delta\nu_+ = \frac{4(\mu_B g)^2}{\bar{Q}}\left(\frac{B_{z'}^2}{2\eta} + \frac{2B_{x'}^2}{3+\eta} + \frac{B_{y'}^2}{3-\eta}\right) \tag{A.30}$$

$$\Delta\nu_- = \frac{4(\mu_B g)^2}{\bar{Q}}\left(\frac{-B_{z'}^2}{2\eta} + \frac{B_{x'}^2}{3+\eta} + \frac{2B_{y'}^2}{3-\eta}\right) \tag{A.31}$$

$$\Delta\nu_0 = \Delta\nu_+ - \Delta\nu_-, \tag{A.32}$$

from which one can obtain the value of $\sin^2\theta(3-\eta\cos(2\phi))$, where θ and ϕ are polar and azimuthal angles of $\vec{B}$ in the principal coordinate system. Complete information of the orientation can be obtained by varying the orientation of the external magnetic field.

In contrast to conventional NMR spectroscopy with crystallized samples, the position of each spin can also be identified. When the detector is itself a nanoscale object located in close proximity to the target molecule, the amplitude of each spectral line depends sensitively on the position of the corresponding nuclear spin relative to the detector. This spatial dependence arises from the radial and angular dependence of the magnetic dipole interaction of each nuclear spin with the nanoscale probe. This effect is illustrated in Fig. A.10A and A.10B, where the magnetic noise spectrum of a single spin is computed for different positions (S1 and S2) and orientations (S2 and S3). In general, for given values of the QCC and AP, the 1-dimensional quadrupolar spectrum is a function of $\vec{r}$, $\vec{B}$ and principal coordinates $\hat{x}', \hat{y}', \hat{z}'$. Therefore, measurement of the spectrum in several external magnetic field (amplitudes and orientations) yields information about the molecular structure (Fig A.10C). This extraction of spa-

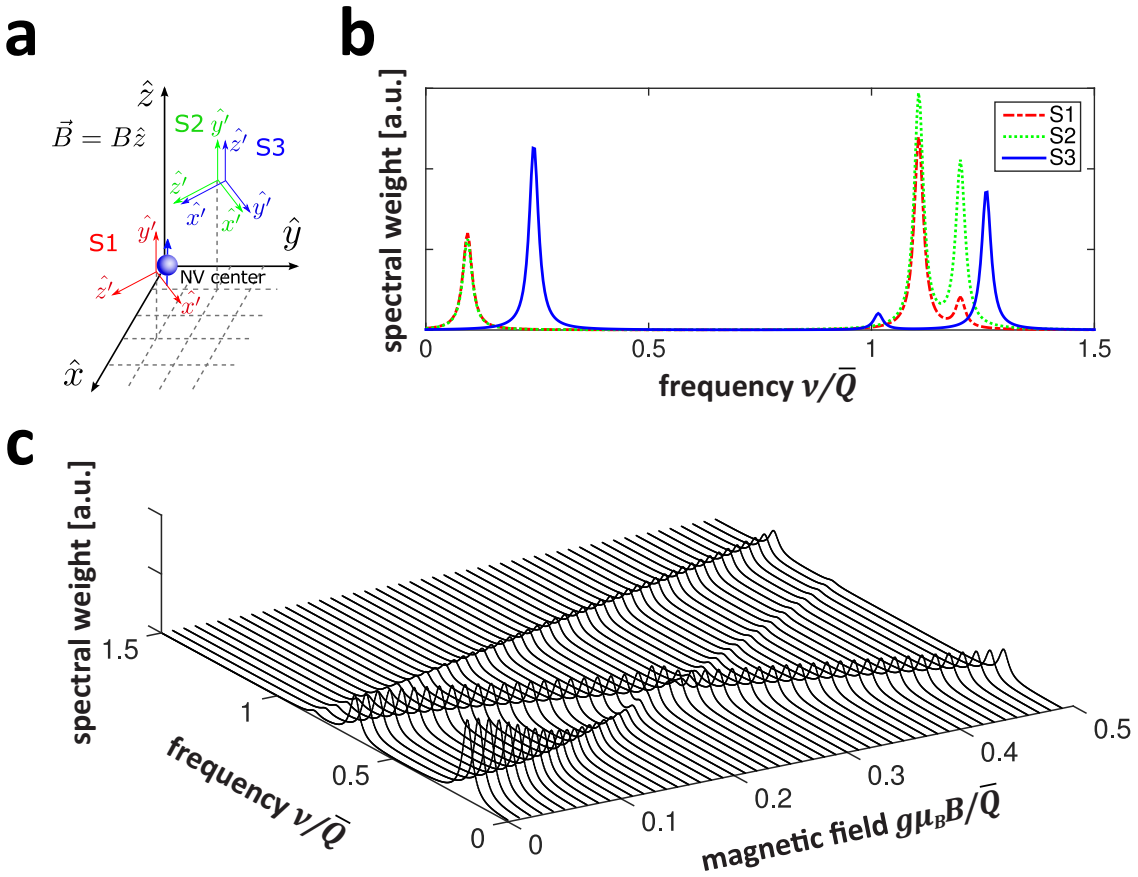

Figure A.10: **Principles of quadrupolar spectroscopy with NV centers. (A)**, Various positions and orientations for spins with quadrupolar moments. The axes with $\hat{x}', \hat{y}', \hat{z}'$ denotes the principal axes for each spin's quadrupolar interaction. **(B)**, Three spectral peaks appear for each spin-1. While the resonance frequencies are determined by the orientation of the principal coordinate system relative to the external magnetic field B (here chosen such that $g\mu_B B = 0.5\bar{Q}$), the weights of the resonances depend on the positions of the spins (S1 and S2). A different orientation at the same position gives a distinct set of spectral peaks (S2 and S3). We assume a value of $\eta = 0.35$ for these simulations. **(C)**, Magnetic field dependence of the three spectral lines shown in **(B)**, blue curve.

tial coordinates of target spins based on magnetic-field dependent spectra is similar to the procedure used in [52], where the positions of several electronic spins were extracted based on their orientation-dependent interaction with a proximal NV center.

A typical biomolecule (e.g. amino acid, protein) may contain many inequivalent quadrupolar nuclei, each with a different principal coordinate system and each pos-

sessing its own characteristic QCC and AP. In a high-field bulk spectrum, containing a macroscopic number of randomly-oriented molecules, these orientation dependent shifts yield a characteristic Pake doublet spectrum [49] for each equivalent (possessing the same QCC and AP) nuclear spin (see Fig. 2.4B, bottom panels). In the limit when only a single molecule contributes to the observed spectrum, however, the Pake doublets break up into potentially resolvable lines, with each nuclear spin contributing three spectral lines. Therefore, the problem of determining the structure of a molecule, assuming that it is fully determined by the positions of the quadrupolar nuclei (as in ^{2}H spectra of deuterated proteins), effectively reduces to finding sets of three spectral peaks corresponding to each nuclear spin and identifying its position and orientation. We note that this task is essentially equivalent to a pattern matching problem since each spin-1 with a given QCC, AP, position and orientation has a well-defined dependence on the external magnetic field (as shown in Fig. A.10C and Fig. 2.4C). We also emphasize that the computational cost of this task is greatly reduced in case there are known constrains on the structure of a molecule (e.g. the sequence of amino acid in a protein). The details of this technique will be described in a forthcoming publication.

A.10.2 Simulations of Quadrupolar Spectra

We illustrate the physics of quadrupolar spectroscopy by considering the model system deuterated Phenylalanine, one of the essential amino acids that make up proteins.

In order to simulate the ^{2}H quadrupolar spectrum, we model Phenylalanine as

an interacting system of deuterons in the C-D, C-D_2 and aromatic groups of the amino acid. We neglect deuterons in the amine and carboxylic groups, which readily exchange with hydrogen in the environment. We assume typical [49, 109] QCC values of 120 kHz, 110 kHz and 130 kHz for deuterons in the C-D, C-D_2 and aromatic groups, respectively. The effects of APs, which tend to be very small for systems of this type (on the order of $\sim$0.05), are neglected [110]. We assume the quadrupolar axis to be oriented along the C-D bond in all cases. In order to simulate the ^{14}N spectrum, we use the known values of $\bar{Q} = 1.354$ MHz and $\eta = 0.63$ [111]. In our simulations the amino acid is fixed on the diamond surface in one of three configurations (Fig. 2.4B - top three panels) and an NV center 4 nm below the (100)-oriented surface is used to probe the variance of the magnetic field fluctuations along its axis. We simulate applying an XY8-1299 sequence, resulting in a mean spectral resolution of $\sim$5 kHz, corresponding to a T_2 of 200 μs. Because of the large quadrupole moment of ^{14}N, the spectral resolution is variable if the number of π-pulses is kept constant during spectrum acquisition. Consequently, if the optimal spectral resolution is to be used in all parts of the spectrum, the number of π-pulses would need to be adjusted dynamically. In our simulations we assume a constant spectral resolution of $\sim$5 kHz. We assume an additional 4 kHz broadening arising from the dipolar coupling of each ^{14}N to its nearest ^{1}H spin.

The change in orientation or conformation of an individual Phenylalanine amino acid, measured by monitoring the amplitude of a single resonance in Fig. 2.4B, can be detected in approximately $\sim$3 seconds using the techniques outlined in Section A.6.2. For this estimate, we assume that the target molecule can deterministically be placed

above a 3 nm deep NV center and that the coherence time can be improved by a factor of ∼3 beyond what was demonstrated in this work.

	depth [nm]	$1/T_2$ [kHz]	depth [nm]	$1/T_2$ [kHz]
NV 1	5.3 ± 0.1	53.1 ± 4.6	3.1 ± 0.1	13.0 ± 1.1
NV 2	6.5 ± 0.1	49.9 ± 1.5	5.1 ± 0.2	9.9 ± 1.1
NV 3	5.1 ± 0.1	67.4 ± 0.7	4.8 ± 0.2	5.9 ± 0.4
NV 4	5.0 ± 0.1	97.6 ± 2.8	4.0 ± 0.1	6.9 ± 0.8
NV 5	5.6 ± 0.1	59.2 ± 1.9	5.3 ± 0.1	4.8 ± 0.4
NV 6	5.1 ± 0.1	64.8 ± 1.0	4.9 ± 0.1	7.9 ± 1.1
NV 7	7.3 ± 0.1	33.0 ± 4.8	6.2 ± 0.3	5.0 ± 0.6

Table A.1: Experimental measurements of NV depth and XY8-187 decoherence rates $1/T_2$ for several NV centers before (columns 1 and 2) and after (columns 3 and 4) oxygen anneal. Errors indicate 68% confidence intervals.

Appendix B

Supporting material for Chapter 3

B.1 Theoretical Model of NQR Spectrum

Here we use the model developed in Section A.6. Diagonalization of the nuclear Hamiltonian

$$H_Q = \frac{\overline{Q}}{4I(2I-1)}\Big[3I_z^2 - I^2 + \eta(I_x^2 - I_y^2)\Big] + \hbar\gamma_n \mathbf{I}\cdot\mathbf{B}, \tag{B.1}$$

where $\mathbf{B}$ is the external applied magnetic field, yields a set of energy eigenvalues and eigenstates which can be used to evaluate the correlation functions in Eqs. A.13 and A.14. The quantity η, is known as the asymmetry parameter and is related to the degree of deviation from axial symmetry in a material (for the case of h-BN, $\eta = 0$) [112]. In the absence of an applied magnetic field the eigenstates of H_Q define a principal axis coordinate system. In axially symmetric materials, this coordinate system is parametrized by a single axis.

In the preceding analysis, we have implicitly assumed that the nuclear spins are non-interacting. In order to (approximately) capture the effects of interactions we

replace the delta-function resonances in the magnetic spectral density with Gaussian functions of width γ:

$$\delta\big(\Delta\omega_{n,m} - \omega\big) \rightarrow \frac{1}{\sqrt{2\pi\gamma^2}} \exp\left[\frac{-(\omega - \Delta\omega_{n,m})^2}{2\gamma^2}\right]. \tag{B.2}$$

All NQR spectra presented in this work are evaluated using this model. After normalization (see Section A.6.1), the data are fit using the expression in Eq. A.5, where the fit parameters correspond to the depth of the NV sensor d, the applied external magnetic field, the quadrupole coupling constant of the target nuclear spins and the spectral linewidth γ.

B.2 NMR Sensing Area and Volume

For a two-dimensional distribution of nuclear spins on the diamond surface, the amplitude of the magnetic field variance signal depends on the depth d of the proximal NV sensor. In the limit when d is much larger than the typical distance between the target nuclear spins (so that the sample can be considered a continuous spin density) approximately 75% of the NQR signal comes from within a circular region of area πd^2 on the diamond surface, directly above the NV center. In this work, we define this region to be the sensing area.

For a three-dimensional spin density, a similar analysis shows that approximately 50% of the signal comes from a half-sphere of volume $\frac{2}{3}\pi d^3$ on the diamond surface, directly above the NV center. We define this region to be the sensing volume.

B.3 Number of Detectable Spins

The optimal sensitivity yields the minimum number of detectable spins per unit averaging time

$$N_{min} \approx \frac{16\pi^4 d^6}{(\mu_0 \hbar \gamma_e \gamma_n)^2 \mathcal{F}} \frac{\sqrt{T_2 + T_R}}{T_2^2}, \tag{B.3}$$

where we assume that the spins are situated on the diamond surface immediately above the NV sensor [66]. Here T_R corresponds to the readout time and $\mathcal{F}$ is the readout fidelity (see SI). Taking a typical readout fidelity of 0.03, a separation of 4 nm between NV and h-BN flake and the measured corresponding NV coherence time ($\sim 150\mu s$), we estimate that a single ^{11}B nuclear spin can be detected in approximately one minute of integration time.

It has been demonstrated [51] that with the use of spin-to-charge conversion readout, $\mathcal{F}$ can be dramatically increased at the cost of a modest increase in T_R. Using this technique, we estimate that our sensitivity can be improved to allow detection of an individual ^{11}B spin, placed directly above the NV sensor, after one second of integration time. In this estimate we again assume a coherence time of 150 μs and an NV depth of 4 nm. The readout fidelity $\mathcal{F} = 0.2$ and the readout time of 100 μs were taken from experimental data presented in [51].

B.4 Model of Dipolar Interactions

Our model for simulating the nuclear spin linewidths, as presented in Fig. 3.3E, assumes that the spins within the h-BN crystal (^{11}B, ^{10}B and ^{14}N) interact only via dipole-dipole coupling. We first consider the case of two nuclear spins. We first

consider the simple case in which the NV sensor is used to probe a single nuclear spin (henceforth denoted by subscript 1) while it is being subjected to the magnetic field corresponding to fluctuations of a nearby nuclear spin (denoted by subscript 2). These magnetic fluctuations increase the linewidth of the spin being probed, where the linewidth is given by the root-mean-square (RMS) lineshift and corresponds to the expression

$$\Delta\nu = \sqrt{\langle\delta^2_{m_1 n_1}\rangle} = \sqrt{Tr(\rho_2 \delta^2_{m_1 n_1})}, \tag{B.4}$$

where ρ_2 is the density operator corresponding corresponding to the spin that creates the magnetic fluctuations and $\delta^2_{m_1 n_1}$ is the lineshift variance, given by the expression

$$\delta^2_{m_1 n_1} = \Big[\langle m_1 | H_{int} | m_1 \rangle - \langle n_1 | H_{int} | n_1 \rangle \Big]^2 / (2\pi\hbar)^2. \tag{B.5}$$

Here $|m_1\rangle$ and $|n_1\rangle$ are the spin eigenstates (determined by diagonalizing H_Q) corresponding to the transition being probed and H_{int} is the dipole-dipole interaction Hamiltonian

$$H_{int} = \frac{\mu_0 \hbar^2 \gamma_{n,1}\gamma_{n,2}}{4\pi|r|^3}\Big[3(\mathbf{I}_1\cdot\mathbf{r}_{12})(\mathbf{I}_2\cdot\mathbf{r}_{12}) - \mathbf{I}_1\cdot\mathbf{I}_2\Big] \tag{B.6}$$

$$= \frac{\mu_0 \hbar^2 \gamma_{n,1}\gamma_{n,2}}{4\pi|r|^3}\Big[I_1^x B_x + I_1^y B_y + I_1^z B_z\Big], \tag{B.7}$$

where the magnetic field operators are defined by the expressions

$$B_x = I_2^x - 3(\mathbf{r}_{12}\cdot\hat{\mathbf{x}})\Big[(\mathbf{r}_{12}\cdot\hat{\mathbf{x}})I_2^x + (\mathbf{r}_{12}\cdot\hat{\mathbf{y}})I_2^y + (\mathbf{r}_{12}\cdot\hat{\mathbf{z}})I_2^z\Big] \tag{B.8}$$

$$B_y = I_2^y - 3(\mathbf{r}_{12}\cdot\hat{\mathbf{y}})\Big[(\mathbf{r}_{12}\cdot\hat{\mathbf{x}})I_2^x + (\mathbf{r}_{12}\cdot\hat{\mathbf{y}})I_2^y + (\mathbf{r}_{12}\cdot\hat{\mathbf{z}})I_2^z\Big] \tag{B.9}$$

$$B_z = I_2^z - 3(\mathbf{r}_{12}\cdot\hat{\mathbf{z}})\Big[(\mathbf{r}_{12}\cdot\hat{\mathbf{x}})I_2^x + (\mathbf{r}_{12}\cdot\hat{\mathbf{y}})I_2^y + (\mathbf{r}_{12}\cdot\hat{\mathbf{z}})I_2^z\Big]. \tag{B.10}$$

Here $\gamma_{n,1}$ and $\gamma_{n,2}$ are the gyromagnetic ratios of the nuclear spins, $\mathbf{r}_{12}$ is the separation vector between the two spins and $\hat{\mathbf{x}}$,$\hat{\mathbf{y}}$,$\hat{\mathbf{z}}$ are unit vectors corresponding to the chosen

coordinate system.

When more than two spins are included in the analysis the lineshift variances corresponding to each spin can be added independently, resulting in the total linewidth

$$\Delta\nu = \sqrt{\sum_i Tr(\rho_i \delta^2_{m_1 n_1})}. \tag{B.11}$$

All measurements presented in this work are performed at room temperature, where the spin eigenstates can be assumed to be equally populated. Consequently, the density operator of all spins corresponds to a fully unpolarized mixture of spin eigenstates.

B.5 Sample Preparation

B.5.1 Diamond Samples

All measurements reported in this work were performed using three (henceforth referred to as samples A, B and C) [100]-cut, electronic-grade diamond crystals (Element Six). The samples consisted of a 50 μm ^{12}C-enriched (99.999% abundance, epitaxially-grown using plasma-enhanced chemical vapor deposition) layer on a natural-abundance diamond substrate. The isotopically-enriched surfaces of samples A and C were polished while sample B was left unpolished. Substitutional N and B concentrations were less than 5 and 1 ppb, respectively. Samples A, B and C were implanted (Innovion) with a $^{15}N^+$ dose of 10^9 cm^{-2}, tilt angle of 0° and ion beam energies of 3 keV, 2 keV and 3 keV, respectively.

After implantation the samples were cleaned in a boiling mixture (1:1:1) of nitric, sulfuric and perchloric acids. The diamonds were then annealed in vacuum using the

following procedure: (a) 6 hour ramp to 400°C, (b) 6 hours at 400°C, (c) 6 hour ramp to 800°C, (d) 8 hours at 800°C and (e) 6 hour ramp to room temperature. After a second 3-acid clean, the samples were annealed in a dry oxygen environment (Tystar, Mini Tytan 4600) using the following procedure: (a) ramp to 465°C for 2 hours, (b) anneal at 465°C for 4 hours, (e) ramp down to 250°C for 2 hours. The samples were cleaned in a Piranha solution (2:1 mixture of concentrated H_2SO_4 and 30% hydrogen peroxide) immediately before and after the oxygen anneal. This treatment has been shown to reduce the decoherence rates of near-surface NV centers [66].

B.5.2 Hexagonal Boron Nitride Samples

Hexagonal boron nitride flakes were produced by mechanical exfoliation of single crystals grown by a high-pressure and high-temperature process [113, 114]. The flakes were first exfoliated using wafer tape (Ultron Systems 1007R) onto a Si substrate with 90 nm of thermally grown SiO_2 (NOVA Wafer). This thickness of SiO_2 on Si has previously been demonstrated to maximize the optical contrast of monolayer h-BN flakes [115]. To remove tape residue from the exfoliation process, the chip was vacuum annealed for 30 minutes at 300°C in a rapid thermal annealer. Thin flakes were identified using an optical microscope and then characterized by atomic force microscopy, Raman spectroscopy, and optical measurements of second harmonic generation (see section on identifying h-BN layer thickness).

The thin flakes of h-BN were transferred from the Si/SiO_2 chip onto a diamond chip with implanted NV centers by the same dry polymer transfer process used to create van der Waals heterostructures [116, 61]. First, h-BN flakes were peeled off from

the SiO_2 surface by sequentially pressing a polymer stamp made of polycarbonate to the surface of the chip, heating to 90°C, cooling to room temperature, and peeling off the stamp. The picked-up flakes on the polymer stamp were then brought in contact with the diamond surface while heating to 160°C, causing the polymer stamp and the h-BN flakes to adhere to the diamond surface. We did not remove the polycarbonate layer using annealing, as is commonly done, since shallow NV centers are susceptible to degradation if exposed to the type of vacuum annealing commonly used by the 2D material community.

When the h-BN flakes are transferred onto the diamond surface, they become weakly fluorescent (see Fig. B.1B) and can be colocalized with shallow NV centers. The h-BN fluorescence can then be readily photobleached by applying a 532 nm laser for several seconds.

B.6 Experimental Setup

B.6.1 Optical Setup

All NMR and NQR experiments presented in this work were carried out using a home-built scanning confocal microscope (Fig. B.1A). Optical excitation of individual NV centers was performed using a 532 nm laser (Coherent, Compass 315M-100) while the NV fluorescence was detected with a fiber-coupled single-photon counting module (PerkinElmer, SPCM-AQRH-14-FC). The microscope used a Nikon Plan Fluor 100x oil immersion objective (NA = 1.3) in an inverted configuration. Lateral steering of the laser beam was accomplished using a galvanometer (Thorlabs GVS012) while the

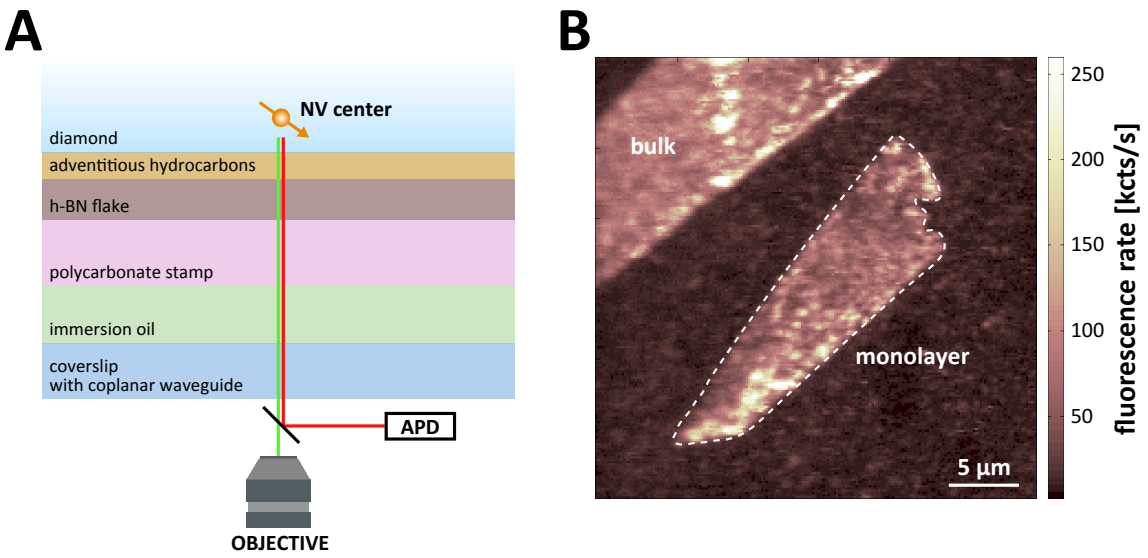

Figure B.1: **Schematic of experimental setup. (A)** Shallow NV centers are excited with a 532 nm laser while the NV fluorescence is split from the excitation beam with a beam-splitter and collected using a photodetector. The surface of the diamond contains a 1-2 nm native layer of water or hydrocarbons (see Section B.12) while the h-BN flake is protected on the backside by a thick polycarbonate layer. A layer of immersion oil is added between the glass coverslip (containing the coplanar waveguide used to drive MW fields) and the polycarbonate stamp in order to increase collection efficiency. **(B)** Fluorescence image (excitation at 532 nm, collection using 637 longpass filter) of an h-BN monolayer (indicated with dashed white outline) and a thick (greater than 50 nm) flake on the diamond surface. While the flakes are weakly fluorescent, this fluorescence can be readily photobleached by applying a 532 laser for several seconds.

vertical position was controlled with a piezoelectric stage (Physik Instrumente P-721 PIFOC). Pulses of laser light were gated using an acousto-optic modulator, which was controlled through TTL pulses delivered using a pulse generator (Spincore Technologies 500 MHz PulseBlasterESR-PRO). Additional details on this optical setup can be found in [66].

B.6.2 Microwave Setup

We apply microwave (MW) drive fields to the NV sensor using a Stanford Research Systems SG384 signal generator. Here the phase of the waveform is modulated us-

ing a built-in IQ modulator, which is triggered using a two-output Tektronix 3052C Arbitrary Function Generator (AFG). The MW pulses are gated with a Mini-Circuts switch (ZASWA-2-50DR+), which is controlled using a second Tektronix 3052C AFG. The gated signal is amplified using a Mini-Circuits ZHL-16W-43-S+ amplifier and delivered to the NV center via a home-built coplanar waveguide. Here we deposit layers of Ti (50 nm), Cu (1000 nm) and Au (300 nm) on a glass coverslip (Ted-Pella, Inc, #260320). A transmission line pattern is created using photolithography (SUSS MicroTec MJB4) where the exposed metal is removed using Au etch (Cu and Au) and dilute hydrofluoric acid (Ti). Additional details on our microwave setup can be found in [66].

B.7 Modified XY8-k Pulse Sequence

All NQR measurements presented in this work utilize a modified XY8-k pulse sequence. Here the NV electronic spin state is optically polarized [31] and prepared in a superposition of the magnetic sublevels $m_s = 0$ and $m_s = 1$. The state is then periodically flipped with k π-pulses, applied at frequency f (not to be confused with the carrier frequency of the MW field, which is close to the NV zero-field splitting of $\sim$2.87 GHz [29]). The spin evolution during the control sequence is governed by the time-dependent components of the local magnetic field (which may include contributions from proximal nuclear spins). Any accumulated phase at the end of the control sequence can be converted to a measurable population signal with a final $\pi/2$ pulse and measured via spin-dependent fluorescence under optical pumping [31].

In contrast to the more canonical XY8 sequence [27, 38, 69], in which the free

evolution intervals immediately after the initial $\pi/2$-pulse and immediately before the final $\pi/2$-pulse are half as long as those between subsequent π-pulses, the $k+2$ pulses comprising our modified sequence are separated by identical free evolution intervals. The amplitudes of the π and $\pi/2$ pulses are controlled through IQ modulation. The phases of the pulses are applied using the following pattern:

$$[X]_1[Y]_2[X]_3[Y]_4[Y]_5[X]_6[Y]_7[X]_8 \cdots [X]_{k-2}[Y]_{k-1}[X]_k, \tag{B.12}$$

where $[X]$ and $[Y]$ correspond to rotations about the x and y axis, respectively. In order to cancel the DC component of the magnetic noise spectrum, an odd number of π-pulses is required. As a specific example, an XY8-11 sequence has the form

$$[X]_{\pi/2}[X]_\pi[Y]_\pi[X]_\pi[Y]_\pi[Y]_\pi[X]_\pi[Y]_\pi[X]_\pi[X]_\pi[Y]_\pi[X]_\pi[X]_{\pi/2}, \tag{B.13}$$

where each pulse is separated by free evolution interval τ. The modulation frequency is defined as the inverse of this free evolution interval, so that $f = 1/\tau$.

B.8 NV Magnetic Sensitivity

As shown in [66], the optimal magnetic sensitivity, defined as the minimum variance signal δB^2_{min} detectable in time t, is achieved when the total sequence duration is approximately equal to the spin coherence time T_2 of the NV sensor and is given by the expression

$$\delta B^2_{min}\sqrt{t} \approx \frac{\pi^2}{\gamma_e^2 \mathcal{F}} \frac{\sqrt{T_2 + T_R}}{T_2^2}. \tag{B.14}$$

Here T_R is the readout time (which is negligible for the conventional optical readout used in this work) and $\mathcal{F} = \left[1+2(\alpha_0+\alpha_1)/(\alpha_0-\alpha_1)^2\right]^{-\frac{1}{2}}$ is the readout fidelity, where

α_0 and α_1 are the average number of photons detected, per measurement, from the $m_s = 0$ and $m_s = 1$ spin sublevels of the NV center, respectively. For typical readout fidelities of $\sim$0.03, the control sequence must be repeated many times (>1000) in order for the flourescence of the $m_s = 0$ and $m_s = 1$ sublevels to be distinguished.

As can be seen from Eq. XX, the sensitivity depends strongly on the coherence time T_2, which in turn depends on the number of applied pulses k in the XY8-k sequence and the details of the interaction between between the sensing qubit and its environment. In most cases of interest, the coherence time tends to increase with increasing k. As a specific example, for a Lorentzian noise bath in the limit of long correlation time [117] the coherence time increases as $T_2 = T_2^{SE} k^{2/3}$, where T_2^{SE} is the spin echo (single π-pulse) coherence time. In this case the optimal sensitivity becomes (neglecting T_R)

$$\delta B_{min}^2 \sqrt{t} \approx \frac{1}{(T_2^{SE})^{9/2} f^3}. \tag{B.15}$$

where $f = 1/\tau$ is the modulation frequency. As can be seen from Eq. XX, the sensitivity becomes dramatically worse for low-frequency signals. This effect illustrates the reasoning behind detecting ^{14}N at high magnetic field (see Fig. 3.3C).

The intrinsic NV decoherence manifests itself as an additional exponential decay factor in the population signal [33]:

$$S(\tau) = \frac{1}{2}\Big(1 - e^{-\langle \phi^2 | / \rangle 2 - (\Gamma\tau)^p}\Big), \tag{B.16}$$

where $\Gamma = 1/T_2$ is the NV decoherence rate and p is a parameter that varies between 1 and 3. In all figures presented in this work, the intrinsic decoherence is normalized out.

B.9 Density Functional Theory Simulations

Historically, the nuclear quadrupole splitting was detected by experiments such as Mössbauer spectroscopy, and is caused by the coupling between the nuclear quadrupole moment and the local electric field gradient that arises from the nearby electronic charge density. Advances in understanding of this effect have been significantly aided by the development of first-principles density functional theory (DFT), a method for obtaining accurate electronic charge densities in the ground state. Excellent agreement between DFT results and experiment in what concerns the nuclear quadrupole splitting has been demonstrated for various materials, for example Fe [118]. This is evidence that DFT describes accurately the electric field gradient, which depends sensitively on the electron density near the nucleus [119].

We employ an all-electron full-potential linearised augmented-plane wave (FP-LAPW) DFT calculation, implemented in the ELK code [120]. The core states near the nucleus, included in this all-electron formalism, are crucial for accurate electric field gradient (EFG) tensor evaluations. The local density approximation (LDA) [121] exchange-correlation functional is used with a reciprocal k-grid size of 13x13x5 for bulk h-BN and 13x13x1 for the bilayer and monolayer h-BN crystals. In the all-electron code, the wave function behaves differently near the atomic cores and in the interstitial space between the cores, which are divided by a muffin-tin radius $R_{\mathrm{MT}} = 0.61$Å. The maximum angular momentum used for the augmented-plane wave is 10 and the plane wave basis for the interstitial region has a cutoff $8R_{\mathrm{MT}}^{-1}$. We obtain the EFG tensor at the nuclear sites from the converged ground state electron density at the in-plane lattice constant determined by total-energy minimization.

We further investigate the effects of strain on the electric field gradient at the nucleus. We numerically calculate the response of the EFG to variations in the inter-layer spacing (Fig. B.2A). Here the EFG approaches the monolayer value for spacing higher than ∼5 Å. If the strain is assumed to be in-plane it can be described by the displacement field $\vec{u} = (u_x, u_y)$. Locally, the strain field is characterized by $u_{ii} = \partial_i u_i$ with $i = x, y$ and $u_{xy} = \partial_x u_y + \partial_y u_x$. Assuming a slowly varying DC strain field in space, the changes in the local electric field gradient tensor at the nucleus can be expanded up to the linear leading order of u_{ij} as:

$$M_{\text{EFG}} \approx M^0_{\text{EFG}} + t_1(u_{xx} + u_{yy})M_1 + t_2[(u_{xx} - u_{yy})M_2 + u_{xy}M_3] \tag{B.17}$$

with unperturbed electric field gradient tensor $M^0_{\text{EFG}} = \lambda_0 M_1$ and the 3×3 matrices M_i whose form is constrained by the D_{3h} group theory representation for the h-BN crystal:

$$M_1 = \begin{bmatrix} -1 & 0 & 0 \\ 0 & -1 & 0 \\ 0 & 0 & 2 \end{bmatrix}, M_2 = \begin{bmatrix} 1 & 0 & 0 \\ 0 & -1 & 0 \\ 0 & 0 & 0 \end{bmatrix}, M_3 = \begin{bmatrix} 0 & 1 & 0 \\ 1 & 0 & 0 \\ 0 & 0 & 0 \end{bmatrix}, \tag{B.18}$$

For the bulk h-BN crystal, the DFT estimates are: $\lambda_0 = -1519.5$ V/nm^2, $t_1 = 1210.5$ V/nm^2 and $t_2 = -3921.1$ V/nm^2 at in-plane lattice constant $a = 2.50$ Å and c-axis 3.33 Å for the boron sites. In the case of in-plane isotropic strain, the lattice constant to $a + \delta a$ with $u_{xx} = u_{yy} = \delta a/a$, $u_{xy} = 0$, $\delta M_{\text{EFG}} = 2t_1 M_1 \delta a/a$ which gives $\delta V_{zz} = 4t_1 \delta a/a$ (see Fig. B.2B). This dependence of the EFG on the in-plane lattice constant implies that lattice constant changes as small as ∼50 femtometers (corresponding to 1 kHz shift in $\overline{Q}$) can be detected using our technique.

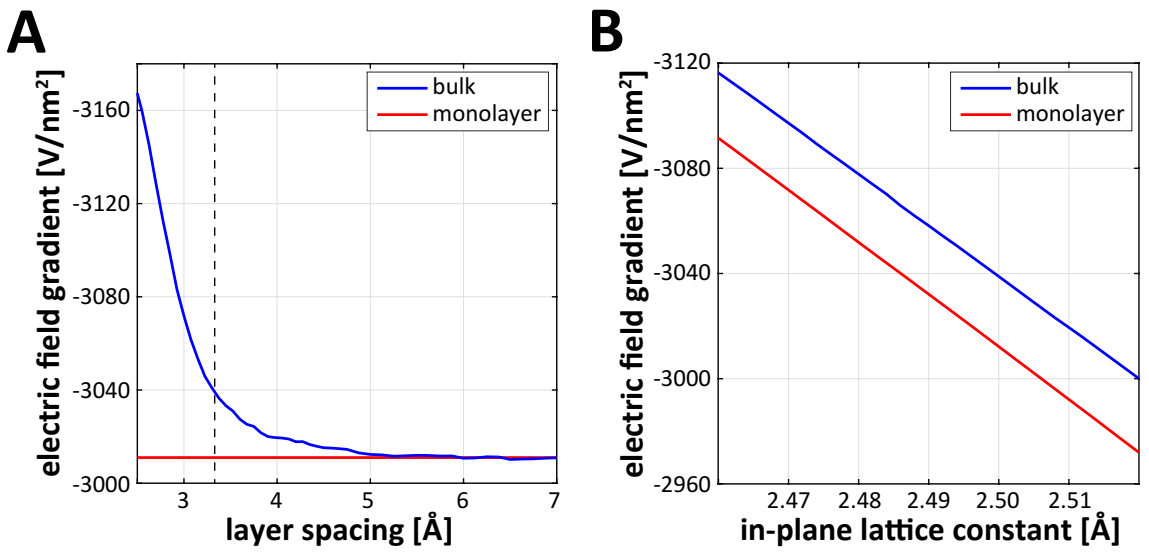

Figure B.2: **Sensitivity of EFG to changes in lattice constants. (A)** Variations of bulk EFG as a function of inter-layer spacing (blue). The curve approaches the monolayer value (red) when the layers are far apart. Dashed black line indicates bulk h-BN layer spacing of 3.33 Å. **(B)** Variation of bulk EFG as a function of in-plane lattice constant. Blue and red curves denote the bulk and monolayer variations, respectively.

B.10 Point Charge Model of EFG Shift

In order to qualitatively understand the origin of the observed EFG shift in the monolayer and bilayer configurations we consider a simple toy model in which the in-plane sp^2 electrons are modeled as classical point charges at interstitial sites between the boron and nitrogen ions. In order to preserve charge neutrality we assign a charge of $-8/3e$ to the valence electrons and $+3e$ and $+5e$ to the boron and nitrogen ions, respectively. Here e is the elementary charge. The EFG at the boron site is calculated by summing up the proximal point charges in the monolayer, bilayer and bulk configurations. We find that the fractional EFG shift (relative to bulk) is -0.015% and -0.03% in the bilayer and monolayer configurations, respectively.

B.11 Determination of h-BN Thickness

To identify monolayer and bilayer h-BN flakes we use three techniques: relative intensity of the h-BN Raman peak at 1366 cm^{-1}, relative intensity of second harmonic generation (SHG), and atomic force microscope (AFM) height measurements.

First, thin flakes are identified in an optical microscope under white illumination, where candidate monolayer and bilayer flakes have the faintest optical contrast. To determine the specific number of layers in a flake, we measure the intensity of the characteristic h-BN Raman line near 1366 cm^{-1}, which scales with the layer thickness [115]. Fig. B.3A shows the background-subtracted Raman spectra for a series of flakes of different thicknesses. The spectra clearly separate into discrete groups and are differentiated by a well-defined intensity step. We find that the Raman signal intensity accurately identifies monolayer and bilayer flakes, while Raman frequency shifts varies sample to sample, possibly due to the variations in strain. We verify that the discrete intensity steps correspond to thickness changes of a single monolayer by AFM height measurements at step interfaces within the flakes (Fig. B.3B). Given the regularity of the intensity change with layer number, we conclude that the flakes in the group with the smallest Raman intensity must be monolayers.

As a final confirmation, we compare optical SHG for different numbers of layers. SHG should only occur in h-BN flakes with an odd number of layers due to a lack of inversion symmetry [122]. Figure B.3C (bottom) shows the result of a SHG measurement (excitation with 880 nm light and collection at 440 nm), where the flake region identified by Raman spectroscopy to be a monolayer exhibits a strong SHG signal while the adjacent bilayer region shows no SHG signal.

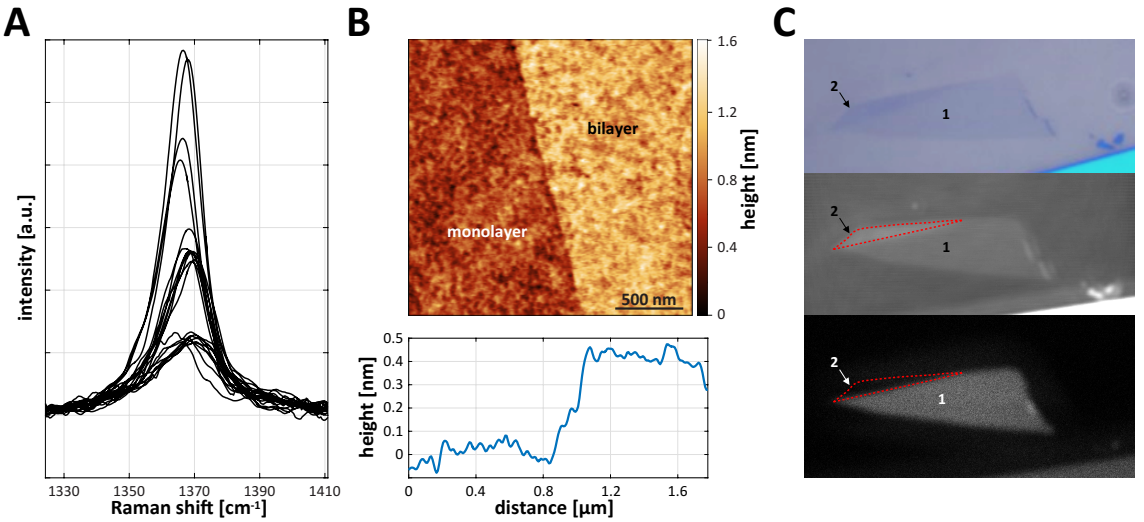

Figure B.3: **Identification of monolayer and bilayer flakes of h-BN. (A)** Raman spectroscopy of thin h-BN flakes. Intensity of the E2g Raman peak is proportional to the number of layers. **(B)** Atomic force microscope height image (top) of the interface between a monolayer and bilayer flake showing a step height of ∼0.4 nm. Bottom plot shows a cross-section of the step. **(C)** White light reflection image of the same h-BN flake (top). The monolayer and bilayer regions are labeled by numbers 1 and 2. Middle panel shows a scanning confocal laser image of same flake with excitation and collection at 440 nm. Bilayer region shows greater reflection. Bottom panel shows SHG contrast measured by exciting with 880 nm light and collecting at 440 nm. The monolayer region shows strong SHG signal due to broken inversion symmetry, while the bilayer region shows no SHG signal.

B.12 Measurements of ^{1}H NMR

It has been shown that diamond samples exposed to ambient laboratory conditions, even briefly, contain a 1 to 2 nm layer of adsorbed water or adventitious hydrocarbons [69, 48] on their surfaces. We use ^{1}H NMR to probe this layer.

As in our NQR experiments, a modified XY8-k pulse sequence (see above) is used to collect information about various Fourier components of the local magnetic noise spectrum. The magnetic field is aligned with the NV symmetry axis and the magnitude of the field is tuned such that the ^{1}H resonance (which coincides with the Larmor frequency for a spin-1/2) is at some specified modulation frequency.

Figure B.4A shows a typical ^{1}H NMR signal at 163 G. Here the NV center is located under a h-BN bilayer and also exhibits a ^{11}B NQR resonance. The data is fit to a model function, similar to that discussed in Section A.6 (see [35]). Based on the depth of this NV center extracted from the ^{11}B NQR spectrum (5.0 $\pm$ 0.1 nm) – or more precisely, the distance of the NV center from the h-BN flake – the amplitude of the ^{1}H signal is far larger than would be expected for a 1 nm layer of water or hydrocarbons. Indeed, in our experiments the h-BN flake is protected on the backside (see Fig. B.1A) by a thick (greater than 1 μm) layer of Poly(Bisphenol A carbonate), containing 40 protons per nm^3. This large ^{1}H signal (effectively from a proton halfspace) allows us an independent estimation of the NV depth. As shown in Fig. B.4B for three representative NV centers, the depths extracted from ^{1}H NMR are smaller than those extracted from ^{11}B NQR by 1 to 2 nm. This result is in excellent agreement with literature values reported previously [69]. In our estimation of the depth from the ^{1}H signal, we assume that the proton density in the adsorbed surface layer is the same as that in the polycarbonate film.

The presence of proximal proton spins on both sides of the h-BN flake also provides a possible mechanism for explaining the NQR line broadening observed in some monolayer and bilayer spectra (Fig. 3.4B). Here we estimate the presence of a single ^{1}H spin, separated from a ^{11}B spin by 2 Å, would increase the linewidth to $\sim$22 kHz. An additional mechanism that could potentially account for broadening of NQR lines is local strain, which would lead to an inhomogeneous distribution of $\overline{Q}$ and non-zero asymmetry parameters η.

Surprisingly we found that while some NV centers under a monolayer h-BN flake

were shallow enough (based on their ^{1}H signal) to yield a NQR signal, they showed no obvious ^{11}B signal. A possible explanation of this effect is hydrocarbon bubbles that have been shown to form under h-BN flakes [123]. In this case, for some NV centers the flake is simply too far away to be detectable via NQR.

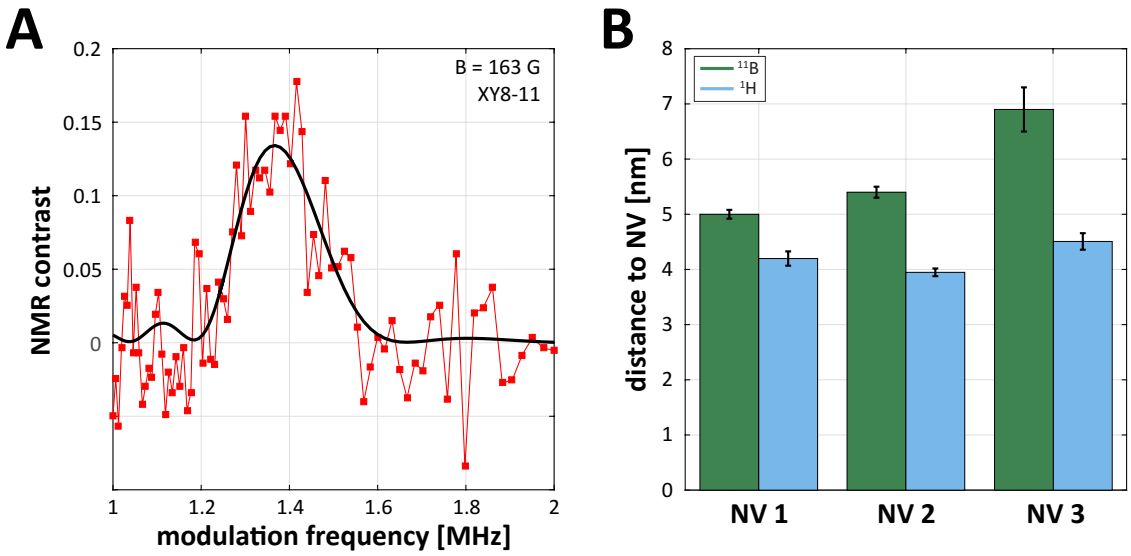

Figure B.4: **Probing the native layer of water or adventitious hydrocarbons on the diamond surface. (A)** Typical ^{1}H NMR signal taken on shallow NV (under an h-BN bilayer) using a XY8-11 pulse sequence. Magnetic field is 163 G. **(B)** The extracted depths for three representative NV centers using ^{1}H NMR (blue) and ^{11}B NQR (green). Error bars are 1-sigma uncertainties.

Appendix C

Supporting material for Chapter 4

C.1 Materials and Methods

C.1.1 Diamond Samples

The samples used in this work were polished, single-crystal electronic grade diamonds grown by chemical vapor deposition (Element Six). The diamonds were {100}-cut, and contained substitutional nitrogen and boron in concentrations less than 5 parts per billion (ppb) and 1 ppb respectively. Prior to implantation, the diamond surface was etched approximately 1 μm, using an Ar-Cl_2 plasma etch (25 sccm Ar, 40 sccm Cl_2, ICP RF 400 W, bias RF 250 W, duration 150 s), followed by an O_2 plasma etch (30 sccm O_2, ICP RF 700 W, bias RF 100 W, duration 150 s). Nitrogen implantation was done by INNOViON Corporation using a $^{15}N^+$ dosage of 10^9 cm^{-2} and an implantation energy of 3 keV, corresponding to a SRIM calculated depth of (5.3 $\pm$ 2.2) nm. The implanted diamonds were annealed in vacuum

using the following procedure: (a) 2 hour ramp to 400°C, (b) 4 hours at 400°C, (c) 2 hour ramp to 800°C, (d) 8 hours at 800°C and (e) 4 hour ramp to room temperature. After annealing, the diamonds were cleaned in a 3-acid mixture (equal volumes of concentrated H_2SO_4, concentrated HNO_3, and 1 M $HClO_4$) for two hours under reflux conditions, followed by air annealing for 10 hours at 420°C.

C.1.2 Optical Setup

We used a home-built scanning confocal microscope to optically address and read out single NV centers. The diamond was placed with NV-side down on top of a No. 0 glass coverslip. The inverted Nikon Plan Fluor 100x oil immersion objective (NA = 1.3) was positioned under the coverslip. Its vertical position is controlled with a piezoelectric scanner (Physik Instrumente P-721 PIFOC) and the lateral position of the laser beam focus was controlled with a closed-loop scanning galvanometer (Thorlabs GVS012). Optical excitation was performed with a 532 nm laser (Information Unlimited, MLLIII532-200-1) modulated with an acousto-optic modulator (Isomet Corporation, 1250C-974) in a double-pass configuration. NV center fluorescence was filtered with a 532 nm notch filter (Semrock, NF03-532E) and a 633 nm long-pass filter (Semorck, LP02-633RU) and collected using an avalanche photodiode (PerkinElmer, SPCM-AQRH-14-FC). The TTL voltage pulses used in our measurements were produced using a 400 MHz PulseBlasterESR-PRO pulse generator from Spincore Technologies.

C.2 Sample Preparation

C.2.1 Diamond Surface Cleaning Procedure

The diamond cleaning procedure was optimized to minimize background fluorescence and to ensure that the surface was terminated with carboxyl groups. The samples were cleaned in a 3-acid mixture (equal volumes of concentrated H_2SO_4, concentrated HNO_3, and 1 M $HClO_4$) for 4 hours under reflux conditions, followed by concentrated ultrapure (99.999%) HNO_3 at 90°C for 1 hour, 1.0 M of NaOH at 90°C for one hour and 1.0 M of HCl at 90°C for one hour. The diamonds were washed with ultrapure water after each step.

C.2.2 Gd^{3+}-Molecule Attachment Procedure

Gd^{3+} molecules were synthesized and purified using methods discussed in [124]. To activate the surface carboxyl groups, the diamonds were treated in a solution of 1-ethyl-3-(3-dimethylaminopropyl)carbodiimide (EDC; 100 μM) and *N*-hydroxysuccinimide (NHS; 100 μM) at room temperature for 12 hours. After rinsing with ultrapure water, the diamonds were placed in a 1 mM Gd^{3+}-molecule solution and reacted at room temperature for 2 hours. The diamonds were then rinsed with ultrapure water. The surface density of attached molecules could be decreased by diluting the Gd-ligand solution.

C.2.3 Gd^{3+}-Molecule Removal Procedure

We repeated the cleaning procedure described above to hydrolyze the peptide bonds and remove the Gd^{3+} molecules from the diamond surface.

C.3 Determination of Gd^{3+}-Molecule Surface Density

C.3.1 Atomic Force Microscopy

We used an Asylum MFP-3D atomic force microscope (AFM) in AC mode to image the surfaces of our diamond samples, in air. The probes (Nanosensors SSM-FMR) had a spike radius of (3 ± 2) nm and a resonant frequency between 45 and 115 Hz. Samples were mounted onto cover slides using SPI die-cut nonconductive double-sided adhesive discs. The AFM trace and retrace data were averaged together linearly.

A typical AFM height image of a diamond surface after Gd^{3+} molecule attachment is shown in Fig. C.1A. We determined the mean separation between the surface molecules to be in the range 20 nm to 25 nm. The radii of the circular features (see Fig. C.1C) are consistent with the lateral resolution limit imposed by the AFM tip while the height (see Fig. C.1B) is consistent with that expected for single Gd^{3+} molecules, estimated from bond lengths and angles. The orientation of the molecules on the surface in ambient conditions is unknown, and the variation of orientations likely contributes to the range of AFM spot heights.

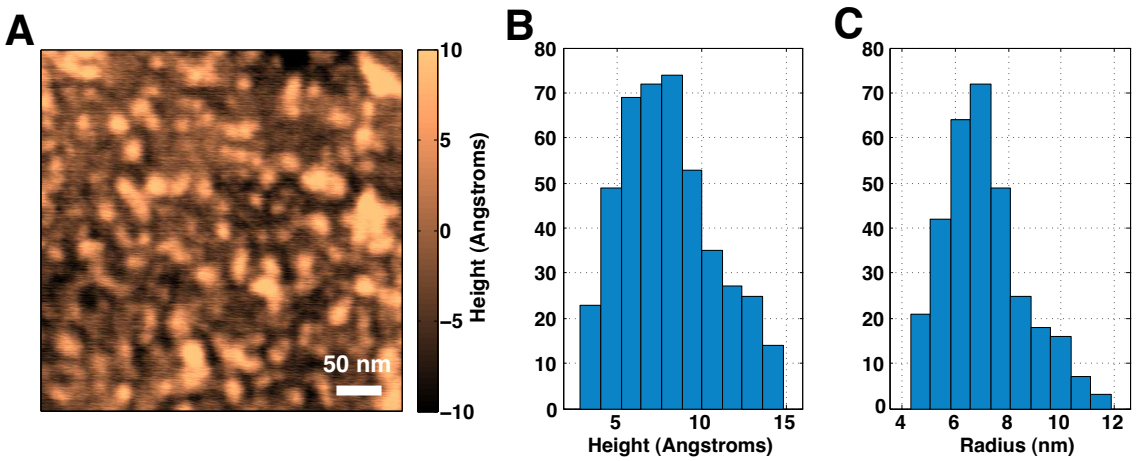

Figure C.1: **Determination of the size of a single Gd^{3+} molecule. (A)** 350 nm × 350 nm AFM height image of a diamond surface with Gd^{3+} molecules attached. **(B)** Histogram of the heights of the circular features in an larger AFM image, of approximate size 3 μm × 3 μm. The mean height of a single Gd^{3+} molecule is determined to be (8 ± 3) Å. **(C)** Histogram of the radii of these features. The mean radius of a feature that corresponds to a single Gd^{3+} molecule is found to be (7 ± 2) nm.

To confirm that these surface features are indeed single Gd^{3+} molecules, we attached to each molecule a single Cy3 fluorescent dye, attached the resulting Cy3-Gd^{3+} molecule to the diamond surface, and correlated the Cy3 fluorescence rate observed in our confocal microscope with the surface density observed in the AFM images. We calibrated the fluorescence rate of a single Cy3-Gd^{3+} molecule by attaching an optically resolvable concentration (achieved by diluting the stock ligand solution) of these molecules to the diamond surface and monitoring the fluorescence rate in the 542 - 633 nm band, filtering out fluorescence from NV centers (Fig. C.2A). A typical fluorescence time trace of a single Cy3-Gd^{3+} molecule under CW 532 nm illumination (2 μW) is shown in Fig. C.2B and displays a photo-bleaching pattern characteristic of a single-molecule emitter. We detected a mean fluorescence rate of 1200 photons/second from a single fluorescent Cy3-Gd^{3+} molecule. At high concentration, the surface molecules were no longer optically-resolvable (Fig. C.2C) but the fluorescence

rate in a diffraction-limited focal spot suggested a mean surface density in the range $1/(20\text{ nm})^2$ to $1/(25\text{ nm})^2$, consistent with that obtained in AFM measurements described above. Finally, inspection of this area of the surface in the AFM revealed circular features with height, radius and density that were in good agreement with those found after attaching Gd^{3+} molecules (see Fig. C.2D).

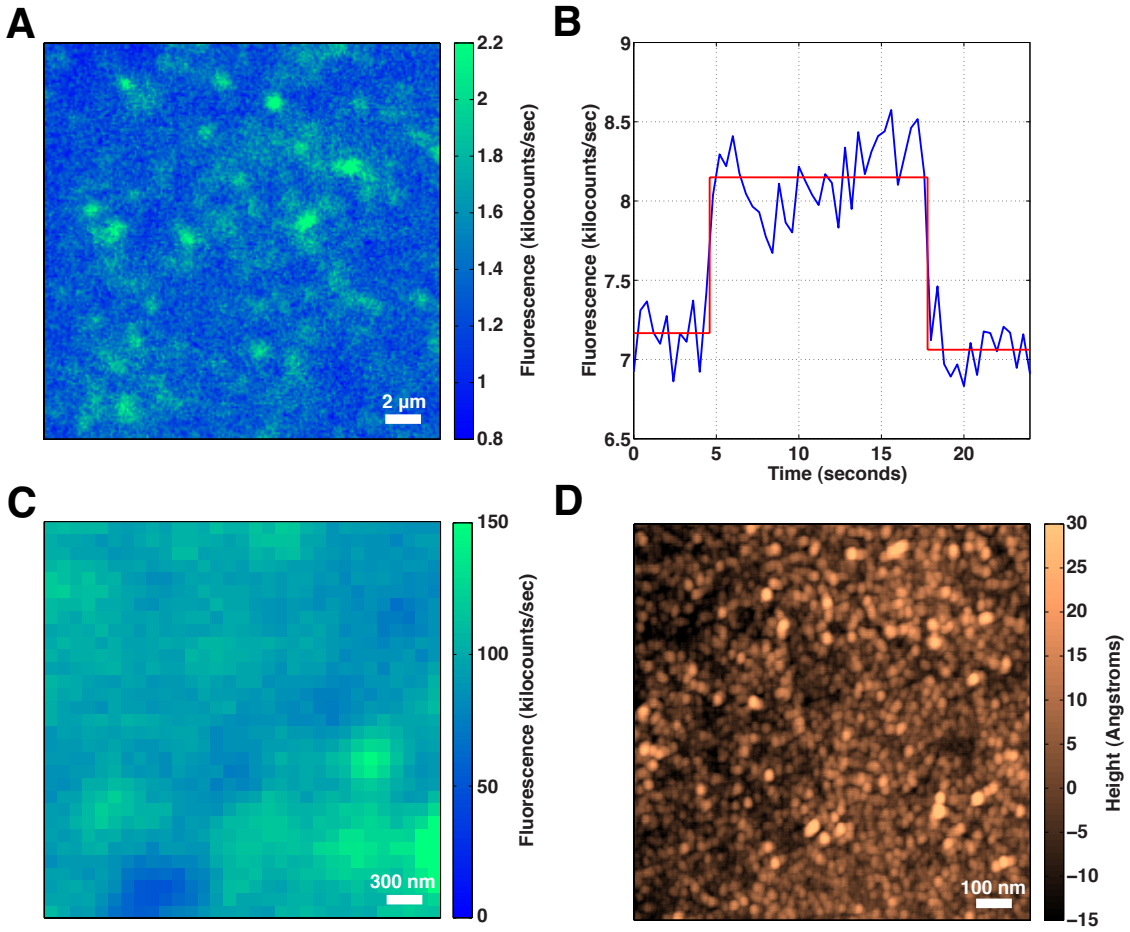

Figure C.2: **Determination of Gd^{3+} molecule surface density.** **(A)** 20 μm × 20 μm fluorescence image of single Cy3-ligand molecules. **(B)** Photobleaching of a single Cy3-ligand molecule under CW 532 nm laser illumination (2 μW). **(C)** 3 μm × 3 μm fluorescence image of a diamond surface saturated with Cy3-ligand molecules. **(D)** 1 μm × 1 μm AFM height image of the same diamond surface as in Fig. C.2C.

We conclude that the observed features are indeed single Gd^{3+} molecules. We note

that the surface concentration could be controlled by diluting the ligand solution and our attachment procedure resulted in a uniform distribution of molecules, with little aggregation.

These molecules are attached to the diamond via the surface carboxylic groups. Some surface carboxylic groups may be chemically unreactive (due, for example, to steric hindrance by neighboring surface groups, or other surface structure considerations [125, 126, 127]) and do not attach the Gd^{3+} molecules. From our measurements we conclude that the surface density of the "reactive" carboxylic groups is in the range $1/(20\text{ nm})^2$ to $1/(25\text{ nm})^2$.

C.4 Co-localization Procedure

C.4.1 AFM Drift Correction

It took on the order of an hour to acquire each of the AFM scans used in our measurements. During that time, the AFM image underwent lateral drift, with typical magnitude of 10 nm per hour to 100 nm per hour. This introduced a shift in the relative positions of the features at the top of an AFM image, taken near the beginning of a scan, relative to the features at the bottom of an AFM image, taken near the end of the scan. In order to correct for the drift, we always acquired two consecutive AFM scans of the same area of the diamond surface, and, using numerical image processing, extracted the magnitude of the drift. We then corrected each of the two images for this drift, and averaged them together.

C.4.2 Co-Localization Steps

We determined the separation between an NV centre and the nearest Gd^{3+} molecule in a three-step co-localization procedure. First, the diamond surface was coated (via electrostatic attachment) with an optically resolvable density of 100 nm-diameter gold nanoparticles. These nanoparticles fluoresce in the same spectral region as the NV centers, and thus could be observed simultaneously with NV centers in our scanning confocal microscope. We compiled a map of the surface positions of these nanoparticles, together with a map of the NV centers in the same region (Fig. 4.2A). In the second step, the surface topography of this diamond was measured using the AFM (Fig. 4.2B). The gold nanoparticles could be clearly seen, together with a number of topographic features (pits and scratches) in the diamond surface, thus enabling us to compile a map of the positions of these surface features relative to the nanoparticles. Finally, after cleaning off the nanoparticles, we attached Gd^{3+} molecules to the diamond surface, and the diamond surface topography was measured using the AFM, yielding a map of the positions of the Gd^{3+} molecules in relation to the surface features. We used these three maps to deduce the positions of the Gd^{3+} molecules relative to the NV centers (Fig. 4.2C).

C.4.3 Co-Localization Uncertainty

The uncertainty in the position of an NV center relative to the Gd^{3+} molecules on the diamond surface was estimated by combining the uncertainties in each of the co-localization steps in quadrature. The dominant uncertainty, on the order of 10 nm, arose when matching the fluorescence and AFM maps of the nanoparticle posi-

tions. We used between 9 and 15 nanoparticles in this step. Their coordinates were extracted from Gaussian fits to the fluorescent spots in the confocal scan, and from spherical-dome fits to the corresponding features in the AFM scan. We deduced the position of the NV center in the AFM image by finding the transformation (scaling + rotation) that most accurately maps the fluorescence-scan coordinates of the nanoparticles to their coordinates in the AFM image and applying this transformation to the NV center fluorescence-scan coordinates. In order to estimate the associated uncertainty in the NV center AFM-scan coordinates, we ran Monte Carlo simulations that shifted each of the nanoparticles by a randomly-oriented normally distributed vector with a standard deviation equal to the mean distance between the transformed fluorescence-scan coordinates and the AFM-scan coordinates of the nanospheres, and then calculated the resultant NV center AFM positions. We set the uncertainty in the NV center AFM coordinates to be equal to the standard deviation of the resulting Gaussian distribution of the NV positions, see Fig. C.3. A similar procedure was implemented to estimate the uncertainties arising from the other two co-localization steps. The resulting total uncertainty was typically 15 nm.

C.5 Derivation of $\Gamma_{induced}$

We describe an NV center interacting with a bath of Gd^{3+} molecules by the Hamiltonian ($\hbar = 1$)

$$H = \frac{\Delta}{2}\sigma_z + \frac{1}{2}g\mu_B \left[B_x(t)\sigma_x + B_y(t)\sigma_y\right] \tag{C.1}$$

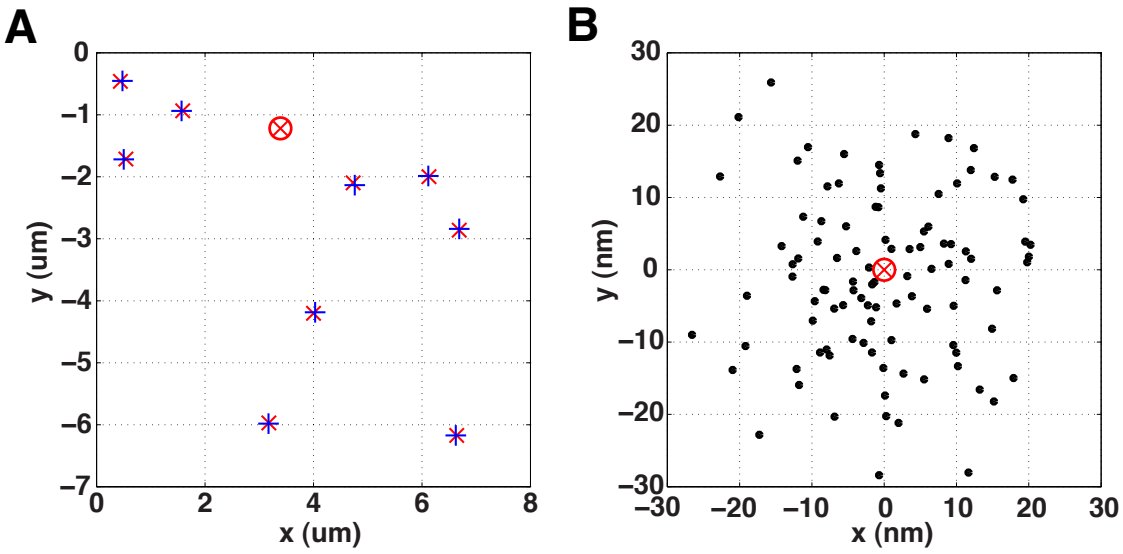

Figure C.3: **Determination of co-localization uncertainty. (A)** The transformed fluorescence image coordinates of an NV center (red circle with a cross) and the gold nanoparticles (all the other red crosses) overlayed on the AFM image coordinates of the same gold nanoparticles (blue crosses). **(B)** Monte Carlo simulation used to determine the error on the NV center position in Fig. C.3A. The red circle with a cross shows the most probable position of the NV center (normalized to the origin) while the blue dots show the distribution of possible positions that arise from the imperfect overlap of the fluorescence and AFM coordinates in Fig. C.3A. We take the standard deviation of the distribution of these positions to be the co-localization uncertainty. For the NV center shown this is approximately 10 nm, and the average value for all the NV centers is 15 nm.

where $\Delta \approx 2.87$ GHz is the zero-field splitting of the NV center, $g \approx 2$ is the electron g-factor, μ_B is the Bohr magneton, $\sigma_{x,y,z}$ are the Pauli spin operators, and $B_{x,y}(t)$ are the transverse components of the fluctuating magnetic field created at the NV center by the proximal Gd^{3+} spins. Here we consider the dynamics within the two-level subspace spanned by the states $|0\rangle$ and $|1\rangle$ of the NV center ground state triplet and treat $B(t)$ as a classical variable. The z-axis is chosen to be along the symmetry axis of the NV center and we ignore the term $\frac{1}{2}g\mu_B B_z(t)\sigma_z$ since its effect is suppressed by the large zero-field splitting. We take the state of the effective two-level system to

be

$$|\psi(t)\rangle = \alpha(t)|0\rangle + \beta(t)|1\rangle. \tag{C.2}$$

For an NV center initially prepared in the $|0\rangle$ state, first-order time-dependent perturbation theory in the interaction pictures gives [128]

$$\beta(t) = \frac{-i}{2} g\mu_B \int_0^t d\tau [\langle 1|\sigma_x(\tau)|0\rangle B_x(\tau) + \langle 1|\sigma_y(\tau)|0\rangle B_y(\tau)] = \frac{-i}{2} g\mu_B \int_0^t d\tau e^{i\Delta\tau} B_\perp(\tau) \tag{C.3}$$

for the amplitude of state $|1\rangle$. Here $B_\perp$ is the transverse component of the fluctuating magnetic field. Averaging over the classical variable $B_\perp(\tau)$, the transition probability is given by

$$P_1(t) = |\beta(t)|^2 = \frac{1}{4} g^2 \mu_B^2 \int_0^t d\tau_1 \int_0^t d\tau_2 e^{-i\Delta(\tau_1 - \tau_2)} \langle B_\perp(\tau_1) B_\perp(\tau_2)\rangle. \tag{C.4}$$

Using the Wiener-Khinchin theorem, the transition rate becomes

$$\Gamma_{0\to 1} = \frac{1}{4} g^2 \mu_B^2 S_B(-\Delta), \tag{C.5}$$

where $S_B(-\Delta)$ is the power spectral density of $B_\perp(\tau)$. Similarly, if we start with the NV center in state $|1\rangle$, the transition rate is given by

$$\Gamma_{1\to 0} = \frac{1}{4} g^2 \mu_B^2 S_B(\Delta) \tag{C.6}$$

Treating the fluctuating field as a classical variable imposes the condition that $\langle B_\perp(\tau) B_\perp(0)\rangle$ is real and thus $\Gamma_{1\to 0} = \Gamma_{0\to 1} = \Gamma$. For the specific case of the NV center interacting with a fluctuating Gd^{3+} spin, we assume a telegraph noise spectrum given by

$$S_B(\Delta) = \frac{2\langle B_\perp^2\rangle \gamma}{\gamma^2 + \Delta^2} \tag{C.7}$$

where $\langle B_\perp^2 \rangle$ is the time-averaged magnetic field component, perpendicular to the NV axis, produced at the NV center by the Gd^{3+} spin and $\gamma = 1/T_1^{Gd}$ is the characteristic spectral width (see Fig. 4.3A of the main text) given by the Gd^{3+} relaxation rate.

To calculate the induced relaxation rate in our experiment we must account for the 3-level structure of the NV center and consider the transition rates between levels $|0\rangle$ and $|-1\rangle$ of the ground state manifold. Because our measurements of the relaxation rates are done in earth magnetic field, levels $|1\rangle$ and $|-1\rangle$ are approximately degenerate and we assume that

$$\Gamma_{0\to-1} \approx \Gamma_{0\to1} = \Gamma. \tag{C.8}$$

Accounting for the 3-level structure, the $|0\rangle$ state population evolves in time according to

$$P_0(t) = \frac{1}{3} + \frac{2}{3}e^{-3\Gamma t} = \frac{1}{3} + \frac{2}{3}e^{-\Gamma_{induced} t} \tag{C.9}$$

where the effective induced relaxation rate is $\Gamma_{induced} = 3\Gamma$.

A single fluctuating Gd^{3+} magnetic dipole moment μ a distance r away from the NV center creates the magnetic field $\langle B_\perp^2 \rangle = 4\mu^2/3r^6$. For a Gd^{3+} ion with spin $S = 7/2$, the dipole moment is $\mu = g\mu_B\sqrt{S(S+1)}$.

Combining the above expressions, we obtain the scaling of the NV-center sublevel population relaxation rate induced by a single fluctuating Gd^{3+} ion a distance r away:

$$\Gamma_{induced} = 2\frac{S(S+1)g^4\mu_B^4}{r^6}\frac{\gamma}{\gamma^2+\Delta^2}. \tag{C.10}$$

The NV-center sublevel population relaxation rate induced by other paramagnetic species (such as other lanthanide ions) can also be calculated using this expression.

C.6 Co-localization Simulation

The Monte-Carlo simulations of the experiment, shown in Fig. 4.4, were performed as follows. For a random distribution of Gd^{3+} molecules on the diamond surface, the separation between the NV center and the proximal Gd^{3+} molecule was computed, together with the induced NV center relaxation rate. The mean spacing between Gd^{3+} molecules was taken to be 20 nm, to be consistent with the AFM measurements, and the AFM co-localization uncertainty was taken to be 15 nm. The Gd^{3+} electron-spin relaxation rate has been measured in a number of MRI contrast agents [77], and depends on several factors, such as the local crystal field environment of the Gd^{3+} ion, and the rotational correlation time for solution-phase measurements. Given the range of values quoted in Ref. [77], this relaxation rate in our experiments is likely to be between 1 and 100 GHz . For the Monte-Carlo simulations we took a value of 10 GHz, which produced the best agreement between the simulation and the data points, as measured by the Kolmogorov-Smirnov Z-statistic test (see below). The simulations contain 10^9 realizations of the experiment. The color scale in Fig. 4.4 (inset) shows the probability density of obtaining a particular NV center relaxation rate for a given measured separation between the NV center and the proximal Gd^{3+} molecule.

In order to quantify the agreement between the experimental data points and the expected Gd^{3+}-induced NV center relaxation, we calculated reduced chi-squared statistic for the experimental data and the model presented in Section C.5: $\chi_r^2 = 0.8$. The agreement between the data points and the Monte-Carlo simulations is hard to quantify rigorously. A commonly used nonparametric technique is the Kolmogorov-

Smirnov test, which quantifies the discrepancy between two statistical distributions [129]. Whereas this test is not distribution-independent for multivariate datasets, it is still a useful measure of the goodness-of-fit [130]. The value of the two-variable Kolmogorov-Smirnov Z-statistic for the data shown in Fig. 4.4 (inset) is 1.1, which indicates that the data points are consistent with the simulated distribution. The agreement deteriorated when the simulation was done for other values of NV depth, Gd^{3+} relaxation rate, Gd^{3+} molecule spacing, and co-localization uncertainty. We note that the average NV center depth has the largest effect on the simulation results at small radial separations between the NV center and the Gd^{3+} position ($\lesssim 10$ nm).

C.7 Detecting Gd^{3+}-Molecules by Measuring NV-center Relaxation

C.7.1 Range of Parameters Consistent with Experimental Data

The binned experimental data presented in Fig. 4.4 of the main text were consistent with a range of parameters (average NV-center depth, Gd^{3+} relaxation rate, and Gd^{3+} molecule surface concentration). These parameters were strongly constrained by the experimental data in the inset in Fig. 4.4. However, we can argue that the NV-center interacts, on average, with a single Gd^{3+} molecule, based solely on the binned data presented in Fig. 4.4. For each NV-center depth, Monte-Carlo simulations were performed to determine which values of the Gd^{3+} relaxation rate and surface con-

centration resulted in the best least-squares fit to the data shown in Fig. 4.4. These best-fit values are shown as blue points in Fig. C.4.

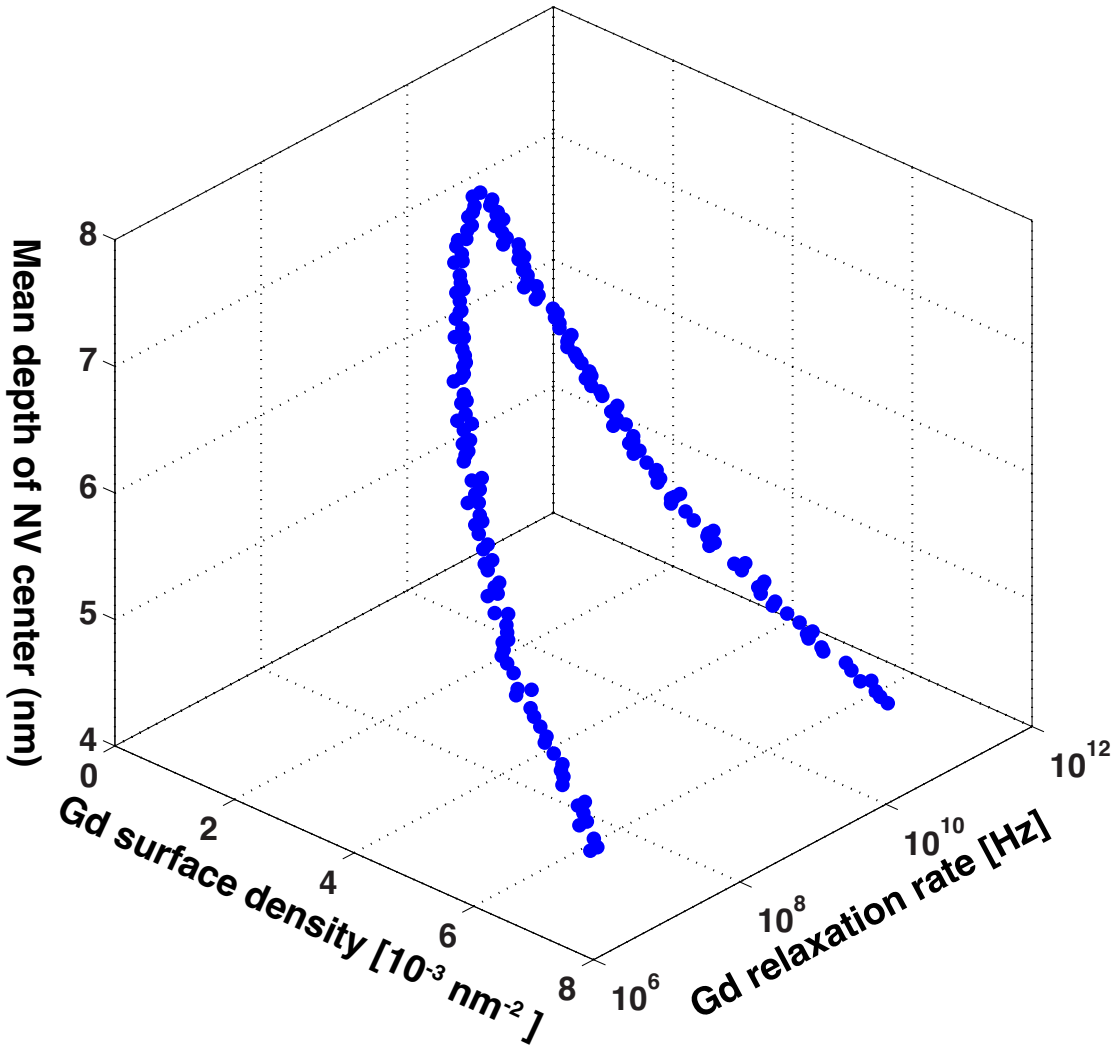

Figure C.4: **The range of experimental parameters that are consistent with the data.** The points show parameter combinations that are consistent with the measured distribution of Gd^{3+}-induced NV-center relaxation rates shown in Fig. 4.4. All the parameter combinations shown by the points result in $\chi_r^2 < 0.7$.

For NV depths greater than approximately 8 nm, all sets of parameters resulted in chi-squared values greater 5 and are therefore inconsistent with the experimental

data. NV-center depths less than 4 nm required a Gd^{3+} relaxation rate above 1 THz, well outside the range of values for this rate found in literature. We note that every suitable combination of parameters (every point on the plot) corresponds to a regime where the induced relaxation rate of the NV center is caused by interaction with a single Gd^{3+} spin (the NV center depth is smaller than the mean spacing between the Gd^{3+} molecules).

C.7.2 Experimental Data Uncertainty Analysis

For the binned experimental data shown in Fig. 4.4, the uncertainties were determined by adding in quadrature the uncertainties resulting from the experimental fitting errors and the bin sampling uncertainties. Each of the 85 measurements (see Fig. 4.3C) was fit with an exponential decay model, yielding the most likely relaxation rate and a one sigma error bar. These errors allow us to determine the probability that a particular measurement lies in a particular histogram bin. We considered all possible ways the 85 measurements can be distributed among the five bins and assign probability values to each distribution. This procedure yielded the most likely number of measurements in each bin and the associated one sigma error bar. Additionally, the probability of getting a particular number of measurements in any bin was related to the stochastic distribution of Gd^{3+} molecules on the diamond surface and was binomially distributed. In particular, given a total of N measurements of the relaxation rate, a bin containing n points would have an associated variance given by $n(1 - n/N)$.

C.7.3 Photon Shot Noise-Limited Detection Sensitivity

A possible paramagnetic molecule detection strategy would be to monitor NV-center fluorescence after optical pumping into the $m_s = 0$ sublevel and a relaxation-in-the-dark period of approximately 2 ms, chosen to be approximately equal to the NV-center intrinsic T_1 time, which we assume to be 5 ms. The photon count rate from a single NV center is typically 5×10^4 s^{-1}. With the 300 ns-long APD photon acquisition window, in such an experiment we can detect approximately 8 photons per second. Given the 30% contrast between the "bright" $m_s = 0$ state, and the "dark" $m_s = \pm 1$ states, a 300 Hz change in NV relaxation rate (which corresponds to detecting a single Gd^{3+} molecule spin at a distance of 10 nm) would result in a photon "signal" of approximately $0.06N_p$, while the "noise" is approximately $\sqrt{N_p}$, where N_p is the detected number of photons. In order to detect this change in NV-center relaxation rate at 3σ confidence level, we need $N_p \approx 2500$ detected photons, which takes approximately five minutes of averaging.

C.8 Control Experiments with La^{3+}-Containing Molecules and Bare Ligand Molecules

In order to demonstrate that the surface chemistry had negligible effect on the relaxation rate of the NV center, we attached bare ligand molecules to the diamond surface. We used the same procedure as for the Gd^{3+} molecules [124], except in this case we never included gadolinium into the 1 mM solution of ligand molecules. After attaching the bare ligand molecules to the diamond surface, it was clear that no

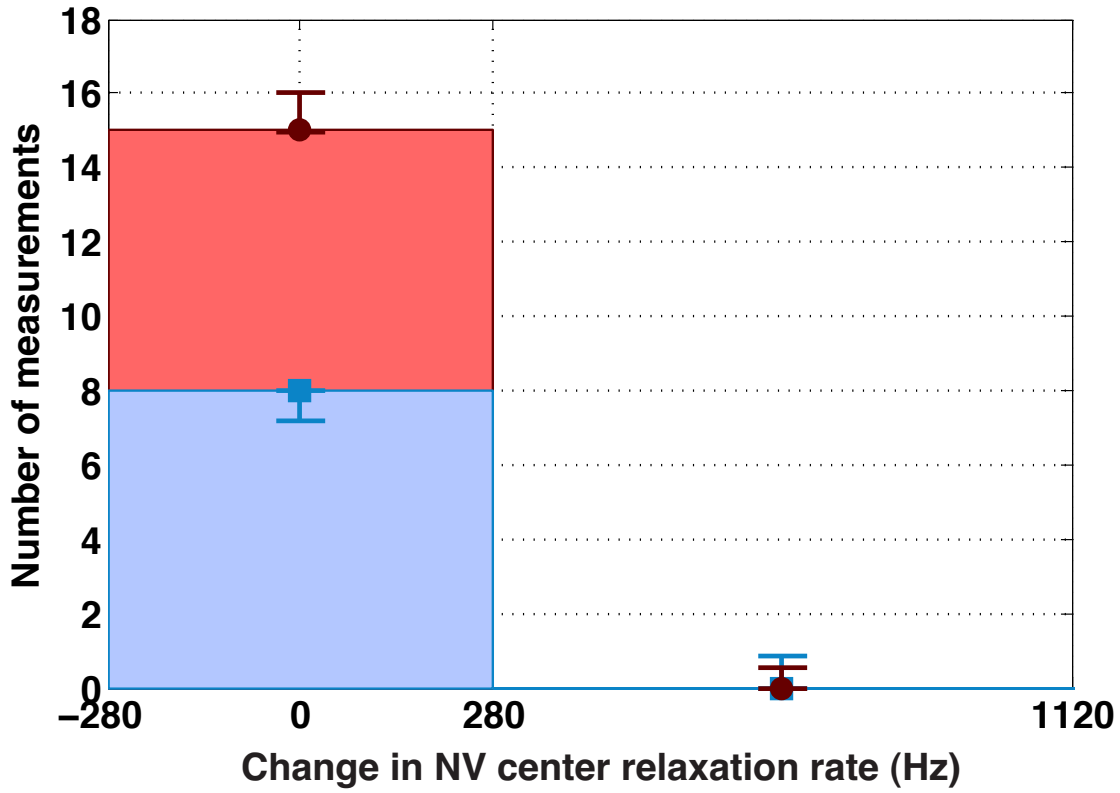

Figure C.5: **Control experiments with bare ligand and La^{3+} molecules.** Experimental results of 16 NV center relaxation rate measurements with bare ligand molecules covalently attached to the diamond surface (red) and 8 NV center relaxation rate measurements with La^{3+} molecules covalently attached to the diamond surface (blue). Within statistical error, the results are consistent with $\Gamma_{induced} = 0$.

significant increase in relaxation rate was observed for the 16 relaxation measurements taken, as expected (Figure C.5). Additionally, we attached La^{3+}-containing molecules to the surface of the diamond. We created La^{3+}-containing molecules in the same way we made Gd^{3+} molecules [124], but instead replaced Gd^{3+} with La^{3+} to create a 1 mM solution of La^{3+}-containing molecules. La^{3+} is chemically identical to Gd^{3+}, but it has no unpaired electron spins and thus we expect to see no enhanced relaxation rate. Indeed, we observed no enhanced relaxation rate for the 8 NV center relaxation measurements taken (Figure C.5).

Appendix D

Supporting material for Chapter 5

D.1 Materials and Measurement Apparatus

D.1.1 Diamond Sample

The sample used in this work is a polished, single-crystal electronic grade diamond grown by chemical vapor deposition (Element Six), containing substitutional nitrogen and boron in concentrations less than 5 parts per billion (ppb) and 1 ppb respectively. Prior to implantation, the {100} diamond surface was etched approximately 2 μm, using an Ar-Cl_2 plasma etch (25 sccm Ar, 40 sccm Cl_2, ICP RF 400 W, bias RF 250 W, duration 150 s), followed by an O_2 plasma etch (30 sccm O_2, ICP RF 700 W, bias RF 100 W, duration 150 s). Nitrogen implantation was done by INNOViON Corporation using a $^{15}N^+$ dosage of 10^9 cm^{-2} and an implantation energy of 2.5 keV. The implanted diamond was annealed in vacuum using the following procedure: (a) 6 hour ramp to 400°C, (b) 6 hours at 400°C, (c) 6 hour ramp to 800°C, (d) 8 hours

at 800°C and (e) 6 hour ramp to room temperature. After annealing, the diamond was cleaned in a 3-acid mixture (equal volumes of concentrated H_2SO_4, HNO_3, and $HClO_4$) for two hours under reflux conditions. The same cleaning procedure was used to re-set the locations of the reporter spins on the diamond surface.

D.1.2 Optical Setup

A home-built scanning confocal microscope was used to optically address and read out single NV centers. An RF transmission line was fabricated on the surface of a glass coverslip, and the diamond was placed NV-side down on top of this coverslip. The inverted Nikon Plan Fluor 100x oil immersion objective (NA = 1.3) was positioned under the coverslip. Its vertical position was controlled with a piezoelectric scanner (Physik Instrumente P-721 PIFOC) and the lateral position of the laser beam focus was controlled with a closed-loop scanning galvanometer (Thorlabs GVS012). Optical excitation was performed with a 532 nm laser (Information Unlimited, MLLIII532-200-1) modulated with an acousto-optic modulator (Isomet Corporation, 1250C-974) in a double-pass configuration. NV center fluorescence was filtered with a 532 nm notch filter (Semrock, NF03-532E) and a 633 nm long-pass filter (Semorck, LP02-633RU) and collected using a single-photon counting module (PerkinElmer, SPCM-AQRH-14-FC). The acousto-optic modulator and the single-photon counting module were gated using TTL pulses produced by a 500 MHz PulseBlasterESR-PRO pulse generator from Spincore Technologies. Typical NV center fluorescence count rate was 20 kHz, and photon counter acquisition window for each sequence repetition was 500 ns.

D.1.3 RF Setup

The RF tones, used to address the NV centers and the surface reporter spins, were generated by two Stanford Research SG384 signal generators. The IQ modulation inputs were used to control the x and y quadrature amplitudes of the generator that addressed the NV center. The RF pulses in each channel were generated by the switches (MiniCircuits ZASWA-2-50DR+), controlled by the TTL pulses from the PulseBlasterESR-PRO, and power boosted by an amplifier (three amplifiers were used, depending on the frequency: MiniCircuits ZHL-20W-13+, ZHL-30W-252-S+, and ZHL-16W-43-S+). The two RF channels were combined using an MCLI PS2-109 power splitter, and coupled into the 50 Ω-terminated RF transmission line with the diamond sample on top.

D.2 NV Centers and Depth Measurements

The DEER experiments were performed on a total of 16 NV centers. 12/16 showed clear DEER collapse due to reporter spins, on the time scale shorter than their $T_2^{(nv)}$, 2/16 showed DEER collapse on the order of $T_2^{(nv)}$, and 2/16 showed no DEER collapse. NVs A and B were selected for their fastest DEER collapse, which likely means they are among the most shallow of the NV centers. Reporter sequence experiments were performed only with NVs A and B.

The depths of each of these two NV centers were determined by covering the diamond surface with immersion oil, and measuring the amplitude of the magnetic field created at the location of the NV center by the immersion oil proton magnetic mo-

ments, precessing at the Larmor frequency. The dynamical decoupling XY-k sequence was used to perform this ac magnetometry experiment, see data shown in Fig. D.1. The details of the fitting procedure are described in Section A.6. This method yielded the following depths: NV A $\rightarrow (3.3 \pm 0.2)$ nm, and NV B $\rightarrow (3.6 \pm 0.3)$ nm.

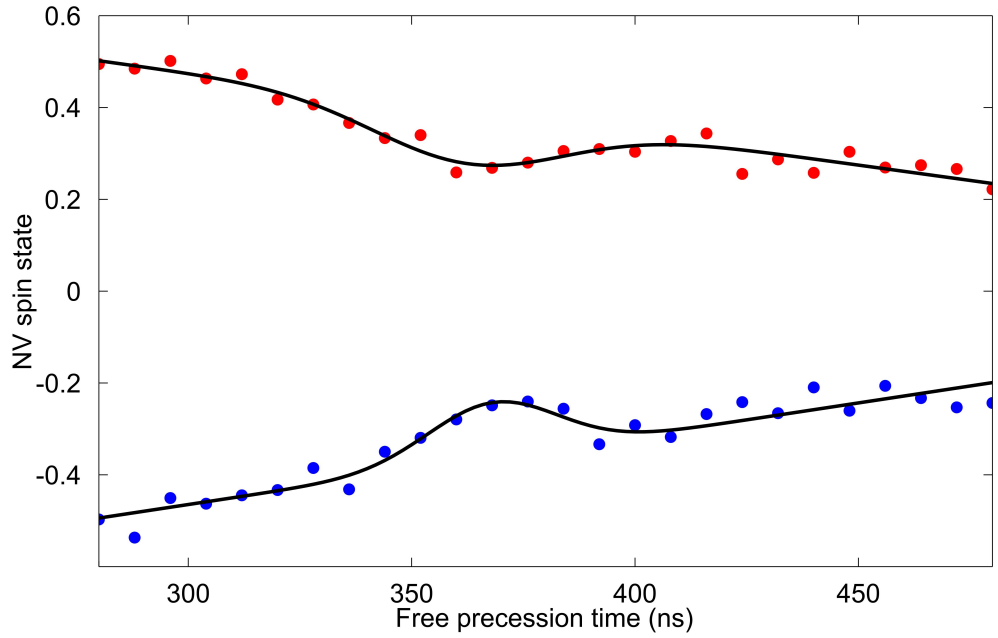

Figure D.1: **The results of dynamical decoupling experiment (XY-16 pulse sequence) on NV A, from which we extract its depth.**

When a separate diamond sample, with an unpolished surface, implanted and annealed with the same parameters as the one used in our work, was treated at 465°C in an O_2 atmosphere [43], we found that the DEER signals were absent for 11 out of the 12 NV centers for which measurements were taken, and one NV center showed a "weak" DEER signal with the DEER collapse on the order of NV decoherence time $T_2^{(nv)}$. We concluded that this treatment removed the reporter spins from the diamond surface.

D.3 Localizing Reporter Spins on the Diamond Surface

D.3.1 The Double Electron-Electron Resonance Experiment

The strength of the magnetic dipole coupling between the NV center and the surface spin network was characterized using the double electron-electron resonance (DEER) pulse sequence.

The dipole-dipole interaction Hamiltonian between the NV center spin $\boldsymbol{S}$ and the surface reporter spin $\boldsymbol{J}$ is:

$$H_d = \frac{\hbar^2\gamma_e^2}{r_s^3}\left[\boldsymbol{S}\cdot\boldsymbol{J} - 3\frac{(\boldsymbol{S}\cdot\boldsymbol{r}_s)(\boldsymbol{J}\cdot\boldsymbol{r}_s)}{r_s^2}\right], \tag{D.1}$$

where $\boldsymbol{r}_s$ is the vector from the NV center to the reporter spin. When the magnetic field B is aligned with the NV center axis, we can neglect all non-secular terms, and consider only the terms that commute with S_z and J_z:

$$H_d = \frac{\hbar^2\gamma_e^2}{r_s^3}\left(1 - 3\cos^2\theta_s\right) S_z J_z = \hbar k_s S_z J_z, \tag{D.2}$$

where θ_s is the angle that vector $\boldsymbol{r}_s$ makes with the magnetic field, and the coupling strength is

$$k_s = \frac{\hbar\gamma_e^2}{r_s^3}\left(1 - 3\cos^2\theta_s\right). \tag{D.3}$$

The NV center $|m_s = 0\rangle$ state population after the DEER sequence with duration t_{nv} is given by

$$S = \frac{1}{2}\left[1 + \cos(k_s J_z t_{nv})\right] = \frac{1}{2}\left[1 + \cos(k_s \sigma^z t_{nv}/2)\right], \tag{D.4}$$

where $\sigma^z = \pm 1$ denotes the sign of the initial projection of the reporter spin.

We have to trace over all the reporter spin projections, and, for several reporter spins, we have to add up the contributions, resulting in

$$S = \frac{1}{2}(1 + \langle \cos \phi_1 \rangle), \tag{D.5}$$

where $\langle\rangle$ denotes averaging over many runs of the experiment (reporter spin projections), and the phase in each run is given by the sum over all reporter spins:

$$\phi_1 = \frac{t_{nv}}{2} \sum_s k_s \sigma_s^z. \tag{D.6}$$

To perform this average, we use $\langle \sigma_s^z \rangle = 0$, $\langle \sigma_s^z \sigma_{s'}^z \rangle = 0$ for $s \neq s'$, $\langle (\sigma_s^z)^2 \rangle = 1$, which yields

$$S \;\; = \tfrac{1}{2} \left[1 + \textstyle\prod_s \cos(k_s t_{nv}/2) \right]. \tag{D.7}$$

D.3.2 Localizing the Reporter Spins with DEER at Several Magnetic Field Directions

In order to map the locations of the surface reporter spins, we performed DEER experiments with varying orientation of the magnetic field, using the $\cos^2 \theta$ dependence of the dipole interaction. The full Hamiltonian for the system of NV spin-reporter spin coupled via the magnetic dipole interaction is given by:

$$H = \hbar \Delta S_{z'}^2 + \hbar \gamma_e \boldsymbol{B} \cdot \boldsymbol{S} + \hbar \gamma_e \boldsymbol{B} \cdot \boldsymbol{J} + \frac{\hbar^2 \gamma_e^2}{r_s^3} \left[\boldsymbol{S} \cdot \boldsymbol{J} - 3 \frac{(\boldsymbol{S} \cdot \boldsymbol{r}_s)(\boldsymbol{J} \cdot \boldsymbol{r}_s)}{r_s^2} \right], \tag{D.8}$$

where $\Delta = 2\pi \times 2.87$ GHz is the zero-field splitting, and the z'-axis points along the NV center symmetry axis.

The zero-field splitting is the largest energy in the problem, therefore we can make the secular approximation, retaining only the terms that commute with $S_{z'}$. This amounts to fixing the direction of the vector $\boldsymbol{S}$ to be along the NV center symmetry axis. The next-largest energy term is the reporter-spin Zeeman energy $\hbar\gamma_e \boldsymbol{B}\cdot\boldsymbol{J}$. Once again we make the secular approximation, retaining only the terms that commute with $J_{z''}$, where z'' points along the direction of the magnetic field. This amounts to fixing the direction of the vector $\boldsymbol{J}$ to be along the static magnetic field. The magnetic dipole interaction can now be calculated for an abritrary magnetic field angle.

We define the coordinate axes with the z-axis pointing normal to the diamond surface, and the x axis chosen so that the NV symmetry axis is in the x-z plane. Thus the unit vector along the NV axis is $(\sqrt{2},0,1)/\sqrt{3}$. In order to map the location of the surface reporter spins, we perform DEER experiments for magnetic field $\boldsymbol{B}$ rotating in the x-y plane by angle ϕ, relative to the "aligned" direction. Thus the unit vector along the magnetic field is $(\sqrt{2}\cos\phi, \sqrt{2}\sin\phi, 1)/\sqrt{3}$. The vector from the NV to the reporter spin is $\boldsymbol{r} = (x,y,z)$, where z is the depth of the NV center, measured as described above.

We can now evaluate the terms in the dipole interaction Hamiltonian in eqn. (D.8):

$$\boldsymbol{S}\cdot\boldsymbol{J} = \tfrac{2\cos\phi+1}{3} S_{z'}J_{z''}, \tag{D.9}$$

$$\boldsymbol{S}\cdot\boldsymbol{r}_s = \left(x\sqrt{\tfrac{2}{3}} + z\sqrt{\tfrac{1}{3}}\right) S_{z'}, \tag{D.10}$$

$$\boldsymbol{J}\cdot\boldsymbol{r}_s = \left(x\sqrt{\tfrac{2}{3}}\cos\phi + y\sqrt{\tfrac{2}{3}}\sin\phi + z\sqrt{\tfrac{1}{3}}\right) J_{z''}, \tag{D.11}$$

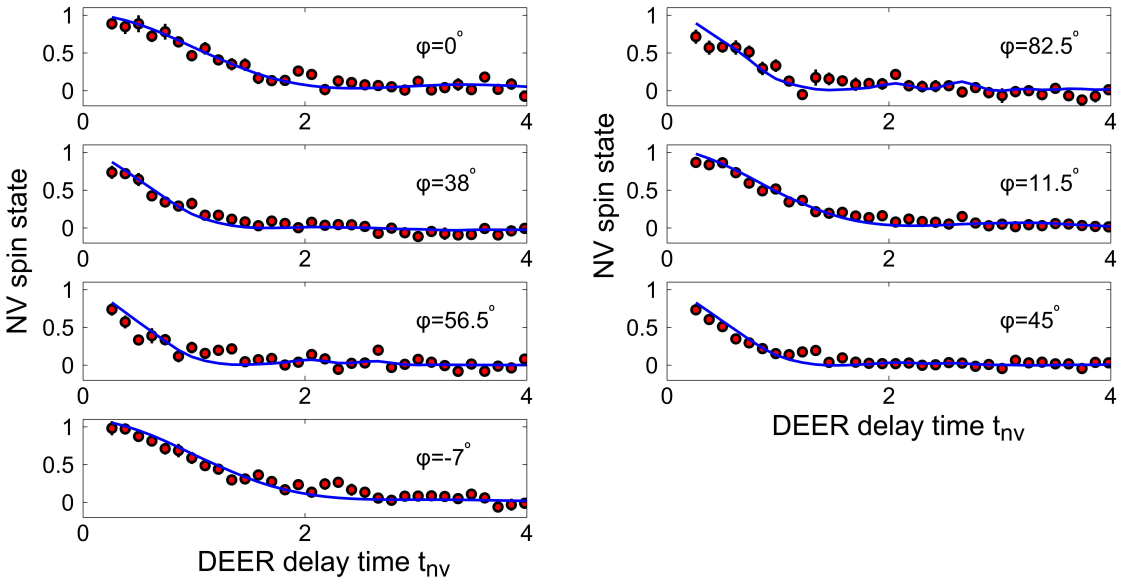

Figure D.2: **DEER data taken at 7 different magnetic field angles, indicated in each plot. The magnetic field magnitude was ≈ 37 G.**

and the dipole interaction Hamiltonian:

$$H_d = \frac{\hbar^2\gamma_e^2}{r_s^3}\left[\frac{2\cos\phi+1}{3} - \frac{\left(x\sqrt{2}+z\right)\left(x\sqrt{2}\cos\phi+y\sqrt{2}\sin\phi+z\right)}{x^2+y^2+z^2}\right] S_{z'}J_{z''} \tag{D.12}$$

Therefore, for a number of reporter spins located at positions (x_s, y_s) on the diamond surface, the NV center spin-state population after a DEER pulse sequence is given by eq. (D.7), with the coupling strengths

$$k_s = \frac{\hbar\gamma_e^2}{r_s^3}\left[\frac{2\cos\phi+1}{3} - \frac{\left(x_s\sqrt{2}+z\right)\left(x_s\sqrt{2}\cos\phi+y_s\sqrt{2}\sin\phi+z\right)}{x_s^2+y_s^2+z^2}\right] \tag{D.13}$$

The DEER experimental data at 7 different magnetic field angles ϕ are shown in Fig. D.2. These data were used to produce the probability density map, shown in Fig. 5.1F of the main text, for the positions of 4 proximal reporter spins on the diamond surface near NV A.

D.3.3 Limits on the Separation Between Surface Reporter Spins from Their Population Relaxation

We can use the reporter-spin population relaxation measurements (Fig. 5.2B) to confirm that the reporter spins are well separated on the diamond surface. The rate of flip-flops between neighbor spins, due to magnetic dipole interaction, is given by [131]

$$w \approx \frac{\hbar\gamma_e^2}{4s^3}\frac{1}{4}, \tag{D.14}$$

where s is the separation between them, and we approximate the angular factor, that depends of the magnetic field direction, by unity. For random reporter spin positions there is likely to be a single closest neighbor that dominates the magnetic dipole interaction. If the depth of the NV center $z \lesssim s$, then the NV center interacts the strongest with a single proximal reporter spin, and the measured population relaxation time $T_1^{(s)}$ corresponds to the time scale for a single spin flip of this proximal reporter:

$$T_1^{(s)} \approx 2\pi/w \approx 32\pi\frac{s^3}{\hbar\gamma_e^2}. \tag{D.15}$$

If the experimentally-measured $T_1^{(s)} \approx 30$ μs is caused by the magnetic dipole interaction between surface reporter spins, then their separation is $s \approx 5$ nm. If another relaxation process limits $T_1^{(s)}$, then $s > 5$ nm.

Another possibility is $z \gg s$, so that the NV center is coupled to many reporter spins. In this case we have to consider spin diffusion, and the population relaxation time $T_1^{(s)}$, as measured by the NV center, would correspond to the time scale for spin diffusion over distance $\approx z$. This can be estimated as follows. The time scale for

a single spin flip-flop is given by eq. (D.15), thus the time scale for diffusion over distance z is:

$$T_1^{(s)} \approx \frac{z^2}{s^2} 32\pi \frac{s^3}{\hbar \gamma_e^2}. \tag{D.16}$$

If the experimentally-measured $T_1^{(s)} \approx 30$ μs were caused by spin diffusion in a bath of closely-spaced reporter spins, then, from eq. (D.16), we extract their spacing to be $s \approx 10$ nm. However, for the ≈ 3.5 nm deep NV centers that we study, this is inconsistent with the assumption $z \gg s$, and we conclude that in our experiments $z \lesssim s$, and $s \gtrsim 5$ nm, as estimated above.

D.4 The Reporter Pulse Sequence

In order to manipulate and probe the reporter spin network we use a "reporter" pulse sequence, inspired by Ramsey interferometry in atomic physics, Fig. D.3. The pulse sequence is separated into two parts: the initial state readout, and the final state readout. During the initial state readout, the phase acquired by the NV center due to the surface sensor spins is ϕ_1, and during the final state readout this phase is ϕ_2. Note that these phases flip sign during the first and second halves of the NV echos, since we apply a π-pulse to the surface sensor spins simultaneously with the π-pulse on the NV. During the period between the initial and the final readout intervals, the NV acquires a phase χ, but, if we keep this time interval longer than NV T_2^*, then $\langle \chi \rangle = \langle \sin \chi \rangle = 0$, and χ does not, on average, affect the NV population. The population readout of the NV center at the end of the pulse sequence is then given

by

$$S = \tfrac{1}{4}\left(2 + \cos(\phi_1 + \phi_2) - \cos(\phi_1 - \phi_2)\right) \tag{D.17}$$

$$= \tfrac{1}{2}\left(1 - \sin\phi_1 \sin\phi_2\right). \tag{D.18}$$

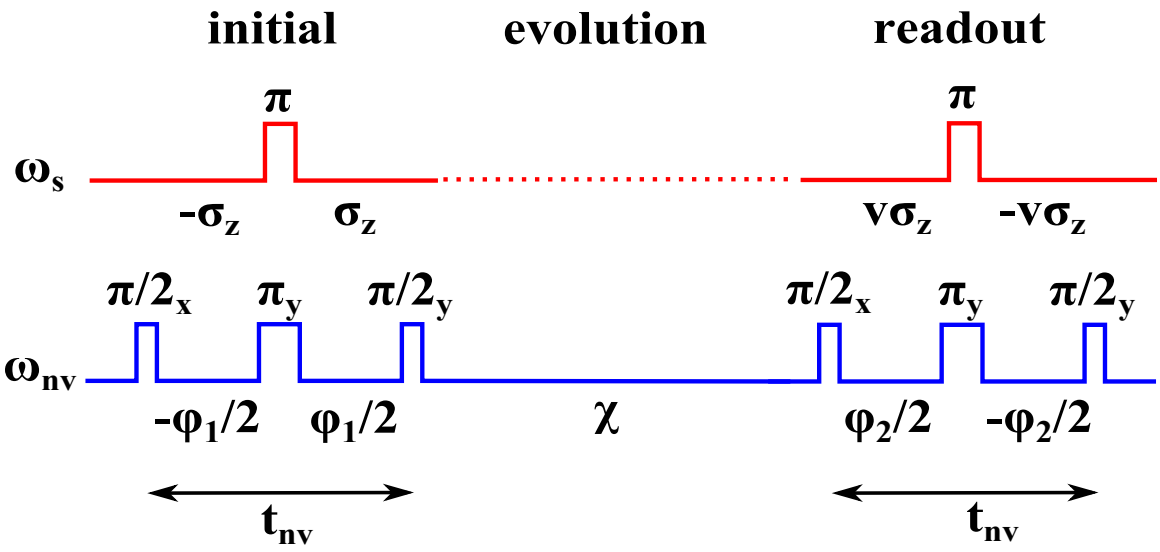

Figure D.3: **Pulse sequence for NV readout of surface sensors.**

Let us assume that the spin projection of a surface sensor spin s at the start of the sequence is σ_s^z, and the coupling to the NV center is k_s, as given in eq. (D.3). Then the NV phase ϕ_1 is given by the sum over all surface sensor spins:

$$\phi_1 = \frac{t_{nv}}{2} \sum_s k_s \sigma_s^z. \tag{D.19}$$

where t_{nv} is the duration of the echo.

During the surface sensor spin evolution, the projection of the surface sensor spin changes: $\sigma_s^z \to v_s^{(i)} \sigma_s^z$, where, for each run i of the experiment $v_s^{(i)} = \pm 1$ (since the spin projection can only take values $\pm 1/2$). After averaging over many experimental

runs, we can average $v_s = \langle v_s^{(i)} \rangle$. For example, if we apply a π-pulse to all surface sensor spins, all $v_s^{(i)} = -1$, and $v_s = -1$. The NV phase ϕ_2 is given by

$$\phi_2 = \frac{t_{nv}}{2} \sum_s v_s^{(i)} k_s \sigma_s^z. \tag{D.20}$$

In this way the NV readout provides information about the surface sensor spin evolution v_s. Note that we have to average the NV population signal over all projections σ_s^z of the surface spin sensors.

We perform this average by using

$$\langle \sigma_s^z \rangle = 0,\ \langle \sigma_s^z \sigma_{s'}^z \rangle = 0 \text{ for } s \neq s',\ \langle (\sigma_s^z)^2 \rangle = 1,\ v_s = \langle v_s^{(i)} \rangle, \tag{D.21}$$

to obtain

$$S = \frac{1}{2} - \frac{1}{4} \prod_s v_s \sin^2 \frac{k_s t_{nv}}{2}. \tag{D.22}$$

D.5 Sensing Nuclear Spins Using the Reporter Echo Sequence

D.5.1 Semiclassical Spin Bath

In order to measure the surface sensor coupling to proton spins, we use the pulse sequence shown in Fig. 5.3A, with the surface reporter spin echo. A surface reporter spin may be strongly coupled some proximal protons, and weakly coupled to many other protons that are present on the diamond surface. We describe these weakly-coupled protons as a semiclassical spin bath, whose magnetic moment precesses at the proton Larmor frequency $\omega_n = \gamma_n B$, where $\gamma_n = g_n \mu_N / \hbar$ is the nuclear gyromagnetic

ratio. The magnetic moments create a fluctuating magnetic field at the location of the surface sensor spin, and the reporter spin echo modulation due to this fluctuating field is described by the factor

$$v_s(t_s) = \exp\left[-8(\gamma_n^2 B_n^2/\omega_n^2)\sin^4(\omega_n t_s/4)\right], \tag{D.23}$$

where B_n is the root-mean-squared amplitude of this magnetic field [93, 28, 27].

The extracted magnitude of B_n is 0.3 G, which is consistent with the magnitude of the fluctuating magnetic field created by a bath of proton spins, randomly-located on the diamond surface, with mean separation of ≈ 5.5 $\mathring{A}$. The separation between surface OH groups for a (001)-(2×1) hydroxylated diamond surface is predicted to be approximately 2.6 $\mathring{A}$ [100], therefore our measurements are consistent with approximately 1/4 of the surface sites filled with protons.

D.5.2 Coherent Hyperfine Coupling to Individual Nuclear Spins

The hyperfine interaction between a reporter electronic spin and a proton spin can be described by the Hamiltonian

$$H = a_0 \boldsymbol{J}\cdot\boldsymbol{I} + \frac{\hbar\gamma_e\gamma_n}{r_n^3}\left[\boldsymbol{J}\cdot\boldsymbol{I} - 3\frac{(\boldsymbol{J}\cdot\boldsymbol{r}_n)(\boldsymbol{I}\cdot\boldsymbol{r}_n)}{r_n^2}\right], \tag{D.24}$$

where $\boldsymbol{J}$ is the spin operator of the reporter qubit, $\boldsymbol{I}$ is the proton spin operator, r_n is the separation between the surface sensor spin and the nuclear spin, and a_0 is the contact hyperfine interaction. In the secular approximation the oscillating terms with J_x and J_y can be neglected, and the Hamiltonian reduces to $H = \hbar a J_z I_z + \hbar b J_z I_x$,

where

$$a = a_0 + \frac{\hbar\gamma_e\gamma_n}{r_n^3}\left(1 - 3\cos^2\theta_n\right), \tag{D.25}$$

$$b = \frac{\hbar\gamma_e\gamma_n}{r_n^3}\left(3\cos\theta_n \sin\theta_n\right), \tag{D.26}$$

where θ_n is the angle between the vector between them and the applied magnetic field B. The spin projection of the reporter spin s, coupled to a nuclear spin n, after the echo sequence is described by the expression [97]:

$$v_{s,n}(t_s) = 1 - 2\left(\frac{b\omega_n}{\omega^+\omega^-}\right)\sin^2(\omega^+ t_s/4)\sin^2(\omega^- t_s/4), \tag{D.27}$$

where

$$\omega^{\pm} = \sqrt{(\pm a/2 - \omega_n)^2 + b^2/4}. \tag{D.28}$$

If the surface sensor is coupled to several proximal nuclear spins, as well as the weakly-coupled nuclear spin bath, then

$$v_s(t_s) = \exp\left[-8(\gamma_n^2 B_n^2/\omega_n^2)\sin^4(\omega_n t_s/4)\right]\prod_n v_{s,n}(t_s). \tag{D.29}$$

D.5.3 Fitting Experimental Data

In addition to the interaction with nuclear spins, the reporter spin decoherence rate Γ_s is a fitting parameter. The final expression used for fitting surface spin sensor echo modulation is:

$$v_s(t_s) = e^{-\Gamma_s t_s}\exp\left[-8(\gamma_n^2 B_n^2/\omega_n^2)\sin^4(\omega_n t_s/4)\right]\prod_n v_{s,n}(t_s), \tag{D.30}$$

where the product is over the strongly-coupled nuclear spins.

Finally, if the NV center is coupled to several surface sensor spins,

$$S = \frac{1}{2} - \frac{1}{4}\prod_s v_s \sin^2 \frac{k_s t_{nv}}{2}, \tag{D.31}$$

as in eq. (D.22).

The fits shown in Fig. 5.4A and 5.4B were performed by first using the DEER data to extract the magnetic dipole coupling constant k_s of the NV center to the proximal reporter spin, and fitting the reporter spin echo data using eqn. (D.30), with one or two coherently-coupled protons, and a proton spin bath, see Table D.1 for relevant best-fit parameters for the fits shown Fig. 5.3A and Fig. 5.4A,B of main text.

In order to calibrate the reporter spin state, we performed two measurements using the reporter sequence: (i) with no pulse in the evolution segment, and (ii) with a π-pulse in the evolution segment. These were taken to correspond to (i) no reporter spin state change $\rightarrow +1$, and (ii) reporter spin flip $\rightarrow -1$. The reporter sequence measurements in this work were done in pairs, with the reporter evolution sequences differing by a reporter π-pulse. For example, the reporter echo measurement was done first with the reporter pulses $\pi/2$-π-$\pi/2$, immediately followed by a sequence $\pi/2$-π-$3\pi/2$. We confirmed that these measurements resulted in opposite final reporter spin populations.

D.6 Control Experiment: Acid-Cleaning the Diamond Surface

Treatment of the diamond crystal surface with the strongly-oxidizing 3-acid mixture (equal volumes of concentrated H_2SO_4, HNO_3, and $HClO_4$) for two hours re-sets

NV center	magnetic field	parameter	best-fit value
NV A	383 G	k_s	1.6 μs^{-1}
		Γ_s	1.3 μs^{-1}
		ω_n	10.6 μs^{-1}
		reduced χ^2	1.2
NV A	619 G	k_s	1.6 μs^{-1}
		Γ_s	1.8 μs^{-1}
		ω_n	19 μs^{-1}
		reduced χ^2	1.3
NV B	665 G	k_s	1.4 μs^{-1}
		Γ_s	1.3 μs^{-1}
		ω_n	17.1 μs^{-1}
		reduced χ^2	1.1

Table D.1: Best-fit parameters.

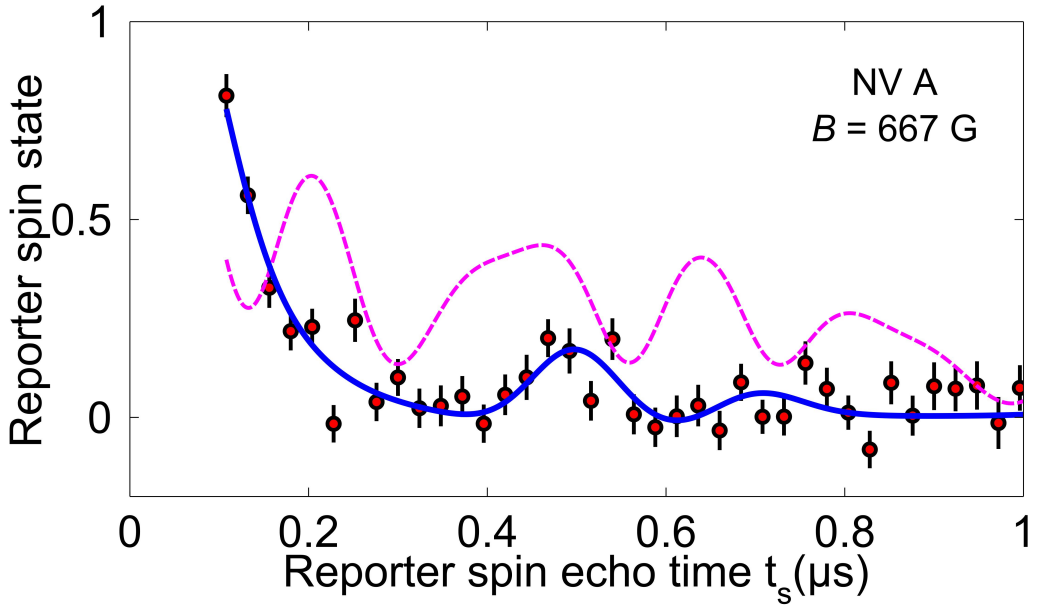

Figure D.4: **The NV A reporter spin echo measurement after 3-acid surface treatment.** The best-fit curve for the measurement before the surface treatment is shown as a dashed magenta line (see also Fig. 5.4A of main text).

the locations of the surface reporter qubits (Fig. 5.1E of main text). We also repeated the reporter spin echo experiment on NV A after this surface treatment, see Fig. D.4. The data are clearly modified, indicating that this measurement is sensitive to the interaction between the reporter spin at a new, post-clean, location, with protons in its vicinity on the diamond surface.

Bibliography

[1] J. Fiaux, E. B. Bertelsen, A. L. Horwich, and K. Wüthrich. NMR analysis of a 900K GroEL GroES complex. *Nature*, 418(6894):207–211, 2002.

[2] K. Pervushin, R. Riek, G. Wider, and K. Wüthrich. Attenuated T2 relaxation by mutual cancellation of dipole-dipole coupling and chemical shift anisotropy indicates an avenue to NMR structures of very large biological macromolecules in solution. *Proceedings of the National Academy of Sciences of the United States of America*, 94(23):12366–71, November 1997.

[3] N. Nishida, F. Motojima, M. Idota, H. Fujikawa, M. Yoshida, I. Shimada, and K. Kato. Probing dynamics and conformational change of the GroEL-GroES complex by 13C NMR spectroscopy. *Journal of biochemistry*, 140(4):591–8, October 2006.

[4] S. Raman, O. F. Lange, P. Rossi, M. Tyka, X. Wang, J. Aramini, G. Liu, T. a. Ramelot, A. Eletsky, T. Szyperski, M. a. Kennedy, J. Prestegard, G. T. Montelione, and D. Baker. NMR structure determination for larger proteins using backbone-only data. *Science (New York, N.Y.)*, 327(5968):1014–1018, February 2010.

[5] M. Kainosho, T. Torizawa, Y. Iwashita, T. Terauchi, A. Mei Ono, and P. Güntert. Optimal isotope labelling for NMR protein structure determinations. *Nature*, 440(7080):52–7, March 2006.

[6] B. Fürtig, C. Richter, J. Wöhnert, and H. Schwalbe. NMR spectroscopy of RNA. *Chembiochem : a European journal of chemical biology*, 4(10):936–962, October 2003.

[7] N. K. Logothetis. What we can do and what we cannot do with fMRI. *Nature*, 453:869–878, 2008.

[8] K.-I. Matsumoto, S. Subramanian, R. Murugesan, J. B. Mitchell, and M. C. Krishna. Spatially Resolved Biologic Information from *In Vivo* EPRI, OMRI and MRI. *Antioxidants & Redox Signaling*, 9(8):1125, 2007.

[9] E. T. Ahrens and J. W. M. Bulte. Tracking immune cells *in vivo* using magnetic resonance imaging. *Nature Reviews Immunology*, 13:755–763, 2013.

[10] N. Netzer, J. M. Goodenbour, A. David, K. A. Dittmar, R. B. Jones, J. R. Schneider, D. Boone, E. M. Eves, M. R. Rosner, J. S. Gibbs, A. Embry, B. Dolan, S. Das, H. D. Hickman, P. Berglund, J. R. Bennink, J. W. Yewdell, and T. Pan. Innate immune and chemically triggered oxidative stress modifies translational fidelity. *Nature*, 462:522–526, 2009.

[11] B. Halliwell. Oxidative stress and cancer: have we moved forward? *Biochemical Journal*, 401(1):1–11, 2007.

[12] M. Valko, D. Leibfritz, J. Moncol, M. T. D. Cronin, M. Mazur, and J. Telser. Free radicals and antioxidants in normal physiological functions and human disease. *The International Journal of Biochemistry & Cell Biology*, 39(1):44–84, 2007.

[13] K. C. Nowack, E. M. Spanton, M. Baenninger, M. Koenig, J. R. Kirtley, B. Kalisky, C. Ames, P. Leubner, C. Bruene, H. Buhmann, L. W. Molenkamp, D. Goldhaber-Gordon, and K. A. Moler. Imaging currents in HgTe quantum wells in the quantum spin Hall regime. *Nature Materials*, 12:787–791, 2013.

[14] S. J. Bending. Local magnetic probes of superconductors. *Advances in Physics*, 48:449–535, 1999.

[15] J. C. Allred, R. N. Lyman, T. W. Kornack, and M. V. Romalis. High-Sensitivity Atomic Magnetometer Unaffected by Spin-Exchange Relaxation. *Physical Review Letters*, 89:130801, 2002.

[16] A. Blank, C. R. Dunnam, P. P. Borbat, and J. H. Freed. Pulsed three-dimensional electron spin resonance microscopy. *Applied Physics Letters*, 85(22):5430, 2004.

[17] P. Glover and S. P. Mansfield. Limits to magnetic resonance microscopy. *Reports on Progress in Physics*, 65(10):1489–1511, October 2002.

[18] L. Ciobanu, D. A. Seeber, and C. H. Pennington. 3D MR microscopy with resolution 3.7 μm by 3.3 μm by 3.3 μm. *Journal of Magnetic Resonance*, 158(1-2):178–182, 2002.

[19] A. Blank and J. H. Freed. ESR Microscopy and Nanoscopy with Induction Detection. *Isr. J. Chem.*, 46:423–438, 2006.

[20] D. Rugar, R. Budakian, , H. J. Mamin, and B. W. Chui. Single spin detection by magnetic resonance force microscopy. *Nature*, 430:329–332, 2004.

[21] C. L. Degen, M. Poggio, H. J. Mamin, C. T. Rettner, and D. Rugar. Nanoscale magnetic resonance imaging. *Proceedings of the National Academy of Sciences*, 106(5):1313–1317, 2009.

[22] J. M. Taylor, P. Cappellaro, L. Childress, L. Jiang, D. Budker, P. R. Hemmer, a. Yacoby, R. Walsworth, and M. D. Lukin. High-sensitivity diamond magnetometer with nanoscale resolution. *Nature Physics*, 4(10):810–816, September 2008.

[23] J. R. Maze, P. L. Stanwix, J. S. Hodges, S. Hong, J. M. Taylor, P. Cappellaro, L. Jiang, M. V. Gurudev-Dutt, E. Togan, A. S. Zibrov, A. Yacoby, R. L. Walsworth, and M. D. Lukin. Nanoscale magnetic sensing with an individual electronic spin in diamond. *Nature*, 455:644–647, 2008.

[24] S. Steinert, F. Ziem, L. T. Hall, A. Zappe, M. Schweikert, N. Gotz, A. Aird, G. Balasubramanian, L. Hollenberg, and J. Wrachtrup. Magnetic spin imaging under ambient conditions with sub-cellular resolution. *Nature Communications*, 4:1607, 2013.

[25] J.-P. Tetienne, T. Hingant, L. Rondin, A. Cavailles, L. Mayer, G. Dantelle, T. Gacoin, J. Wrachtrup, J.-F. Roch, and V. Jacques. Spin relaxometry of single nitrogen-vacancy defects in diamond nanocrystals for magnetic noise sensing. *Physical Review B*, 87:235436, 2013.

[26] S. Kaufmann, D. A. Simpson, L. T. Hall, V. Perunicic, P. Senn, S. Steinert, L. P. McGuinness, B. C. Johnson, T. Ohshima, F. Caruso, J. Wrachtrup, R. E. Scholten, P. Mulvaney, and L. Hollenberg. Detection of atomic spin labels in a lipid bilayer using a single-spin nanodiamond probe. *Proceedings of the National Academy of Sciences*, 110:10894, 2013.

[27] T. Staudacher, F. Shi, S. Pezzagna, J. Meijer, J. Du, C. a. Meriles, F. Reinhard, and J. Wrachtrup. Nuclear magnetic resonance spectroscopy on a (5-nanometer)^3 sample volume. *Science*, 339(6119):561–563, February 2013.

[28] H. J. Mamin, M. Kim, M. H. Sherwood, C. T. Rettner, K. Ohno, D. D. Awschalom, and D. Rugar. Nanoscale nuclear magnetic resonance with a nitrogen-vacancy spin sensor. *Science*, 339(6119):557–560, February 2013.

[29] M. W. Doherty, N. B. Manson, P. Delaney, F. Jelezko, J. Wrachtrup, and L. C. Hollenberg. The nitrogen-vacancy colour centre in diamond. *Physics Reports*, 528(1):1–45, July 2013.

[30] L. I. Childress. *Coherent manipulation of single quantum systems in the solid state*. PhD thesis, Harvard University, Cambridge, Massachusetts, March 2007.

[31] M. L. Goldman, M. W. Doherty, A. Sipahigil, N. Y. Yao, S. D. Bennett, N. B. Manson, A. Kubanek, and M. D. Lukin. State-selective intersystem crossing in nitrogen-vacancy centers. *Physical Review B*, 91:165201, 2015.

[32] P. Maurer, G. Kucsko, C. Latta, L. Jiang, N. Y. Yao, S. D. Bennett, F. Pastawski, D. Hunger, N. Chisholm, M. Markham, D. J. Twitchen, J. I. Cirac, and M. D. Lukin. Room-temperature quantum bit memory exceeding one second. *Science*, 336(6086):1283–1286, 2012.

[33] Y. Romach, C. Müller, T. Unden, L. J. Rogers, T. Isoda, K. M. Itoh, M. Markham, A. Stacey, J. Meijer, S. Pezzagna, B. Naydenov, L. P. McGuinness, N. Bar-Gill, and F. Jelezko. Spectroscopy of surface-induced noise using shallow spins in diamond. *Physical Review Letters*, 114:017601, 2015.

[34] Z.-H. Wang, G. de Lange, D. Ristè, R. Hanson, and V. V. Dobrovitski. Comparison of dynamical decoupling protocols for a nitrogen-vacancy center in diamond. *Physical Review B*, 85:155204, 2012.

[35] L. M. Pham, S. J. DeVience, F. Casola, I. Lovchinsky, A. O. Sushkov, E. Bersin, J. Lee, E. Urbach, P. Cappellaro, H. Park, A. Yacoby, M. Luking, and R. L. Walsworth. NMR technique for determining the depth of shallow nitrogen-vacancy centers in diamond. *Physical Review B*, 93:045425, 2016.

[36] A. Jarmola, V. M. Acosta, K. Jensen, S. Chemerisov, and D. Budker. Temperature- and Magnetic-Field-Dependent Longitudinal Spin Relaxation in Nitrogen-Vacancy Ensembles in Diamond. *Physical Review Letters*, 108:197601, 2012.

[37] G. Balasubramanian, I. Y. Chan, R. Kolesov, M. Al-Hmoud, J. Tisler, C. Shin, C. Kim, A. Wojcik, P. R. Hemmer, A. Krueger, T. Hanke, A. Leitenstorfer, R. Bratschitsch, F. Jelezko, and J. Wrachtrup. Nanoscale imaging magnetometry with diamond spins under ambient conditions. *Nature*, 455(7213):648–651, October 2008.

[38] S. Kolkowitz, Q. P. Unterreithmeier, S. D. Bennett, and M. D. Lukin. Sensing distant nuclear spins with a single electron spin. *Physical Review Letters*, 109:137601, 2012.

[39] P. London, J. Scheuer, J.-M. Cai, A. Schwarz, A. Retzker, M. B. Plenio, M. Katagiri, T. Teraji, S. Koizumi, J. Isoya, R. Fischer, L. P. McGuinness, B. Naydenov, and F. Jelezko. Detecting and polarizing nuclear spins with double resonance on a single electron spin. *Physical Review Letters*, 111:067601, 2013.

[40] S. Vijay-Kumar, C. E. Bugg, and W. J. Cook. Structure of ubiquitin refined at 1.8 $\AA$ resolution. *J Mol Biol*, 194(3):531–544, Apr 1987.

[41] L. Jiang, J. S. Hodges, J. Maze, P. Maurer, J. M. Taylor, D. G. Cory, P. R. Hemmer, R. L. Walsworth, A. Yacoby, A. S. Zibrov, and M. D. Lukin. Repetitive readout of a single electronic spin via quantum logic with nuclear spin ancillae. *Science*, 326:267–272, 2009.

[42] P. Neumann, J. Beck, M. Steiner, F. Rempp, H. Fedder, P. R. Hemmer, W. J, and F. Jelezko. Single-shot readout of a single nuclear spin. *Science*, 329:542–544, 2010.

[43] Y. Chu, N. P. de Leon, B. J. Shields, B. Hausmann, R. Evans, E. Togan, M. J. Burek, M. Markham, A. Stacey, A. S. Zibrov, A. Yacoby, D. J. Twitchen, M. Loncar, H. Park, P. Maletinsky, and M. D. Lukin. Coherent optical transitions in implanted nitrogen vacancy centers. *NanoLetters*, 14(4):1982–1986, 2014.

[44] M. Kim, H. J. Mamin, M. H. Sherwood, C. T. Rettner, J. Frommer, and D. Rugar. Effect of oxygen plasma and thermal oxidation on shallow nitrogen-vacancy centers in diamond. *Applied Physics Letters*, 105(4):042406, 2014.

[45] G. Goldstein, M. Scheid, U. Hammerling, D. H. Schlesinger, H. D. Niall, and E. A. Boyse. Isolation of a polypeptide that has lymphocyte-differentiating properties and is probably represented universally in living cells. *Proceedings of the National Academy of Sciences*, 72(1):11–15, 1975.

[46] J. C. Sheehan, P. A. Cruickshank, and G. L. Boshart. A convenient synthesis of water-soluble carbodiimides. *The Journal of Organic Chemistry*, 26(7):2525–2528, 1960.

[47] A. O. Sushkov, N. Chisholm, I. Lovchinsky, K. M, P. K. Lo, S. D. Bennett, D. Hunger, A. Akimov, R. L. Walsworth, H. Park, and M. D. Lukin. All-optical sensing of a single-molecule electron spin. *NanoLetters*, 14(11):6443–6448, 2014.

[48] M. Loretz, S. Pezzagna, J. Meijer, and C. L. Degen. Nanoscale nuclear magnetic resonance with a 1.9-nm-deep nitrogen-vacancy sensor. *Applied Physics Letters*, 104(3):033102, January 2014.

[49] D. B. Zax, A. Bielecki, K. W. Zilm, A. Pines, and D. P. Weitekamp. Zero field NMR and NQR. *Journal of Chemical Physics*, 83(10):4877–4905, 1985.

[50] T. P. Das and E. L. Hahn. *Nuclear Quadrupole Resonance Spectroscopy*. Academic Press Publishers, New York, USA, 1958.

[51] B. J. Shields, Q. P. Unterreithmeier, de Leon N P, H. Park, and M. D. Lukin. Efficient readout of a single spin state in diamond via spin-to-charge conversion. *Physical Review Letters*, 114:136402, 2015.

[52] A. O. Sushkov, I. Lovchinsky, N. Chisholm, R. L. Walsworth, H. Park, and M. D. Lukin. Magnetic resonance detection of individual proton spins using quantum reporters. *Physical Review Letters*, 113:197601, 2014.

[53] T. Staudacher, N. Raatz, S. Pezzagna, J. Meijer, F. Reinhard, C. A. Meriles, and J. Wrachtrup. Probing molecular dynamics at the nanoscale via an individual paramagnetic centre. *Nature Communications*, 6:8527, 2015.

[54] S. Cavadini. Indirect detection of nitrogen-14 in solid-state NMR spectroscopy. *Progress in Nuclear Magnetic Resonance Spectroscopy*, 56:46–77, 2010.

[55] A. Ajoy, U. Bissbort, M. D. Lukin, R. L. Walsworth, and P. Cappellaro. Atomic-scale nuclear spin imaging using quantum-assisted sensors in diamond. *Physical Review X*, 5:011001, 2015.

[56] L. Childress, R. L. Walsworth, and M. D. Lukin. Atom-like crystal defects: From quantum computers to biological sensors. *Physics Today*, 67(10):38–43, 2014.

[57] T. Klar, R. Wollhofen, and J. Jacak. Sub-Abbe resolution: from STED microscopy to STED lithography. *Physica Scripta*, T162:014049, 2014.

[58] H. S. Chung, K. McHale, J. M. Louis, and W. A. Eaton. Single-molecule fluorescence experiments determine protein folding transition path times. *Science*, 335:981–984, 2012.

[59] I. A. Yudushkin, A. Schleifenbaum, A. Kinkhabwala, B. G. Neel, C. Schultz, and P. I. H. Bastiaens. Live-cell imaging of enzyme-substrate interaction reveals spatial regulation of ptp1b. *Science*, 315(5808):115–119, 2007.

[60] K. S. Novoselov, A. Mishchenko, A. Carvalho, and A. H. Castro Neto. 2D materials and van der Waals heterostructures. *Science*, 353:461, 2016.

[61] A. K. Geim and I. V. Grigorieva. Van der Waals heterostructures. *Nature*, 499:419–425, 2013.

[62] T. T. Tran, K. Bray, M. J. Ford, M. Toth, and I. Aharonovich. Quantum emission from hexagonal boron nitride monolayers. *Nature Nanotechnology*, 11:37–41, 2016.

[63] B. H. Suits. *Handbook of Applied Solid State Spectroscopy*. Springer, New York, USA, 2006.

[64] U. Werner, B. B, M. Ziegeweid, and A. Pines. SQUID-NQR of nitrogen-14 in amino acids and small peptides. *Chemical Physics Letters*, 209:17–21, 1993.

[65] S. Brummer and A. Weiss. Crystal Structure and Nuclear Quadrupole Resonance. The Bond Length C – Cl and ^{35}Cl NQR. *Berichte der Bunsengesellschaft für physikalische Chemie*, 94:497–513, 1990.

[66] I. Lovchinsky, A. O. Sushkov, E. Urbach, N. P. de Leon, S. Choi, K. De Greve, R. Evans, R. Gertner, E. Bersin, C. Muller, L. McGuinness, F. Jelezko, R. L. Walsworth, H. Park, and M. D. Lukin. Nuclear Magnetic Resonance Detection and Spectroscopy of Single Proteins Using Quantum Logic. *Science*, 351:836–841, 2016.

[67] T. Wolf, P. Neumann, K. Nakamura, H. Sumiya, T. Ohshima, J. Isoya, and J. Wrachtrup. Subpicotesla Diamond Magnetometry. *Physical Review X*, 5:041001, 2015.

[68] A. H. Silver and P. J. Bray. NMR Study of Bonding in Some Solid Boron Compounds. *Journal of Chemical Physics*, 32:288–292, 1960.

[69] S. J. DeVience, L. M. Pham, I. Lovchinsky, A. O. Sushkov, N. Bar-Gill, C. Belthangady, F. Casola, M. Corbett, H. Zhang, M. D. Lukin, H. Park, A. Yacoby, and R. L. Walsworth. Nanoscale NMR spectroscopy and imaging of multiple nuclear species. *Nature Nanotechnology*, 10:129–134, 2015.

[70] P. Maletinsky, S. Hong, M. S. Grinolds, B. Hausmann, M. D. Lukin, R. L. Walsworth, M. Loncar, and A. Yacoby. A robust scanning diamond sensor for nanoscale imaging with single nitrogen-vacancy centres. *Nature Nanotechnology*, 7:320–324, 2012.

[71] M. Chhowalla, Z. Liu, and H. Zhang. Two-dimensional transition metal dichalcogenite (TMD) nanosheets. *Chemical Society Reviews*, 44:2584–2586, 2015.

[72] M. P. Boneschanscher, W. H. Evers, J. J. Geuchies, T. Altantzis, B. Goris, F. T. Rabouw, S. A. P. van Rossum, H. S. J. van der Zant, L. D. A. Siebbeles, G. Van Tendeloo, I. Swart, J. Hilhorst, A. V. Petukhov, S. Bals, and D. Vanmaekelbergh. Long-range orientation and atomic attachment of nanocrystals in 2D honeycomb superlattices. *Science*, 344:1377–1380, 2014.

[73] C. D. Aiello and P. Cappellaro. Time-optimal control by a quantum actuator. *Physical Review A*, 91:042340, 2015.

[74] J. Cai, A. Retzker, F. Jelezko, and M. B. Plenio. A large-scale quantum simulator on a diamond surface at room temperature. *Nature Physics*, 9:168–173, 2013.

[75] J. W. Britton, B. C. Sawyer, A. C. Keith, C. C. Joseph Wang, J. K. Freericks, H. Uys, M. J. Biercuk, and J. J. Bollinger. Engineered two-dimensional Ising interactions in a trapped-ion quantum simulator with hundreds of spins. *Nature*, 484:489–492, 2012.

[76] R. Bierig, M. Weber, and S. Warshaw. Paramagnetic Resonance and Relaxation of Trivalent Rare-Earth Ions in Calcium Fluoride. II. Spin-Lattice Relaxation. *Physical Review*, 134(6A):A1504–A1516, June 1964.

[77] H. K. Kim, G. H. Lee, T. J. Kim, and Y. Chang. Determination of Correlation Times of New Paramagnetic Gadolinium MR Contrast Agents by EPR and 17O NMR. *Bull. Kor. Chem. Soc.*, 30:849, 2009.

[78] L. Hall, C. Hill, J. Cole, and L. Hollenberg. Ultrasensitive diamond magnetometry using optimal dynamic decoupling. *Physical Review B*, 82(4), July 2010.

[79] V. S. Perunicic, L. T. Hall, D. A. Simpson, C. D. Hill, and L. C. L. Hollenberg. Single molecule NMR detection and spectroscopy using single spins in diamond. *ArXiv: 1307.8220*, July 2013.

[80] B. N. G. Giepmans, S. R. Adams, M. H. Ellisman, and R. Y. Tsien. The fluorescent toolbox for assessing protein location and function. *Science*, 312(5771):217–224, April 2006.

[81] D. Le Sage, K. Arai, D. R. Glenn, S. J. DeVience, L. M. Pham, L. Rahn-Lee, M. D. Lukin, A. Yacoby, A. Komeili, and R. L. Walsworth. Optical magnetic imaging of living cells. *Nature*, 496(7446):486–489, April 2013.

[82] S. J. James, P. Cutler, S. Melnyk, S. Jernigan, L. Janak, D. W. Gaylor, and J. A. Neubrander. Metabolic biomarkers of increased oxidative stress and impaired methylation capacity in children with autism. *Am J Clin Nutr*, 80(6):1611–1617, December 2004.

[83] M. S. Grinolds, S. Hong, P. Maletinsky, L. Luan, M. D. Lukin, R. L. Walsworth, and A. Yacoby. Nanoscale magnetic imaging of a single electron spin under ambient conditions. *Nature Physics*, 9(4):215–219, February 2013.

[84] J. R. Kirtley. Fundamental studies of superconductors using scanning magnetic imaging. *Reports on Progress in Physics*, 73(12):126501, December 2010.

[85] H. Zhang, C.-X. Liu, X.-L. Qi, X. Dai, Z. Fang, and S.-C. Zhang. Topological insulators in Bi2Se3, Bi2Te3 and Sb2Te3 with a single Dirac cone on the surface. *Nature Physics*, 5(6):438–442, May 2009.

[86] M. Schaffry, E. M. Gauger, J. J. L. Morton, and S. C. Benjamin. Proposed Spin Amplification for Magnetic Sensors Employing Crystal Defects. *Physical Review Letters*, 107(20):207210, November 2011.

[87] B. Grotz, J. Beck, P. Neumann, B. Naydenov, R. Reuter, F. Reinhard, F. Jelezko, J. Wrachtrup, D. Schweinfurth, B. Sarkar, and P. Hemmer. Sensing external spins with nitrogen-vacancy diamond. *New Journal of Physics*, 13(5):055004, May 2011.

[88] M. S. Grinolds, M. Warner, K. De Greve, Y. Dovzhenko, L. Thiel, R. L. Walsworth, S. Hong, P. Maletinsky, and A. Yacoby. Subnanometre resolution in three-dimensional magnetic-resonance imaging of individual dark spins. *Nature Nanotechnology*, 9:279–284, 2014.

[89] B. A. Myers, A. Das, M. C. Dartiailh, K. Ohno, D. D. Awschalom, and A. C. Bleszynski Jayich. Probing surface noise with depth-calibrated spins in diamond. *Physical Review Letters*, 113:027602, 2014.

[90] T. Rosskopf, A. Dussaux, K. Ohashi, M. Loretz, R. Schirhagl, H. Watanabe, S. Shikata, K. M. Itoh, and C. L. Degen. Investigation of Surface Magnetic Noise by Shallow Spins in Diamond. *Physical Review Letters*, 112(14):147602, April 2014.

[91] H. R. Herschman. Molecular imaging: looking at problems, seeing solutions. *Science*, 302(5645):605–8, October 2003.

[92] M. Scanziani and M. Häusser. Electrophysiology in the age of light. *Nature*, 461(7266):930–9, October 2009.

[93] L. Childress, M. V. Gurudev Dutt, J. M. Taylor, A. S. Zibrov, F. Jelezko, J. Wrachtrup, P. R. Hemmer, and M. D. Lukin. Coherent dynamics of coupled electron and nuclear spin qubits in diamond. *Science*, 314(5797):281–5, October 2006.

[94] P. Neumann, R. Kolesov, B. Naydenov, J. Beck, F. Rempp, M. Steiner, V. Jacques, G. Balasubramanian, M. L. Markham, D. J. Twitchen, S. Pezzagna, J. Meijer, J. Twamley, F. Jelezko, and J. Wrachtrup. Quantum register based on coupled electron spins in a room-temperature solid. *Nature Physics*, 6(4):249–253, February 2010.

[95] N. Ramsey. A Molecular Beam Resonance Method with Separated Oscillating Fields. *Physical Review*, 78(6):695–699, June 1950.

[96] A. Laraoui, F. Dolde, C. Burk, F. Reinhard, J. Wrachtrup, and C. A. Meriles. High-resolution correlation spectroscopy of C spins near a nitrogen-vacancy centre in diamond. *Nature communications*, 4:1651, January 2013.

[97] L. Rowan, E. Hahn, and W. Mims. Electron-Spin-Echo Envelope Modulation. *Physical Review*, 137(1A):A61–A71, January 1965.

[98] M. J. Rao and R. S. Anderson. Electron Spin Resonance in Gamma-Irradiated Single Crystals of Hydroxylated Organic Compounds. *The Journal of Chemical Physics*, 42(8):2899, July 1965.

[99] V. N. Mochalin, O. Shenderova, D. Ho, and Y. Gogotsi. The properties and applications of nanodiamonds. *Nature nanotechnology*, 7(1):11–23, January 2012.

[100] S. Sque, R. Jones, and P. Briddon. Structure, electronics, and interaction of hydrogen and oxygen on diamond surfaces. *Physical Review B*, 73(8):085313, February 2006.

[101] A. O. Sushkov, N. Chisholm, I. Lovchinsky, M. Kubo, P. K. Lo, S. D. Bennett, D. Hunger, A. Akimov, R. L. Walsworth, H. Park, and M. D. Lukin. All-optical sensing of a single-molecule electron spin. *ArXiv: 1311.1801*, November 2013.

[102] H.-J. Wang, C. S. Shin, S. J. Seltzer, C. E. Avalos, A. Pines, and V. S. Bajaj. Optically detected cross-relaxation spectroscopy of electron spins in diamond. *Nature communications*, 5:4135, January 2014.

[103] C. Müller, X. Kong, J.-M. Cai, K. Melentijević, A. Stacey, M. Markham, D. Twitchen, J. Isoya, S. Pezzagna, J. Meijer, J. F. Du, M. B. Plenio, B. Naydenov, L. P. McGuinness, and F. Jelezko. Nuclear magnetic resonance spectroscopy with single spin sensitivity. *Nat Commun*, 5:4703, 2014.

[104] C. Belthangady, N. Bar-Gill, L. Pham, K. Arai, D. Le Sage, P. Cappellaro, and R. Walsworth. Dressed-State Resonant Coupling between Bright and Dark Spins in Diamond. *Physical Review Letters*, 110(15):157601, April 2013.

[105] G. Goldstein, P. Cappellaro, J. R. Maze, J. S. Hodges, L. Jiang, A. S. Sø rensen, and M. D. Lukin. Environment-Assisted Precision Measurement. *Physical Review Letters*, 106(14):140502, April 2011.

[106] L. Cywinski, R. M. Lutchyn, C. P. Nave, and S. D. Sarma. How to enhance dephasing time in superconducting qubits. *Physical Review B*, 77:174509, 2008.

[107] M. Loretz, J. M. Boss, T. Rosskopf, H. J. Mamin, D. Rugar, and C. L. Degen. Spurious harmonic response of multipulse quantum sensing sequences. *Physical Review X*, 5:021009, 2015.

[108] T. Giavani, H. Bildsoe, J. Skibsted, and H. J. Jakobsen. A solid-state ^{14}N magic-angle spinning NMR study of some amino acids. *Journal of Magnetic Resonance*, 166:262–272, 2004.

[109] P. A. Mirau. *Solid State NMR of Polymers*. iSmithers Rapra Publishing, 2001.

[110] M. J. Hunt and A. L. Mackay. Deuterium and nitrogen pure quadrupole resonance in deuterated amino acids. *Journal of Magnetic Resonance*, 15:402–414, 1974.

[111] D. T. Edmonds and C. P. Summers. ^{14}N Pure Quadrupole Resonance in Solid Amino Acids. *Journal of Magnetic Resonance*, 12:134–142, 1973.

[112] T. J. Bastow, D. Massiot, and J. P. Coutures. ^{14}N NMR in AlN and BN. *Solid State Nuclear Magnetic Resonance*, 10:241–245, 1998.

[113] K. Watanabe, T. Taniguchi, and H. Kanda. Direct-bandgap properties and evidence for ultraviolet lasing of hexagonal boron nitride single crystal. *Nature Materials*, 3:404–409, 2004.

[114] T. Taniguchi and K. Watanabe. Synthesis of high-purity boron nitride single crystals under high pressure by using Ba-BN solvent. *Journal of Crystal Growth*, 303:525–529, 2007.

[115] R. V. Gorbachev, I. Riaz, R. R. Nair, R. Jalil, L. Britnell, B. D. Belle, E. W. Hill, K. S. Novoselov, K. Watanabe, T. Taniguchi, A. K. Geim, and P. Blake. Hunting for Monolayer Boron Nitride: Optical and Raman Signatures. *Small*, 7:465–468, 2011.

[116] P. J. Zomer, M. H. D. Guimaraes, J. C. Brant, N. Tombros, and B. J. van Wees. Fast pick uptechnique for high quality heterostructures of bilayer graphene and hexagonal boron nitride. *Applied Physics Letters*, 105:013101, 2014.

[117] G. de Lange, D. Ristè, V. V. Dobrovitski, and R. Hanson. Single-Spin Magnetometry with Multiple Sensing Sequences. *Physical Review Letters*, 106:080802, 2011.

[118] P. Dufek, P. Blaha, and K. Schwarz. Determination of the Nuclear Quadrupole Moment of ^{57}Fe. *Physical Review Letters*, 75:3545, 1995.

[119] P. Blaha, K. Schwarz, and P. H. Dederichs. First-principles calculation of the electric-field gradient in hcp metals. *Physical Review B*, 37:2792, 1988.

[120] The Elk FP-LAPW Code, http://elk.sourceforge.net/.

[121] J. P. Perdew and Y. Wang. Accurate and simple analytic representation of the electron-gas correlation energt. *Physical Review B*, 45:13244, 1992.

[122] Y. Li, Y. Rao, K. Fai Mak, Y. You, S. Wang, C. R. Dean, and T. F. Heinz. Probing Symmetry Properties of Few-Layer MoS_2 and h-BN by Optical Second-Harmonic Generation. *NanoLetters*, 13:3329–3333, 2013.

[123] S. J. Haigh, A. Gholinia, R. Jalil, S. Romani, L. Britnell, D. C. Elias, K. S. Novoselov, L. A. Ponomarenko, A. K. Geim, and R. V. Gorbachev. Cross-sectional imaging of individual layers and buried interfaces of graphene-based heterostructures and superlattices. *Nature Materials*, 11:764–767, 2012.

[124] J. Henig, I. Mamedov, P. Fouskova, E. Tóth, N. K. Logothetis, G. Angelovski, and H. A. Mayer. Influence of calcium-induced aggregation on the sensitivity of aminobis(methylenephosphonate)-containing potential MRI contrast agents. *Inorganic chemistry*, 50(14):6472–81, July 2011.

[125] P. E. Pehrsson and T. W. Mercer. Oxidation of heated diamond C(100):H surfaces. *Surface Science*, 460(1-3):74–90, July 2000.

[126] P. Strobel, J. Ristein, and L. Ley. Controlled hydroxylation of diamond for covalent attachment of fullerene molecules. *Diamond and Related Materials*, 17(7-10):1362–1366, July 2008.

[127] R. I. Masel. *Principles of adsorption and reaction on solid surfaces*. Wiley, New York, 1996.

[128] A. A. Clerk, M. H. Devoret, S. M. Girvin, F. Marquardt, and R. J. Schoelkopf. Introduction to quantum noise, measurement, and amplification. *Reviews of Modern Physics*, 82(2):1155–1208, April 2010.

[129] E. D. Feigelson and G. J. Babu. *Modern Statistical Methods for Astronomy: With R Applications*, volume 2. Cambridge University Press, 2012.

[130] J. Peacock. Two-dimensional goodness-of-fit testing in astronomy. *Monthly Notices of the Royal Astronomical Society*, 202:615–627, 1983.

[131] A. Abragam. *The principles of nuclear magnetism*. Oxford University Press, 1961.